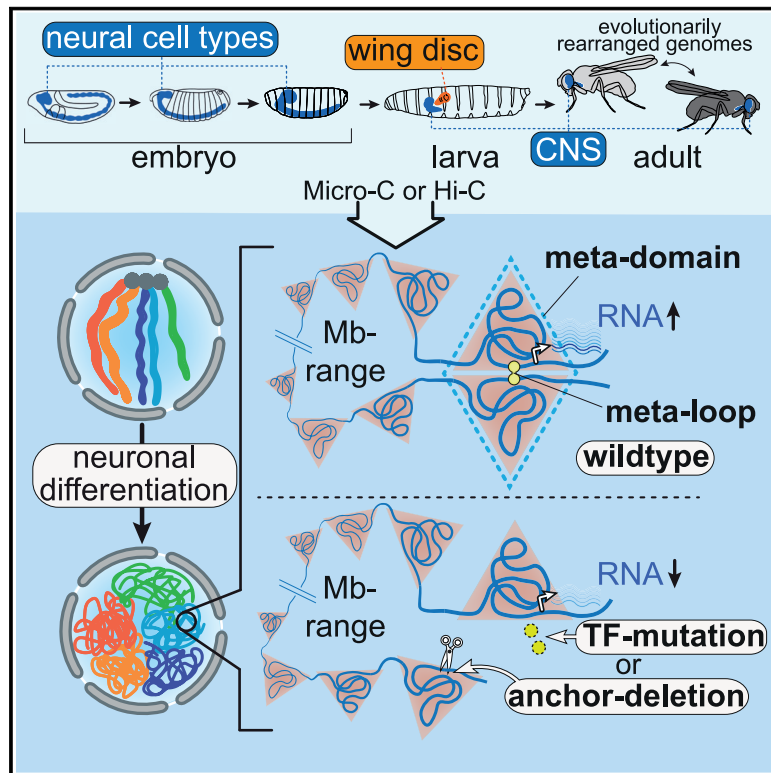


Chromosome-level organization of the regulatory genome in the *Drosophila* nervous system

Graphical abstract



Authors

Giriram Mohana, Julien Dorier, Xiao Li, ..., Aleksander Jankowski, Michael S. Levine, Maria Cristina Gambetta

Correspondence

aleksander.jankowski@uw.edu.pl (A.J.), msl2@princeton.edu (M.S.L.), mariacristina.gambetta@unil.ch (M.C.G.)

In brief

Topologically associating domains that are megabases apart form meta-domains in mature fly neurons to regulate neuronal gene transcription.

Highlights

- Meta-domains are specific associations of distant TADs in mature fly neurons
- In meta-domains, meta-loops tether neuronal gene promoters and intergenic elements
- Meta-loops enable megabase-range regulation of neuronal gene transcription
- Dedicated transcription factors, such as CTCF and GAF, form individual meta-loops



Article

Chromosome-level organization of the regulatory genome in the *Drosophila* nervous system

Giriram Mohana,^{1,8} Julien Dorier,^{2,3,8} Xiao Li,^{4,8} Marion Mougnot,¹ Rebecca C. Smith,⁵ H el ena Malek,¹ Marion Leleu,^{2,3} Daniel Rodriguez,¹ Jenisha Khadka,¹ Patrycja Rosa,⁶ Pascal Cousin,¹ Christian Iseli,^{2,3} Simon Restrepo,⁷ Nicolas Guex,^{2,3} Brian D. McCabe,⁵ Aleksander Jankowski,^{5,*} Michael S. Levine,^{4,*} and Maria Cristina Gambetta^{1,9,*}

¹Center for Integrative Genomics, University of Lausanne, 1015 Lausanne, Switzerland

²Bioinformatics Competence Center, University of Lausanne, 1015 Lausanne, Switzerland

³Bioinformatics Competence Center, Swiss Federal Institute of Technology Lausanne, 1015 Lausanne, Switzerland

⁴Lewis-Sigler Institute for Integrative Genomics, Princeton University, Princeton, NJ, USA

⁵Brain Mind Institute, Swiss Federal Institute of Technology Lausanne, 1015 Lausanne, Switzerland

⁶Faculty of Mathematics, Informatics and Mechanics, University of Warsaw, 02-097 Warsaw, Poland

⁷Arcoris bio AG, L ussirainstrasse 52, 6300 Zug, Switzerland

⁸These authors contributed equally

⁹Lead contact

*Correspondence: aleksander.jankowski@uw.edu.pl (A.J.), msl2@princeton.edu (M.S.L.), mariacristina.gambetta@unil.ch (M.C.G.)
<https://doi.org/10.1016/j.cell.2023.07.008>

SUMMARY

Previous studies have identified topologically associating domains (TADs) as basic units of genome organization. We present evidence of a previously unreported level of genome folding, where distant TAD pairs, megabases apart, interact to form meta-domains. Within meta-domains, gene promoters and structural intergenic elements present in distant TADs are specifically paired. The associated genes encode neuronal determinants, including those engaged in axonal guidance and adhesion. These long-range associations occur in a large fraction of neurons but support transcription in only a subset of neurons. Meta-domains are formed by diverse transcription factors that are able to pair over long and flexible distances. We present evidence that two such factors, GAF and CTCF, play direct roles in this process. The relative simplicity of higher-order meta-domain interactions in *Drosophila*, compared with those previously described in mammals, allowed the demonstration that genomes can fold into highly specialized cell-type-specific scaffolds that enable megabase-scale regulatory associations.

INTRODUCTION

Previous studies identified diverse genome-folding mechanisms at different scales. Local folding into topologically associating domains (TADs) occurs when cohesin extrudes chromosomal loops until it is stalled by DNA-bound CCCTC-binding factor (CTCF) at domain boundaries^{1,2} or when active and inactive contiguous chromatin regions physically segregate.³ TADs can further associate into higher-order assemblies.^{4–6} Beyond TADs, chromosomes organize into territories and more broadly into transcriptionally active and inactive compartments.^{7–9} Transcription factors shape three-dimensional (3D) genome contacts within these frameworks.^{10–13} A basic question arises regarding the role of 3D genome folding in facilitating specialized gene expression, as regulatory interactions are, to a certain degree, distance dependent.^{14–16}

Functional interactions between regulatory elements and gene promoters primarily occur within TADs, spanning distances of 10–100 kb in flies and megabases (Mb) in mice.^{17,18} TADs guide and constrain regulatory interactions, although the impact on

TAD-internal gene regulation varies between loci.^{15,19–24} Although TADs may be sufficient or even dispensable for most local regulation, long-range regulation may require additional 3D structural support. In flies, tethering elements bridge distal regulatory elements and target genes within the same TAD, facilitating rapid activation of certain developmental genes²⁵ and co-regulation of distant paralogs.²⁶ In mammals, loop extrusion brings promoters and regulatory elements into contact over long distances.^{15,27,28} Additionally, mammalian “tethering-like elements” bridge some enhancers to their target promoters within TADs for activation.²³ These TAD-level features are often constitutive features of genomes.

Recent studies explored how 3D genome organization contributes to cell-type-specific transcription programs in mammalian tissues, purified cells, and cell culture models. Local variations in 3D genome folding were observed within TADs, at their boundaries, and in long-range contacts and compartments.^{10,29–31} In some striking cases, distant genes and regulatory elements co-bound by common transcription factors coalesce into specialized hubs.^{10,11,32,33} However, the redundancy of such



assemblies challenges the understanding of how clustering may impact co-regulation. Studies in *Drosophila* embryos not only identified cell-type-specific chromatin folding^{34,35} but also suggested that enhancer and promoter hubs are often constant across cell types and precede gene activity.^{17,36–38} These findings underscore the uncertainty regarding the extent to which cell-type-specific 3D genome folding directly supports specialized transcriptional programs.

We investigated specialized genome folding in the *Drosophila* central nervous system (CNS) to determine its role in cell-type-specific transcription. Using Micro-C,³⁹ we compared genome folding in the CNS and wing imaginal disc at single-nucleosome resolution and discovered that specific pairs of TADs that are megabases apart interact to form meta-domains predominantly in the CNS. Within meta-domains, 58 high-frequency contacts (“meta-loops”) connect certain neural gene promoters and intergenic accessible chromatin sites. Evolutionary analysis revealed that meta-loops are remarkably robust and specific. Hi-C experiments on neuroblasts, glia, and neurons showed that meta-domains are most prominent in differentiated neurons. We disrupted meta-loops by deleting anchors or mutating transcription factors, GAGA factor (GAF, encoded by the *Trithorax-like* gene) and CTCF, resulting in decreased expression of neural genes at meta-loop anchors. Meta-loops are present in a large fraction of CNS cells but support gene transcription in only a subset. Our findings unveil a previously unrecognized level of genome folding and demonstrate that meta-loops facilitate the longest-range regulatory associations reported to date.

RESULTS

Meta-domains harbor loops involving genes expressed in the CNS

Micro-C analysis of CNSs or wing discs of *Drosophila melanogaster* third instar larvae revealed specific interactions between TADs separated by millions of base pairs (Figures 1A, 1B, S1A, S1B, and S2A; Table S1). These interacting TADs, referred to here as meta-domains, harbored one or several high-frequency interactions within them, referred to here as meta-loops (Figures 1A, 1B, and S1A). Unlike compartmental interactions that reflect segregation of transcriptionally active and inactive genomic compartments, meta-domains represent se-

lective, long-range associations between specific pairs of TADs at high frequencies. In larval CNSs, the normalized Micro-C counts within meta-loops were orders of magnitude higher than background compartmental interactions (Figure 1C). Single-cell assays for transposase-accessible chromatin-sequencing (scATAC-seq) conducted on larval CNSs demonstrated that all loop anchors overlapped accessible chromatin peaks (Figure 1A). Loop anchors also overlapped published DNase I hypersensitive sites (DHS) sequencing (DNase-seq) peaks in mid-embryogenesis neurons but less frequently in muscle cells⁴⁰ (Figures 1A and S2B). These results suggest that transcription factors bind to meta-loop anchors in the CNS.

Using a custom algorithm for automatic meta-loop identification in larval CNS contact maps and manual validation, 58 curated meta-loops were identified (Figure S1A; see STAR Methods). DNase-seq peaks from mid-embryogenesis neurons⁴⁰ were then assigned to meta-loop anchors (Figure 1B). Meta-loops ranged in size between 403 kb and 22.7 Mb (Figure 1D), spanning a chromosome arm in one case but always restricted to individual chromosome arms. In total, 79 identified meta-loop anchors interacted with each other to form 68 loops comprising 58 meta-loops and 10 intra-TAD loops (Figure S1A; Table S2). These 68 loops were present in 28 meta-domains, with most (68%) meta-domains containing clusters of two to six loops (Figure 1E). Among meta-loop anchors, 48% engaged in pairwise interactions, 34% paired with two possible anchors, and 18% potentially interacted with three or four others (Figure S2C). Hi-C demonstrated concurrent three-way interactions between some meta-loop anchors (Figures S2D and S2E).

We compared CNS meta-loops with loops described in *Drosophila* Kc167 cells⁴³ or early embryos.^{25,26} Unlike meta-loops, previously described loops were as follows: detected in different cell types,^{25,26} orders of magnitude smaller (Figure 1D), limited to individual TADs, and used different anchors (Figure S2F) enriched for pioneer factor and Polycomb (Pc) protein binding sites^{25,26,43} (Figure S2G).

Meta-loop anchors were categorized as promoter anchors if the underlying DNase-seq peak was ± 200 bp from a gene transcription start site (TSS) or otherwise as intergenic anchors (IAs) (Figure 1F). Of all 68 loops involving meta-loop anchors, 9 connected two promoter anchors (P-P loops), 25 connected two IAs (I-I loops), and 34 connected an intergenic and a promoter

Figure 1. Meta-domains harbor loops involving CNS-expressed genes

(A) Top: third instar larva wing disc (left) or CNS (right) Micro-C map of chromosome 3L. Dotted squares mark meta-domains. Bottom: Zoom-in on left (in x) and right (in y) anchors of a meta-domain (center) harboring meta-loops L35 and L36. Pseudo-bulk scATAC-seq on larval CNSs, DNase-seq on embryonic neurons and muscles,⁴⁰ mRNA-seq on larval CNSs,⁴¹ and gene tracks (with longest isoforms colored according to transcription direction) are shown. Zoom-ins of 10 kb regions around each meta-loop anchor are shown in dotted rectangles.

(B) Cartoon representation of (A) column 2.

(C) Normalized larval CNS Micro-C count distribution (at 6.4 kb resolution) versus genomic distance of all pairwise contacts on all chromosomes (except Y). Red dots show meta-loops, purple dots show intra-TAD loops involving meta-loop anchors, light and dark gray curves, respectively, show 1–99 or 25–75 percentile ranges of all contact pairs, and the black line shows the median.

(D) Sizes (in bp, in y) of all indicated loop types (points).

(E) Number of meta-domains (in y) each harboring the indicated numbers of loops involving meta-loop anchors (in x).

(F) Distances (in bp, in y) of all 79 meta-loop anchors (points) to the nearest protein-coding gene TSS. The 200 bp line marks the cut-off for defining promoter or intergenic anchors.

(G) Classification of all 58 meta-loops called in larval CNSs (I, intergenic; P, promoter).

(H) RNA-seq on adult fly tissues from FlyAtlas v2.⁴²

See also Figures S1 and S2.

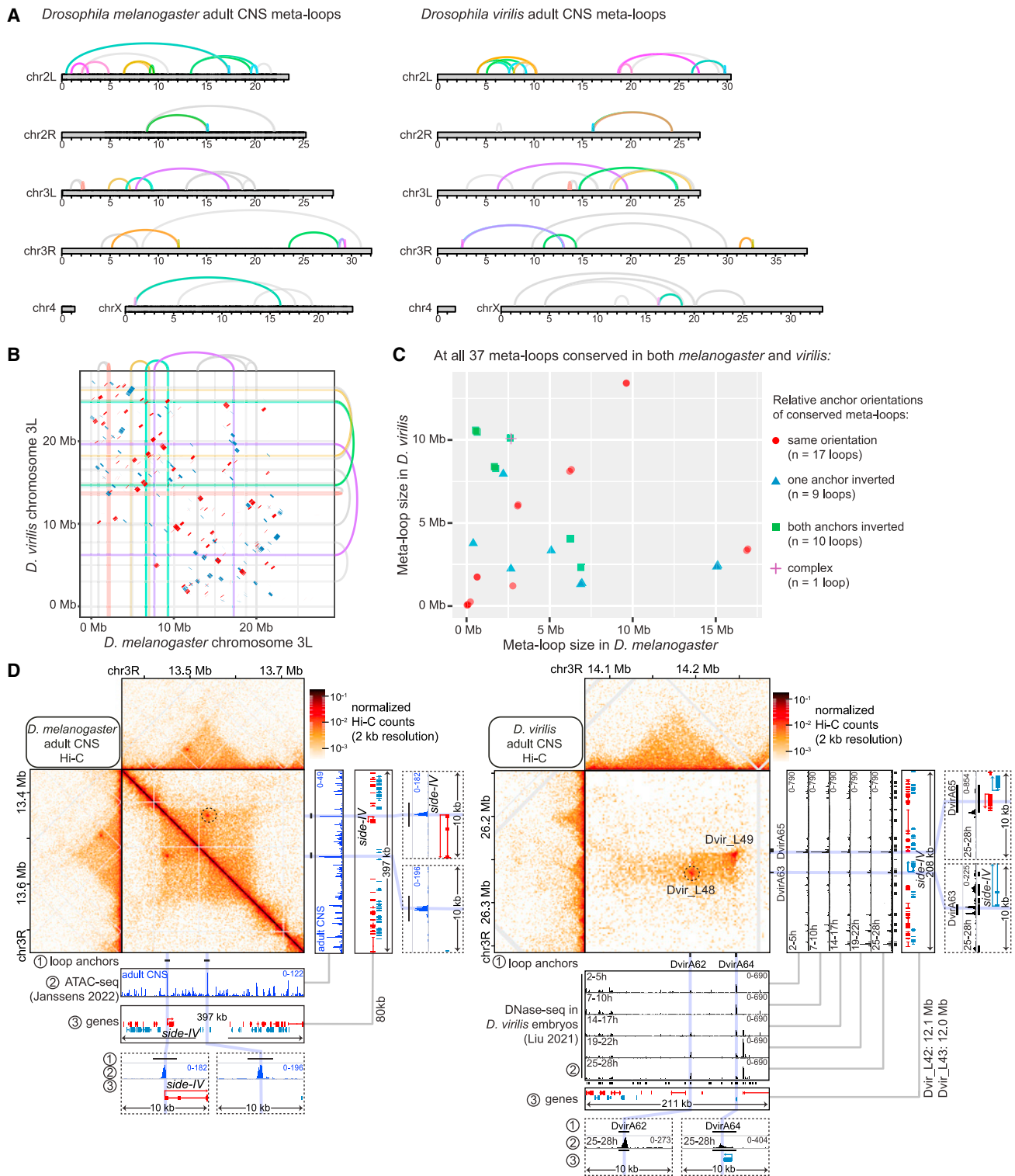


Figure 2. Meta-loop anchors specifically pair over flexible distances in evolution

(A) Loops observed by Hi-C in CNSs of adult *D. melanogaster* (*D. mel.*, left) and *D. virilis* (*D. vir.*, right). For each chromosome arm, conserved loops are uniquely colored (but colors are re-used between chromosome arms) whereas loops present only in *D. mel.* or *D. vir.* are gray. Scale is in Mb.

(B) Dot plot of aligned regions of *D. mel.* (in x) and *D. vir.* (in y) chromosome 3L. Aligned regions in the same orientation are blue, and those that are inverted in one species are red. Conserved loops are colored as in (A) and loop anchors are highlighted (in x and y).

(legend continued on next page)

anchor (I-P loops) (Figure 1G). 6/9 (66%) P-P loops joined paralogous gene promoters (Figure S2H). Genes at promoter anchors are more highly transcribed in adult brains than in other tissues (Figure 1H) and start to be transcribed in differentiating embryonic nervous systems (Figure S2I). These genes encode extracellular or transmembrane proteins involved in axon guidance, including immunoglobulin receptor superfamily members or ion channels specific to neuronal subtypes.⁴⁴ Genes at promoter anchors were significantly enriched for gene ontology (GO) terms related to cell adhesion and axon guidance (Figure S2J). In contrast, genes with TSSs closest to IAs were not enriched for these GO terms (Figure S2J) and were not specifically expressed in the brain (Figure 1H). This suggests that if IAs control transcription, they may affect a gene in a distant TAD to which they loop, rather than a local gene in *cis*.

Meta-loop anchors specifically pair over flexible genomic distances in evolution

We investigated the impact of chromosomal rearrangements on meta-loops during evolution. Hi-C was performed on adult CNSs of *Drosophila melanogaster* and *Drosophila virilis*, with an evolutionary distance comparable with that between humans and lizards⁴⁵ (Figure S3A; Table S1). Using a similar procedure to call meta-loops as in *D. melanogaster*, 84 meta-loop anchors were discovered, which formed 58 meta-loops and 6 intra-TAD loops (Table S3). We examined loop conservation between both species by searching for homologous loop anchor candidates (see STAR Methods). Loop candidates were defined as all pairwise combinations of loop anchor candidates in the other species, for each observed loop. Finally, conserved loops were identified as loop candidates present in both Hi-C maps. Most (61 out of 79) *D. melanogaster* meta-loop anchors mapped uniquely to corresponding *D. virilis* loop anchor candidates (Figure S3B). This homology was not solely driven by coding sequence similarity (Figure S3C). Overall, 37 loops involving meta-loop anchors were conserved in both species, accounting for 54% of *D. melanogaster* loops and 58% of *D. virilis* loops (Figures 2A and S3D). Orthologs of genes closest to *D. melanogaster* meta-loop anchors were often close to homologous meta-loop anchors observed in *D. virilis* (Figures S3E and S3F).

As illustrated for chromosome 3L, conserved loops persisted despite chromosomal breakpoints and inversions (Figure 2B). The lengths of conserved loops varied between *D. melanogaster* and *D. virilis* (Figure 2C), and loop conservation was not limited by loop length (Figure S3G), indicating that loop anchors pair over flexible distances. Loop anchor orientation did not impact loop formation, even at shorter distances (Figures 2B and 2C). Moreover, pairs of loop anchors faithfully looped to each other and rarely to other anchors, highlighting the highly specific pairwise interactions between loop anchors through evolution (Figure S3H). This suggests that dedicated transcription factors bound

to loop anchors mediate distinct loops, a hypothesis explored later in the results section.

In an exceptional case, a meta-loop observed in one species corresponded to an intra-TAD loop in the other species. Although the promoter of the *sidestep IV* (*side-IV*) gene involved in axon guidance⁴⁸ loops to an IA 12 Mb away in *D. virilis* (meta-loop Dvir_L48 in Figure 2D), it loops to a homologous IA 89 kb away within the same TAD in *D. melanogaster* (Figure 2D). A nearby I-I meta-loop (Dvir_L49) in *D. virilis* was not conserved in *D. melanogaster*. This unique example suggests that there might not be strong selective pressure to maintain *side-IV* and its IA in separate TADs. Nonetheless, *side-IV* promoter in *D. melanogaster* remains distant (89 kb) from its IA within the same TAD.

Despite considerable loop conservation, the reason why some loop anchor candidates failed to loop in *D. melanogaster* or *D. virilis* remains unclear. The inability of loop anchor candidates to form a loop could not be attributed to their chromosomal separation between the two species, consistent with previous observations that most chromosomal rearrangements between *D. melanogaster* and *D. virilis* occur within each chromosomal arm.⁴⁹

Meta-loops strengthen during neuronal differentiation

We asked when and where meta-loops emerge in the *D. melanogaster* CNS. Meta-loops were observed in larval and adult CNS Micro-C maps, with certain meta-loops exhibiting greater strength in adults (Figure S1B). Our scATAC-seq dataset in larval CNSs (Figure 1A) and a published scATAC-seq dataset in adult CNSs⁴⁶ revealed that many meta-loop anchors were more accessible in neurons than in glia or neuroblasts (neural stem cells) (Figures S4A and S4B). A published DNase-seq dataset spanning part of embryogenesis⁴⁰ indicated that loop anchor chromatin gradually gained accessibility during neuronal differentiation (Figure S4C). Collectively, these chromatin accessibility analyses suggested that certain meta-loops may be stronger in or specific to differentiated neurons.

To test this hypothesis, we performed Hi-C on neurons, glia, and neuroblasts from embryos at three developmental stages: neuroblast proliferation (6–8 h of development), neural patterning and axon outgrowth (10–12 h), and neuronal terminal differentiation (14–16 h) (Table S1). These cell types were purified by fluorescence-activated cell sorting (FACS) from fixed embryos using antibodies against lineage markers Elav (neurons), Repo (glia), and Wor (neuroblasts) labeled using Multimodal Universal Signal Enhancement (MUSE) technology (Figure S5A). Chromosomes of undifferentiated cells, including neuroblasts from any stage and glia and neurons from 6- to 8-h-old embryos, displayed a Rab1 configuration where centromeres and telomeres cluster at opposite poles and chromosome arms are aligned (Figure 3A row 1 and column 1). The Rab1 configuration was gradually

(C) Sizes of all 37 conserved loops involving meta-loop anchors (colored symbols) plotted in *D. vir.* (in y) versus *D. mel.* (in x). Different symbols represent conserved loops with different relative anchor orientations. The “complex” case is illustrated in Figures S3I and S3J.

(D) Similar to Figure 1A but showing Hi-C maps of a *D. vir.* meta-loop (Dvir_L48) homologous to an intra-TAD loop in *D. mel.* (circled). *D. mel.* adult CNS ATAC-seq from Janssens et al.⁴⁶ or whole *D. vir.* embryo DNase-seq at the indicated hours of development from Liu et al.⁴⁷ are shown below. Anchors of meta-loops called in *D. vir.* were assigned to underlying DNase-seq peaks in old (25–28 h) *D. vir.* embryos.

See also Figure S3.

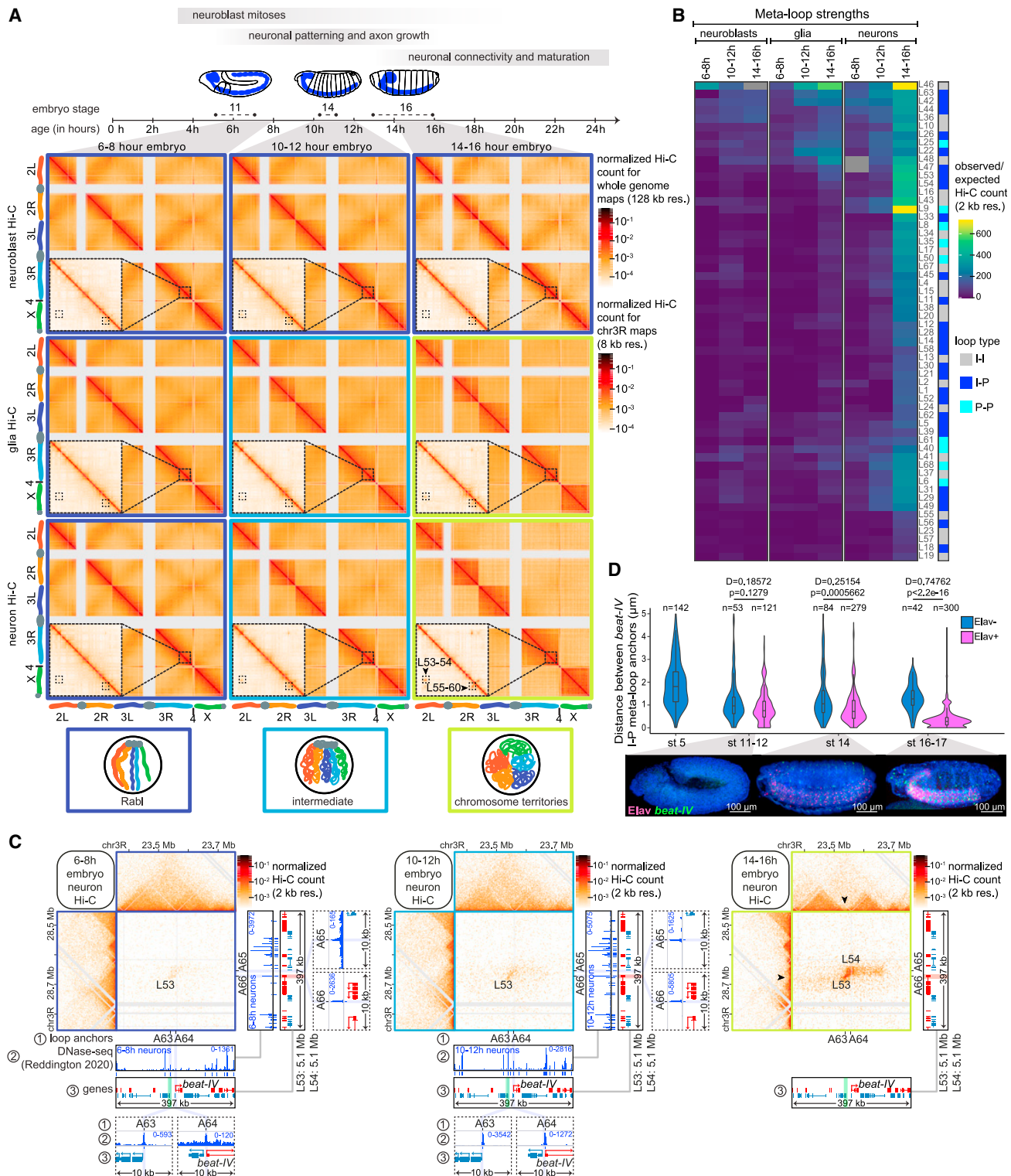


Figure 3. Meta-loop anchors come into enhanced proximity in a large fraction of neurons during neuronal differentiation

(A) Top: hours in embryogenesis, embryonic stages, and major events in neurogenesis. Bottom: Whole-genome Hi-C maps in neuroblasts (row 1), glia (row 2), or neurons (row 3) FACS-purified from embryos of the indicated ages (columns). Dotted squares show zoom-ins around example meta-loops. 3D genome configurations deduced by Hi-C are schematized below and bounded by colored boxes.

(legend continued on next page)

replaced by organization into chromosome territories in neurons and glia from 14- to 16-h-old embryos (Figure 3A). This demonstrates significant genome reorganization during cell differentiation.

Closer inspection revealed that some meta-loops identified in larval CNSs were present in all CNS cell types throughout embryogenesis, whereas other meta-loops specifically emerged in differentiated neurons (Figures 3A and 3B). Although several meta-loops were not exclusive to neurons, most exhibited maximal strength in differentiated neurons (Figure 3B). This trend is exemplified by the 2.6 Mb P-P meta-loop L35 involving the *Glutamate receptor IA and IB (GluRIA-GluRIB)* paralogs, which emerged in mature neurons near a pre-existing I-I loop within the same meta-domain (Figure S5B). The emergence of L35 coincided with the emergence of TAD boundaries that restricted the meta-domain borders (Figures S5B and S5C). Similarly, the 5.1 Mb I-P meta-loop L54 involving the promoter of *beaten path IV (beat-IV)*, involved in motor neuron axon guidance,⁴⁸ emerged in neurons of 14- to 16-h-old embryos near an earlier I-I meta-loop (L53), whose anchor chromatin was accessible earlier than L54 anchor chromatin (Figure 3C). L54 emergence also coincided with the reinforcement of TAD boundaries near meta-loop anchors (Figure 3C). These findings suggest that, particularly during neuronal differentiation, transcription factors occupy meta-loop anchors and participate in meta-looping.

Meta-loop anchors are in enhanced proximity in a large fraction of neurons

To examine the reproducibility of meta-domains across cells, physical distances between the I-P *beat-IV* meta-loop anchors were measured in whole-mount embryos by DNA fluorescence *in situ* hybridization (DNA-FISH). The proportion of nuclei with physically close *beat-IV* meta-loop anchors specifically increased in neuronal nuclei (immunolabeled with α -Elav) as embryos aged (Figure 3D). Meta-loop strengthening observed by Hi-C during neuronal maturation (Figure 3C) thus reflects an increasing proportion of nuclei in which *beat-IV* meta-loop anchors are physically close. The increased proximity of *beat-IV* meta-loop anchors began at the developmental stage coinciding with *beat-IV* transcriptional onset (Figure 3D). *beat-IV* meta-loop anchors were close in most nuclei of late-stage embryonic nerve cords, despite *beat-IV* being transcribed only in a subset of these cells (Figure 3D). Overall, these results indicate that meta-domains are established throughout the embryonic nervous system at the onset of transcription of genes at meta-loop anchors, although expression is restricted to a subset of cells.

To investigate whether meta-loops exist in nuclei independently of the expression of genes at promoter anchors, we compared our Micro-C data in larval CNSs and wing discs. Approximately, one-third of meta-loops were visible in both tissues, although certain shared meta-loops were stronger in larval CNSs compared with wing discs (Figures S1A and S1B). Surprisingly, meta-loops involving a subset of promoter anchors of genes primarily expressed in the CNS were also observed in wing discs (Figure S1; Table S2). One example is the 1.6 Mb I-P meta-loop L22 involving *no long nerve cord (nolo)*, hypothesized to function in the extracellular matrix.⁵⁰ The fact that the *nolo* meta-loop and meta-domain were comparable in CNSs and wing discs (in which *nolo* is not expressed⁴²) indicates that this meta-loop can exist independently of *nolo* transcription.

Meta-domains are formed by meta-loop anchors and delimited by TAD boundaries

To test whether meta-loop anchors are required for meta-domain formation, we deleted 815 or 199 bp overlapping accessible chromatin regions at *nolo* or *beat-IV* IAs. In contrast to most meta-domains (Figure 1E), the *nolo* meta-domain features a single meta-loop (L22, Figure 4A). Hi-C on *nolo* ^{Δ A23} larval CNSs revealed that deleting the IA of the *nolo* meta-loop disrupted the entire meta-domain (Figure 4A). In contrast, Hi-C on *beat-IV* ^{Δ A65} larval CNSs revealed that deleting an anchor of only one of a pair of meta-loops in the *beat-IV* meta-domain was not sufficient to disrupt the meta-domain, which was possibly tethered by the remaining intact meta-loop (Figure 4B).

To test whether deletion of intergenic meta-loop anchors affects transcription of nearby genes, potentially leading to 3D contact changes, mRNA levels of adjacent genes were measured by reverse transcription-quantitative PCR (RT-qPCR). *CG10651* was the only gene in the TAD containing the *nolo* intergenic meta-loop anchor (Figure 4A). Genes around the *nolo* IA are expressed in the male reproductive system⁴² and were not reliably detected in wild-type (WT) or *nolo* ^{Δ A23} mutant heads. mRNA levels measured in whole-bodied adult flies showed no significant change in *nolo* ^{Δ A23} mutants (Figure S6A). Similar observations were made for genes surrounding the deleted anchor in *beat-IV* ^{Δ A65} mutants (Figure S6B). Structural changes in *nolo* and *beat-IV* meta-domains therefore occur without strong transcriptional changes of genes near the deleted meta-loop anchors.

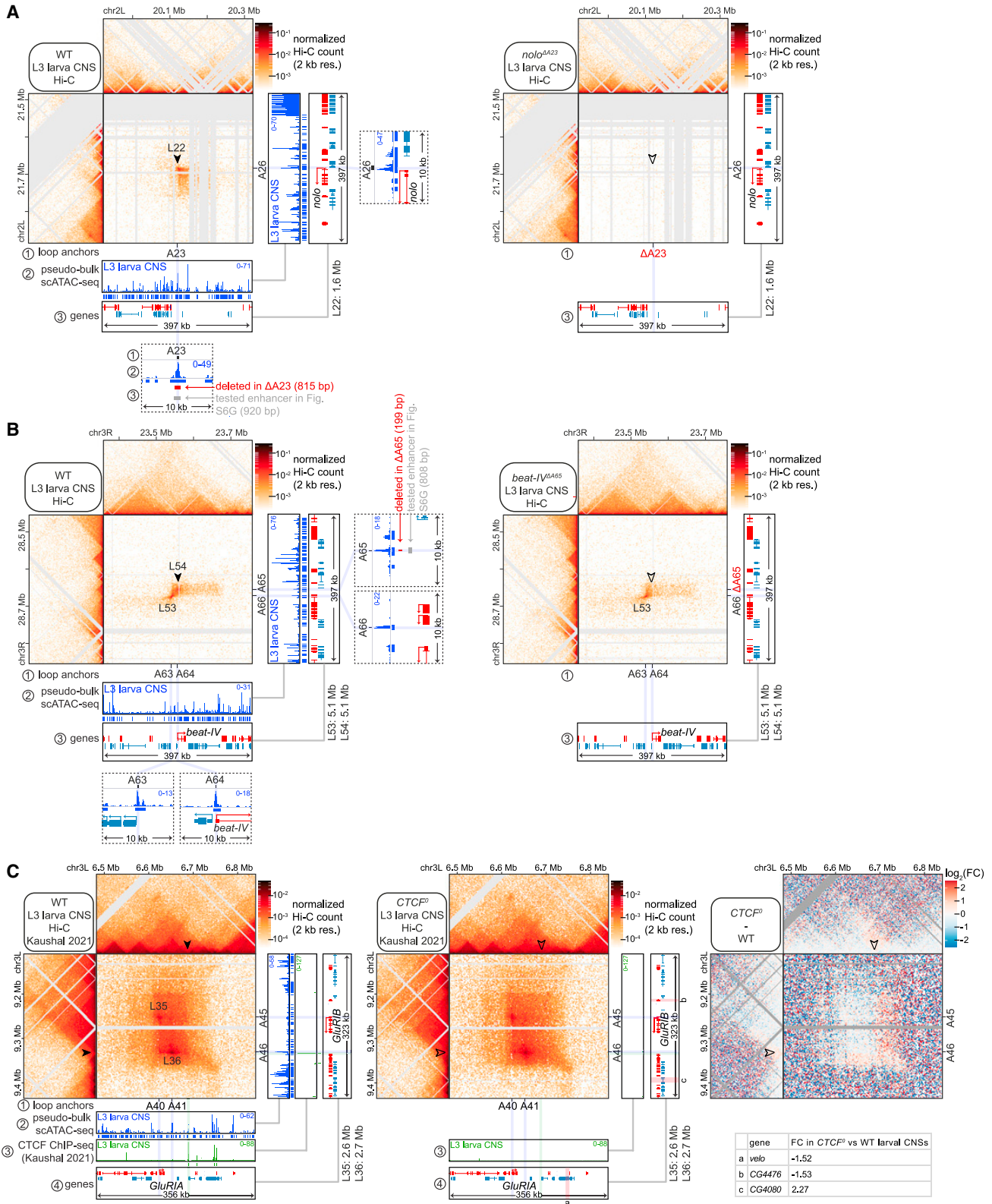
We next asked whether meta-domain borders are established by TAD boundary-forming proteins. CTCF is required to form 10% of TAD boundaries in larval CNSs⁴¹ and determined 5 out of 28 (18%) meta-domain boundaries. The *GluRIA-GluRIB*

(B) For each meta-loop observed in WT larval CNSs (rows), loop strength (color, measured as the observed-over-expected normalized Hi-C count) is shown in each sample (columns). Loop types are color-coded on the right.

(C) Similar to Figure 1A but showing Hi-C maps and DNase-seq profiles in neurons isolated from staged embryos by Reddington et al.⁴⁰ at the *beat-IV* meta-domain, in neurons of 6- to 8-h-old (left), 10- to 12-h-old (middle), or 14- to 16-h-old (right) embryos. Arrowheads mark emerging TAD boundaries near meta-loop anchors. DNA-FISH probes used in (D) are highlighted in green or red in the gene tracks.

(D) Violin plots (central horizontal lines mark medians, boxes mark interquartile ranges) of distances (in y, in μ m) measured by DNA-FISH with probes against *beat-IV* and its intergenic meta-loop anchor, in Elav-immunolabeled (pink) or neighboring (blue) nuclei of embryos of the indicated stages (in x). Below, lateral views of embryos of the indicated stages stained with a probe against *beat-IV* mRNA (green) and α -Elav (pink) (anterior, left; posterior, right). p values and D-statistics from two-sided Kolmogorov-Smirnov tests are indicated.

See also Figures S4 and S5.



(legend on next page)

meta-domain's right and bottom borders were bound by CTCF in larval CNSs of WT but not *CTCF*⁰ animals lacking maternal and zygotic CTCF (Figure 4C).⁴¹ In *CTCF*⁰ mutants, these borders were weakened, and the meta-domain expanded to the next TAD boundaries. Expanding the *GluRIA-GluRIB* meta-domain in *CTCF*⁰ mutants did not strongly affect gene expression within the meta-domain, as assessed by RNA sequencing (RNA-seq) on WT and *CTCF*⁰ mutant larval CNSs⁴¹ (Figure 4C). 48% of meta-loop anchors were within one genomic bin of a TAD boundary called by Hi-C in WT larval CNSs,⁴¹ including both promoter and IAs (Figure S5C). Examples showed meta-loop anchors coinciding with TAD boundaries in WT (e.g., A46 in Figure 4C), but boundary and meta-looping functions were separable in *CTCF*⁰ mutants, indicating dispensability of meta-looping factors for boundary formation in these cases.

These results collectively suggest that meta-domains are tethered by meta-loops and set by TAD boundaries.

An intergenic meta-loop anchor enables distal activation of *nolo*

To investigate whether *nolo* and *beat-IV* IAs are required for transcription of these genes, we measured their mRNA levels in adult fly heads by RT-qPCR. This revealed a 3-fold decrease in *nolo* mRNA levels in *nolo*^{ΔA23} mutants compared with WT, whereas *beat-IV* mRNA levels remained unchanged in *beat-IV*^{ΔA65} mutants (Figures S6A and S6B). Deletion of anchor A23 therefore did not significantly impact the expression of nearby genes in *cis* but decreased *nolo* expression over 1.6 Mb (Figure S6A). To further investigate transcriptional defects, single-cell RNA-seq (scRNA-seq) was performed on larval CNSs from WT, *nolo*^{ΔA23}, and *beat-IV*^{ΔA65} mutants (Figures 5A and S6C). *nolo* and *beat-IV* were expressed in different cell subsets in WT CNSs (11% and 9% of WT cells, respectively) (Figure 5B). In *nolo*^{ΔA23} mutants, *nolo* was expressed in fewer cells (2%) and at lower levels, whereas *beat-IV* expression remained relatively stable in *beat-IV*^{ΔA65} (Figure 5C). Differential expression analysis per cell cluster in each mutant relative to WT revealed significant differential expression (adjusted p value ≤ 0.01) of *nolo* in three *nolo*^{ΔA23} mutant clusters, whereas *beat-IV* was unaffected in any cluster or genotype (Figure 5C; Tables S4 and S5). Thus, deleting one gene's intergenic meta-loop anchor did not impact the meta-loop or the expression of the other gene (Figures 5C and S6D), revealing their independence.

nolo RNA-FISH signals were strongly reduced in embryonic nerve cords of *nolo*^{ΔA23} mutants compared with WT (Figure 5D). To assess if decreased *nolo* mRNA levels in *nolo*^{ΔA23} mutants resulted from reduced *nolo* transcription, we imaged *nolo* nascent RNA and *nolo* promoter DNA by RNA-DNA-FISH (Figures 5E and S6E). Counting *nolo* promoter DNA-FISH spots with or without

co-localizing nascent *nolo* RNA-FISH signal in late-stage (stage 17) embryonic nerve cords revealed that *nolo* was transcribed in 28% of WT nuclei but only in 7% (4-fold less) of *nolo*^{ΔA23} nuclei (Figure 5E). Thus, deletion of the *nolo* IA decreases *nolo* transcription.

To investigate whether IAs may facilitate neural gene transcription by serving as distal enhancers, we tested five intergenic loop anchors (550–999 bp) for their ability to activate reporter gene transcription in WT transgenic reporter embryos when cloned upstream of the minimal *Drosophila* synthetic core promoter (DSCP) and integrated into a common landing site (Figures S6F and S6G). Reporter gene RNA-FISH on embryos homozygous for each transgene revealed that only the IAs of *beat-IV* (A65) and *nolo* (A23) were moderate and weak enhancers, respectively, active in the nervous system of late-stage embryos (Figure S6G). Deletion of the *beat-IV* IA did not visibly affect *beat-IV* expression in larval CNSs (Figures 5C and S6B), implying that *beat-IV* transcription in larval CNSs relies on other uncharacterized enhancers. Of note, the enhancer reporter transgenes were integrated into a different chromosomal arm (chr3L) from that housing *nolo* or *beat-IV* meta-loops to prevent potential confounding looping between the transgenic and endogenous anchors.

In summary, the *nolo* IA is critical for *nolo* transcription. However, the tested I-P meta-loops are not classical enhancer-promoter loops, as most IAs show limited enhancer activity (Figure S6G). It is possible that *beat-IV* expression in *beat-IV*^{ΔA65} mutants is sustained by distal regulatory elements within the preserved meta-domain due to the intact meta-loop (Figure 4B). This hypothesis is tested in the last results section.

To determine whether *nolo*^{ΔA23} mutation affects *nolo* function, we compared the lethal stages of *nolo*^{ΔA23} and *nolo*^{KO} mutants with nonsense mutations after codons 47 or 48 (Figures 5F and 5G). *nolo*^{KO} and *nolo* whole-body or neuroblast-specific knockdown pupae showed impaired eclosion that was not observed in *nolo*^{ΔA23} mutants (Figure 5G). In *nolo* knockdown flies, the *nolo*^{ΔA23} mutation decreased pupal eclosion further (e.g., from 66% upon neuroblast-specific *nolo* knockdown to 11% when performed in a *nolo*^{ΔA23} mutant) (Figure 5G). We analyzed neuromuscular junctions (NMJs) of *nolo* knockout, knockdown, and *nolo*^{ΔA23} third instar larvae. α -horseradish peroxidase (HRP) immunostaining of neuronal membranes at muscle 6/7 NMJs revealed that the NMJ area and the number of synaptic boutons were significantly reduced in *nolo*^{KO}, *nolo*^{ΔA23}, and *nolo* knockdown flies compared with WT controls (Figures 5H and 5I), suggesting that NMJs are underdeveloped or impaired. Thus, *nolo*^{ΔA23} is a hypomorphic *nolo* allele with similar NMJ defects to those observed in *nolo* knockout and knockdown animals.

Figure 4. Meta-domains are formed by meta-loop anchors and delimited by TAD boundaries

(A) Similar to Figure 1A but showing Hi-C maps of the *nolo* meta-domain in WT (left) or *nolo*^{ΔA23} (right) larval CNSs. Filled/empty arrowheads point to meta-loop L22 presence/absence in each genotype. The extents of meta-loop anchor A23 deletion or testing for enhancer activity in Figure S6G are indicated below.

(B) Same as (A) but for the *beat-IV* meta-domain in WT (left) or *beat-IV*^{ΔA65} mutants (right).

(C) Similar to (A) but also showing CTCF ChIP-seq profiles and called peaks at the *GluRIA-GluRIB* meta-domain in WT (left) or *CTCF*⁰ (middle) larval CNSs.⁴¹ Filled/empty arrowheads mark normal/weakened TAD boundaries in each genotype. A differential (*CTCF*⁰ minus WT) Hi-C map is shown on the right (scale is log₂ fold change of contacts). Differentially expressed genes defined by RNA-seq in *CTCF*⁰ relative to WT larval CNSs (padj < 0.05 and [fold change] > 1.5)⁴¹ are highlighted in pink and labeled with a letter on the gene track in the middle, and the fold changes are indicated in the table.

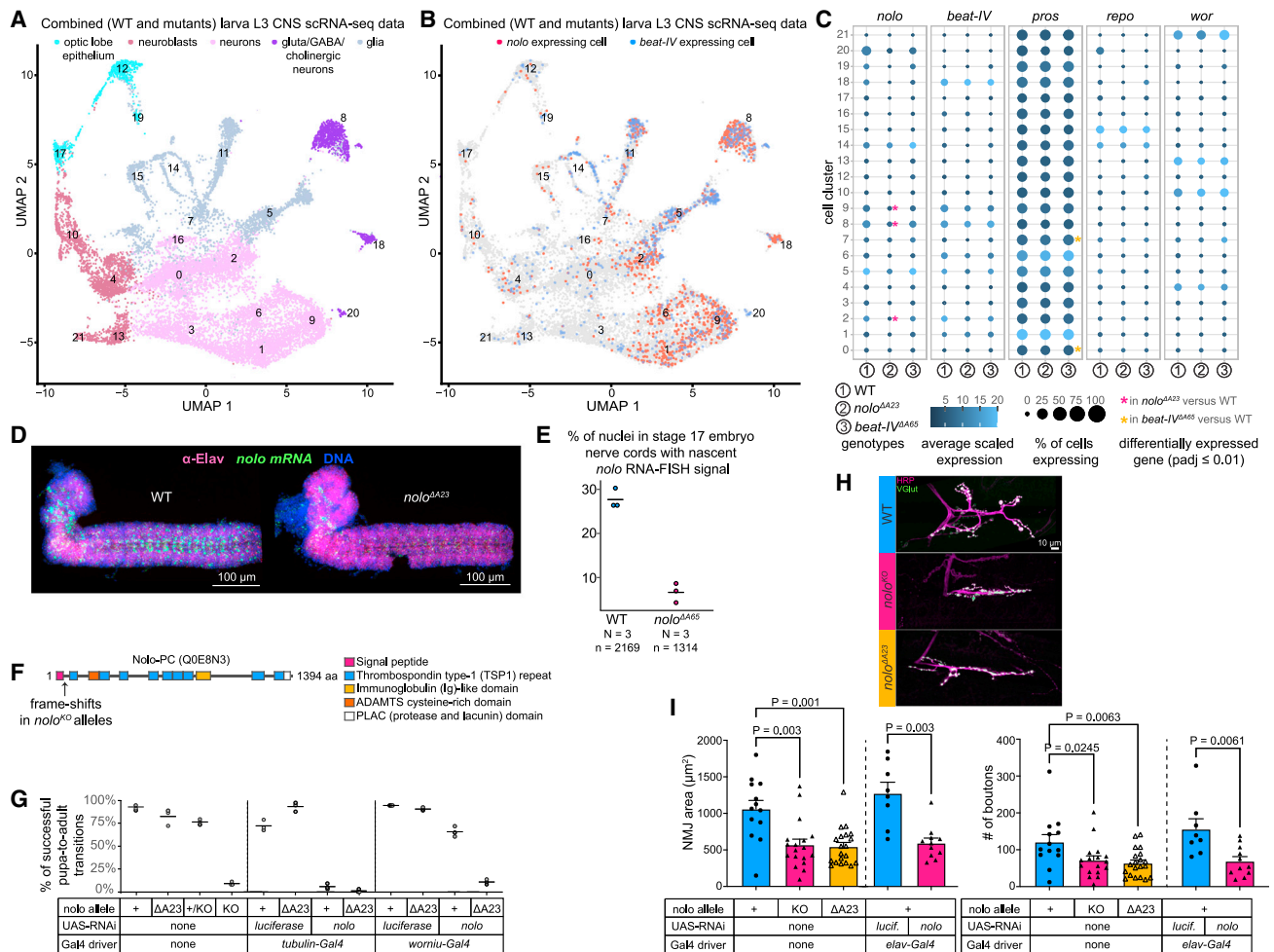


Figure 5. An intergenic anchor enables distal activation of *nolo*

(A) Combined scRNA-seq datasets generated in WT, *nolo*^{ΔA23}, and *beat-IV*^{ΔA65} third instar larval CNSs. Cell clusters are numbered, and major cell types color-coded.

(B) Same as (A) but coloring cells expressing *nolo* (red) or *beat-IV* (blue).

(C) For each cell cluster, the percentage (circle size) of cells expressing the indicated genes (columns) and the average scaled expression (color) are shown in WT (1), *nolo*^{ΔA23} (2) or *beat-IV*^{ΔA65} (3) larval CNSs. Cells from cluster 11 were variably recovered between samples and were excluded. *pros*, *repo*, and *wor* are respectively neuronal, glial, and neuroblast markers. Asterisks mark cell clusters that significantly ($p_{adj} \leq 0.01$) differentially expressed the indicated gene in *nolo*^{ΔA23} (red asterisk) or *beat-IV*^{ΔA65} (orange asterisk) mutants relative to WT.

(D) RNA-FISH with a probe against *nolo* mRNA (green) in dissected nerve cords of stage 16 WT and *nolo*^{ΔA23} mutant embryos immunostained with α -Elav (pink) (anterior, left; posterior, right). Reduced *nolo* expression shown here was observed in 100% of *nolo*^{ΔA23} mutants (≥ 10 embryos imaged per genotype).

(E) Percentage (in y) of nuclei with *nolo* promoter DNA-FISH signal that overlapped nascent *nolo* RNA-FISH signal in nerve cords of stage 17 WT (left) or *nolo*^{ΔA23} (right) mutant embryos (dots). Horizontal lines show means. N, number of embryos; n, number of nuclei with DNA-FISH signal scored.

(F) Schematic of the longest Nolo protein isoform (Uniprot accession Q0E8N3). Protein domains and positions of premature stop codons present in *nolo*^{KO} alleles are marked.

(G) Percentages of indicated genotypes that successfully developed from pupae to fully eclosed adults in three independent batches of 30–40 animals (dots). Horizontal lines show means.

(H) Immunostaining of synaptic boutons (α -Vesicular glutamate transporter [VGlut]) and the whole neuromuscular junction (α -HRP) in muscle 6/7 terminals in WT and the indicated *nolo* mutant third instar larvae. Representative images are shown, and results from several images are quantified in (I).

(I) Quantification of neuromuscular junction (NMJ) area (left) and numbers of synaptic boutons (right) from $n \geq 8$ larvae (data points) of the indicated genotypes. Bar plots show average values, error bars show standard deviation. p values from one-way ANOVA (for wild-type versus mutant comparisons) or unpaired two-sided t tests (for *luciferase* to *nolo* knockdown comparisons) are indicated.

See also Figure S6.

GAF is required to form two specific meta-loops

A comprehensive analysis of all meta-loop anchors did not reveal enriched transcription factor motifs. GAF is required to form a subset of chromosomal loops between tethering elements in embryos in a manner dependent on its BTB (broad-complex, tram track, and bric-à-brac—zinc finger, also known as POZ) domain.⁵¹ To investigate GAF's potential role in meta-loop formation, we performed Micro-C on WT and *GAF^{ΔBTB}* mutant larval CNSs.⁵² The GAF BTB domain was specifically required to form two ~6 Mb meta-loops connecting the promoter of *sticks and stones* (*sns*) with that of *hibris* (*hbs*) (L25) or with an IA (L26) (Figures 6A and 6B). GAF ChIP-seq data in larval tissues, comprising the CNS,⁵³ revealed lower enrichment of GAF binding around meta-loop anchors compared with anchors of loops detected in embryos and cultured cells (Figure 6C). Nonetheless, GAF bound to a subset of meta-loop anchors, and A29, the common anchor of both GAF-dependent meta-loops, was most strongly bound by GAF (Figures 6A and 6C). Thus, both meta-loops destabilized in *GAF^{ΔBTB}* mutants have relatively strong GAF binding at their anchors in WT, whereas other meta-loops with anchors that are less bound or unbound by GAF are unaffected (Figures 6B and 6C). The long-range interaction between *sns* and *hbs* is not limited to the CNS (Figure S1) and was also previously observed in whole embryos (WE),^{54,55} suggesting a non-CNS-specific role of GAF in forming these meta-loops.

Visualization of *sns* and *hbs* mRNAs by *in situ* hybridization chain reaction (HCR) revealed a moderate decrease in *sns* expression in a stripe in optic lobes of *GAF^{ΔBTB}* mutants, whereas *hbs* expression was mostly unchanged (Figure 6D). These observations were further supported by RT-qPCR on larval CNSs (Figure 6E). These results indicate that GAF is required to form meta-loops involving *sns* promoter and for WT levels of *sns* transcription in larval CNSs.

CTCF is required to form a different subset of meta-loops than GAF in the CNS

Comparison of WT and *CTCF⁰* mutant larval CNS Hi-C maps⁴¹ identified six meta-loops that were significantly weakened in *CTCF⁰* mutants compared with WT (Figures 7A, 7B, and S7A), and these were unaffected in *GAF^{ΔBTB}* larval CNSs (Figure 6B). CTCF-dependent meta-loops were identified in CNSs but not wing discs (Figure S1). Although CTCF generally binds constitutively in different cell types,⁴⁰ the chromatin of CTCF-bound meta-loop anchors was more accessible in embryonic neurons than muscle (Figures 7C and S7A).

Surprisingly, the *beat-IV* meta-domain was weakened in *CTCF⁰* mutant larval CNSs even though CTCF only binds to the anchors of meta-loop L53 but not L54, which connects *beat-IV* promoter to its IA (Figures 7A and 7D). This suggests that L53 loss in the absence of CTCF may destabilize L54 in the same meta-domain. No genes within the *beat-IV* meta-domain were significantly differentially expressed in *CTCF⁰* mutant relative to WT larval CNSs by RNA-seq⁴¹ (Figure 7A). We further examined *beat-IV* expression in WT and *CTCF⁰* embryos by RNA-FISH. In WT embryos, *beat-IV* expression is detected throughout the nerve cord at stage 15 and increases at stage 16 (Figure 7E). In *CTCF⁰* embryos, *beat-IV* expression

was strongly reduced at stages 15–17 except for a few bright cells in the center of the nerve cord (Figure 7E). CTCF recruits its BTB-ZnF cofactor, Centrosomal protein 190 kDa (Cp190) to CTCF binding sites.⁴¹ Consistently, Cp190 co-bound with CTCF at L53 anchors in WT but was either reduced or absent at these anchors in *CTCF⁰* larval CNSs (Figures 7A and 7D). Cp190 is, in contrast, largely dispensable for CTCF binding to DNA,^{20,41} and CTCF was bound at WT levels at L53 anchors in *Cp190^{KO}* (maternal+ zygotic–) larval CNSs (Figure S7B). In *Cp190⁰* (maternal– zygotic–) embryos, *beat-IV* expression was reduced to an even greater extent than in *CTCF⁰* embryos (Figure 7E). In contrast, in *beat-IV^{ΔA65}* mutants with a deletion of the IA looping to *beat-IV* promoter (Figure 4B), *beat-IV* expression was largely normal (Figure 7E).

We also investigated a second CTCF-dependent meta-domain containing two 2.2 Mb meta-loops normally both bound by CTCF in WT (Figure S7B). L33 connects two IAs and L34 connects the promoter of Multiplexin (*Mp*) to an IA (Figure S7A). RNA-seq analysis revealed an 11-fold upregulation of the gene *CG7509* within the *Mp* meta-domain in *CTCF⁰* mutants compared with WT larval CNSs (Figure S7A).⁴¹ We further examined *Mp* expression in embryos by RNA-FISH. In WT embryos, *Mp* is expressed in the posterior nerve cord at stage 15 and expands to the anterior nerve cord at stage 16 (Figure S7C). In *CTCF⁰* embryos, *Mp* expression appeared normal at stage 15 but failed to expand anteriorly in stage 16, resembling the expression pattern of stage 15 embryos (Figure S7C). In *Cp190⁰* embryos, *Mp* was expressed in much fewer cells at stage 15 and partially recovered in the posterior nerve cord at stage 16 but remained lower than WT in the anterior nerve cord similar to *CTCF⁰* embryos (Figure S7C).

In conclusion, the destabilization of distinct meta-loops in *GAF^{ΔBTB}* and *CTCF⁰* mutants suggests that specific transcription factors are recruited to different meta-loop anchors, ensuring interaction specificity. Loss of CTCF or Cp190 delays and reduces the transcriptional activation of neuronal genes in a CTCF-dependent meta-loop (*Mp*) and meta-domain (*beat-IV*).

DISCUSSION

We studied genome folding in the developing *Drosophila* CNS and discovered long-range associations between specific pairs of TADs. We propose that meta-domains represent a previously unrecognized paradigm of genome folding that enables coordinated megabase-range control of gene transcription in the CNS. Below, we discuss the implications of these findings.

Specialized chromosomal folding can support cell-type-specific gene expression

Recent studies have explored cell-type-specific genome folding in the mammalian nervous system. Differential genome folding was observed between brain cell types and during differentiation, resulting in altered TAD boundaries, differential enhancer-promoter contacts, and increased inactive B compartment interactions.^{10,30,56} The most striking long-range contacts occurred in *cis* (over up to 50 Mb) and *trans* between heterochromatinized silent olfactory receptor (OR) gene clusters on the one hand and between OR enhancer clusters and the single active OR allele on the other, in neurons.^{11,30} Clustering of OR genes

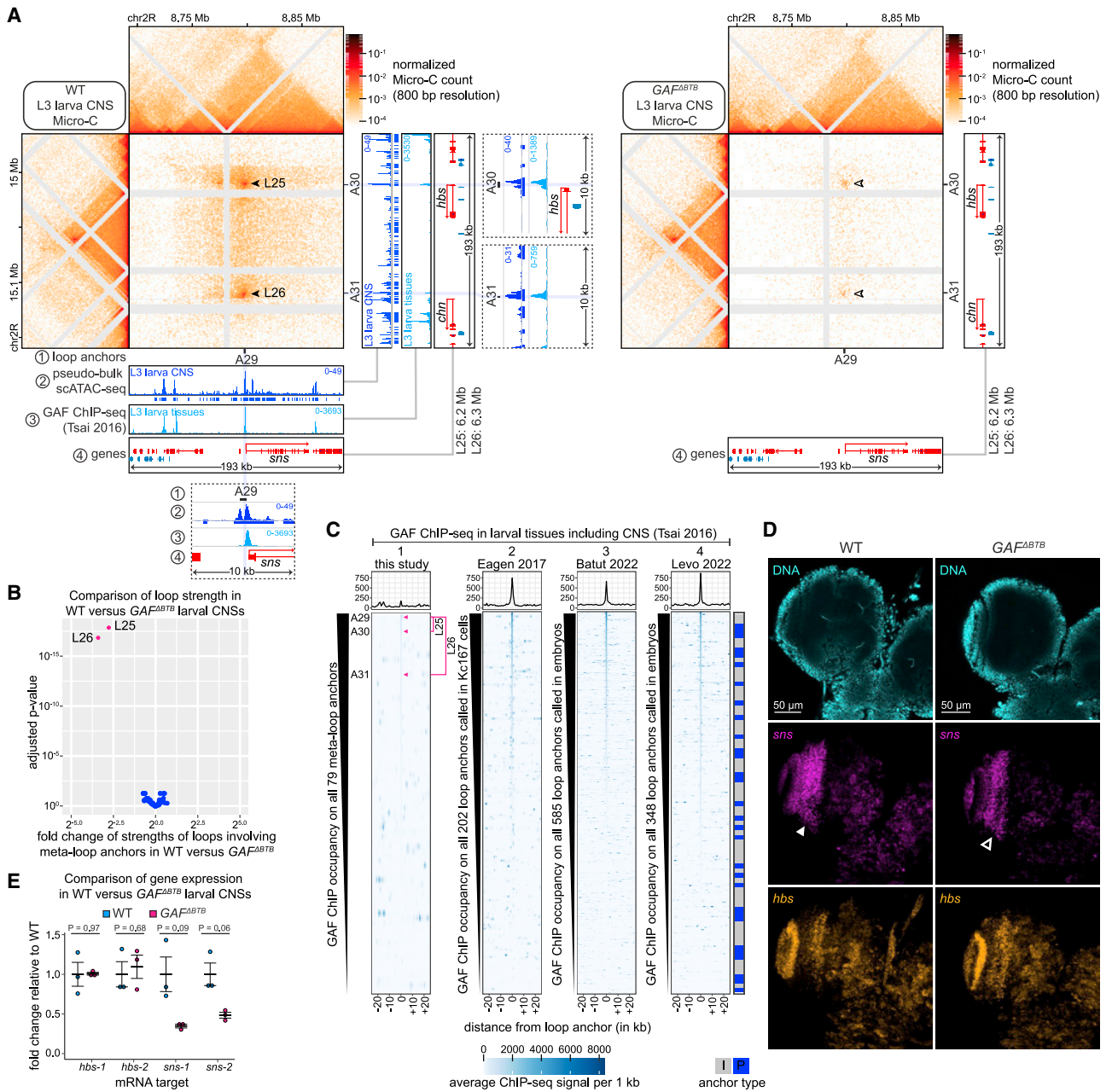


Figure 6. The GAF BTB domain is required to form the *sns-hbs* meta-domain

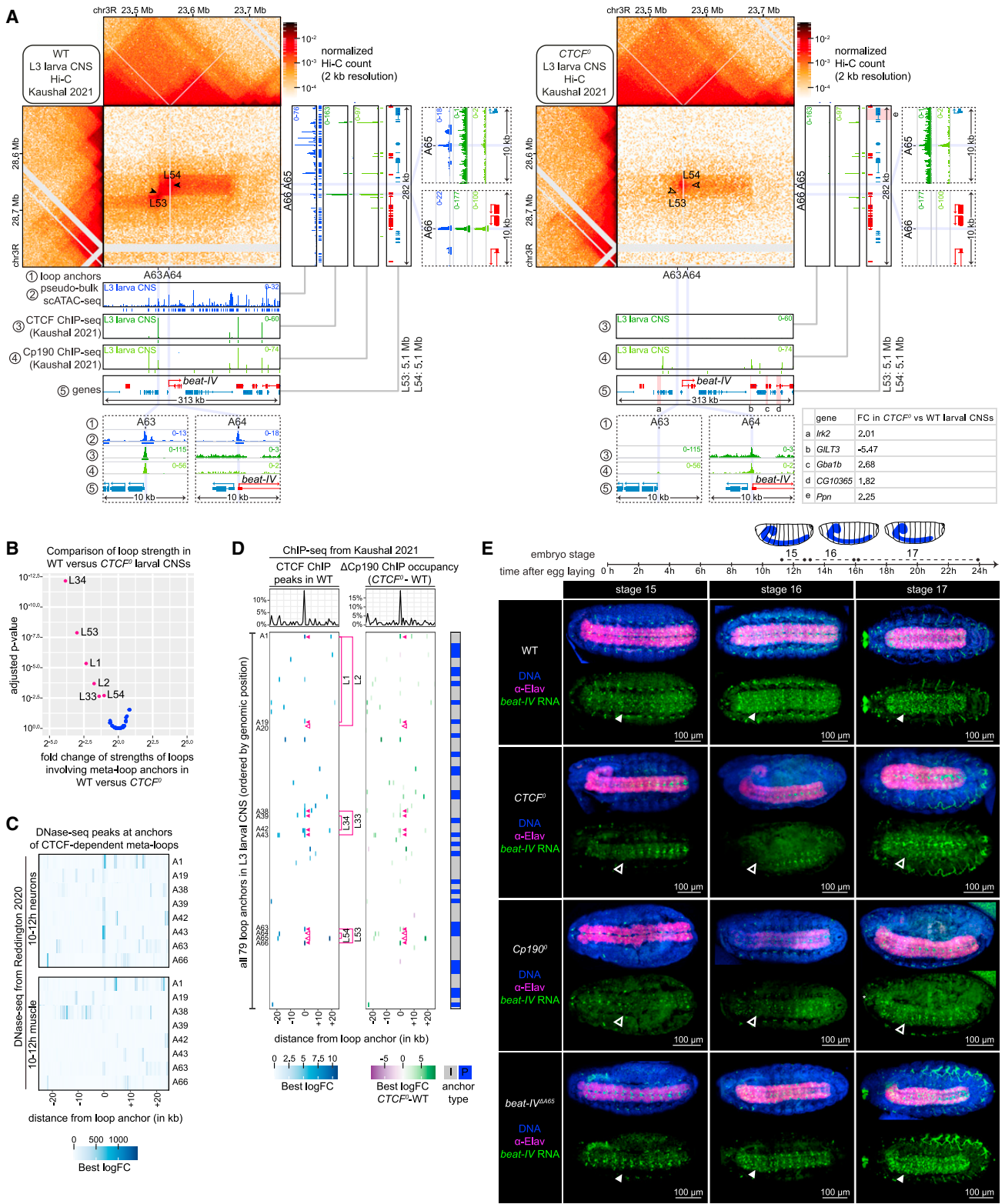
(A) Similar to Figure 1A but also showing GAF ChIP-seq profiles in larval tissues including the CNS⁵³ at the *sns-hbs* meta-domain in WT (left) and $GAF^{\Delta BTB}$ (right) larval CNSs. Filled/empty arrowheads point to WT/reduced meta-loop strength in each genotype.

(B) Differential analysis of strengths of loops involving meta-loop anchors (dots) measured by Micro-C in WT versus $GAF^{\Delta BTB}$ larval CNSs. Labeled loops (pink dots) were significantly weaker ($p_{adj} \leq 0.01$) in $GAF^{\Delta BTB}$ compared to WT.

(C) Distribution of GAF ChIP-seq signal in larval tissues including CNS⁵³ in 1-kb bins ± 25 kb around all anchors of meta-loops (lane 1) or loops previously defined in tissue culture cells (lane 2) or embryos (lanes 3 and 4) ranked by GAF ChIP occupancy. Average signals over all loop anchors are shown above.

(D) HCR RNA-FISH with co-hybridized probes against *sns* (magenta) and *hbs* (yellow) mRNAs in WT (left) and $GAF^{\Delta BTB}$ (right) larval CNSs. Filled/empty arrowheads mark a stripe with WT/reduced *sns* expression in each genotype. This phenotype was observed in 100% of $GAF^{\Delta BTB}$ mutants (≥ 10 larval CNSs imaged per genotype).

(E) Fold change of *hbs* and *sns* mRNA levels measured by RT-qPCR with two independent primer pairs each, in $GAF^{\Delta BTB}$ relative to WT larval CNSs. Dots represent individual biological triplicate values, thick horizontal bars represent average values, and error bars indicate standard deviation. p values from two-sided unpaired t tests are shown.



(legend on next page)

was crucial for activating a single OR allele,⁵⁷ but deletion of an OR enhancer cluster largely only affected the transcription of OR genes in *cis*.¹¹ The lack of clear defects in distal OR gene activation suggests that OR enhancers act redundantly and compensate for deletions of other enhancer clusters.¹¹ By contrast, the specificity of *Drosophila* CNS meta-domain associations uncovered examples of megabase-scale gene regulation.

Meta-loop function

Three lines of evidence support the functional relevance of meta-loops in CNS development and function. First, deleting the *nolo* intergenic loop anchor disrupted the meta-domain and reduced *nolo* transcription over 1.6 Mb (Figures 4A and 5). Second, *GAF^{ΔBTB}* mutants displayed a notable loss of 6.2 Mb meta-loops involving the *sns* promoter and decreased *sns* expression (Figure 6). Third, CTCF loss weakened three CNS-specific meta-domains and decreased the expression of *beat-IV* and *Mp* located at meta-loop anchors (Figures 7 and S7). Of note, the expression of two genes at (*Mp*) or near (*CG7509*) opposite meta-loop anchors was oppositely affected in *CTCF⁰* mutant CNSs, potentially suggesting coordination of gene expression over 2.2 Mb (Figures S7A and S7C). Together, these findings indicate that gene expression in the CNS is controlled over longer distances than those previously described in the mammalian genome, such as *SOX9* activation by its enhancer 1.5 Mb away in the cranial neural crest of mice and humans.⁵⁸

Our observation of reduced *beat-IV* expression in *CTCF⁰*, but not *beat-IV^{ΔA65}*, mutants suggests that the *beat-IV* meta-domain, and not the *beat-IV* meta-loop itself, is important for *beat-IV* expression (Figures 5C and 7E). Meta-domains may facilitate the sharing of regulatory information between distant TADs. Investigating the impact of meta-domain boundary perturbations on the expression of genes at meta-loop anchors would provide valuable insights.

Our findings suggest that meta-loops are formed through long-range focal contacts of structural elements rather than enhancer-promoter loops. Unlike enhancer-promoter interactions, which correlate with active transcription,^{40,59} and like tethering elements that bridge promoters to distal regulatory elements in fly embryos and mammalian cells, meta-loop anchors lack robust enhancer activity (Figure S6G) and pair in more cells than those that transcribe the associated gene (Figures 3D and S1).^{23,25,26,60} However, tethering element activity is generally

constrained to individual TADs,^{23,25,26} whereas CNS meta-loops span tens of TADs. Meta-loops reconcile contrasting views of 3D genome folding as either invariant scaffolds^{17,25,26,36,37} or tissue-specific structures by demonstrating that specialized and relatively invariant scaffolds exist within neurons.

Mechanism of meta-loop formation

Our findings indicate that meta-domains are tethered by meta-loops, and not by compartmental interactions (Figures 1 and 4), that pair over long and flexible genomic distances with striking specificity (Figure 2) and rely on dedicated transcription factors including GAF and CTCF (Figures 6 and 7) for their formation.

In contrast to GAF, which is required to form a meta-domain that is also observed outside of the CNS (Figures 6 and S1),^{54,55} CTCF was required to form three CNS-specific meta-domains (Figures 7 and S1). Our previous finding that CTCF is specifically required in neurons for fly viability⁴¹ suggests that CTCF plays a specialized role in the CNS that includes meta-domain formation. Differentiating neurons may express additional factors that cooperate with CTCF at meta-loop anchors. It should be noted that although CTCF is required for meta-loop formation, it cannot be the sole factor responsible, as weak meta-domains persist in *CTCF⁰* CNSs despite complete loss of CTCF⁴¹ (Figures 7A and S7A). Cp190 may also be required, as partial meta-domain retention in *CTCF⁰* mutants correlates with partial Cp190 retention at meta-loop anchors. The severe effect of Cp190 loss on *Mp* and *beat-IV* gene expression compared with CTCF loss may further suggest an important role of Cp190 in meta-loop formation (Figures 7E and S7C). GAF and Cp190 belong to the same BTB-ZnF protein family and possibly share a mechanism for meta-loop formation. Investigating the effect of Cp190 loss on meta-domain formation will therefore be crucial. Another possibility is that CTCF or Cp190 collaborate with other essential factors to form meta-domains.

Most meta-domains contain clustered loops (Figure 1E). In *beat-IV* (Figure 3C) and *GluRIA-GluRIB* (Figure S5B) meta-domains, an I-I meta-loop emerged earlier in neuronal differentiation than the I-P or P-P meta-loop. Deleting the IA connected to *beat-IV* promoter did not disrupt the *beat-IV* meta-domain (Figure 4B). However, destabilizing the earlier CTCF-bound I-I meta-loop by CTCF loss also destabilized the I-P meta-loop (not directly bound by CTCF) and the entire *beat-IV* meta-domain (Figure 7). These results suggest a hierarchy in long-range

Figure 7. CTCF is required to form a different set of meta-loops than GAF

(A) Same as Figure 4C but also showing Cp190 ChIP-seq profiles and called peaks⁴¹ at the *beat-IV* meta-domain in WT (left) or *CTCF⁰* (right) larval CNSs.
 (B) Differential analysis of strengths of loops involving meta-loop anchors (dots) measured by Hi-C in WT versus *CTCF⁰* larval CNSs. Labeled loops (pink dots) were significantly weaker ($\text{padj} \leq 0.01$) in *CTCF⁰* compared with WT.
 (C) Distribution of DNase-seq signal from Reddington et al.⁴⁰ around the anchors of CTCF-dependent meta-loops shown in (B), in 500-bp bins ± 25 kb around these anchors ordered by genomic position, in 10- to 12-h-old embryonic neurons (top) or muscle (bottom).
 (D) Distribution of CTCF ChIP-seq peaks and differential Cp190 ChIP-seq occupancy (colored by average best.logFC) in *CTCF⁰* versus WT larval CNSs (data from Kaushal et al.²⁰) in 1-kb bins ± 25 kb around all meta-loop anchors ordered by genomic position. Percentages of meta-loop anchors with at least one CTCF ChIP peak or differential Cp190 binding region in WT versus *CTCF⁰* mutants over all anchors are shown on top. Pink filled/empty arrowheads indicate anchors of meta-loops weakened in *CTCF⁰* that are bound/not bound by CTCF. These anchors are labeled on the left and meta-loops are labeled on the right.
 (E) Ventral views of embryos of indicated genotypes (rows) and stages (columns) stained with a probe against *beat-IV* mRNA (green) and α -Elav (pink) (anterior, left; posterior, right; merged images on top). Specific RNA-FISH signal appears as dots; string-like and broad green non-specific signal is visible in trachea and epidermis. Filled/empty arrowheads point to WT/reduced *beat-IV* RNA-FISH signal in each genotype. Phenotypes shown here were observed in 100% of embryos (≥ 6 embryos imaged per genotype and stage).

See also Figure S7.

associations, where a meta-loop can facilitate the emergence of another meta-loop in the same meta-domain.

Moreover, we observe a previously unrecognized interplay between certain meta-loop anchors and TAD boundaries that appear to emerge concomitantly during neural differentiation, although the temporal resolution of our time-course Hi-C experiments is limited (Figures 3C, S5B, and S5C). It will be important to determine whether TAD boundaries may facilitate meta-domain emergence at specific loci, although TAD boundaries at other loci can be shifted without affecting meta-domain formation (Figure 4C).

Meta-loops differ from traditional models of chromosome folding, which involve cohesin-mediated loop extrusion,^{1,2} clustering of transcription factor-bound elements into complex “hubs” or “factories”^{10,32,61,62}, or compartmentalization.^{11,57,63} Although the specificity of CTCF-dependent loops in mammalian cells is explained by a tracking mechanism, the specificity of meta-loop interactions invokes a distinct mechanism. CTCF-dependent meta-loops are unlikely to be extruded due to their large (up to 16 Mb) size and spanning of hundreds of TAD boundaries in between. Furthermore, in contrast to meta-domains, the compartmentalization of heterochromatic OR clusters relies not only on the binding of a common set of transcription factors to local OR enhancer clusters but also primarily on heterochromatin-driven compartmentalization of OR clusters.¹¹

In conclusion, the striking specificity of meta-loop interactions is arguably their most intriguing property. The mechanisms by which GAF or CTCF enable specific pairwise interactions, despite binding to over a thousand loci,^{41,64} remain unclear. Meta-loops provide a powerful and relevant paradigm to explore the emergence of specific long-range regulatory interactions in genomes and their role in establishing tissue-specific gene activity.

Limitations of the study

Why meta-loops are enriched in the CNS remains unresolved. Meta-loops may be most prominent in neurons because neurons are post-mitotic. However, our data suggest that meta-loops are functionally significant in the CNS. It remains unclear whether meta-loops represent a mere adaptation or an evolutionary advantage. Meta-loops may compensate for chance breakpoints (illustrated in Figure 2B) that separate CNS genes from their regulatory elements. Alternatively, meta-loops may prevent premature regulation of genes by distal regulatory elements until 3D genome organization in the CNS matures (Figure 3A) and stabilizes meta-loops. Differentiating between these models requires identifying putative distal regulatory elements and positioning them close to target genes to bypass long-range regulation. Another possibility is that meta-loops evolved to generate novelty in the brain. Determining whether meta-loops confer advantages for regulating specific CNS genes in a given species will require identifying the relevant neurons where gene expression depends on meta-loops and understanding how this regulation confers species-specific traits, ideally through studies conducted in natural habitats.

STAR★METHODS

Detailed methods are provided in the online version of this paper and include the following:

- KEY RESOURCES TABLE
- RESOURCE AVAILABILITY
 - Lead contact
 - Materials availability
 - Data and code availability
- EXPERIMENTAL MODEL AND STUDY PARTICIPANT DETAILS
 - Drosophila
- METHOD DETAILS
 - Micro-C
 - Micro-C analysis
 - FACS of embryonic neurons, glia, neuroblasts for Hi-C
 - Hi-C
 - Hi-C analysis
 - Meta-loop calling
 - Loop anchor classification
 - Differential analysis of Micro-C or Hi-C interactions
 - Analysis of three-way interactions between meta-loop anchors
 - Loop strength measurement
 - GO term enrichment analysis
 - RNA-FISH
 - DNA-FISH
 - RNA-DNA-FISH
 - HCR-RNA-FISH
 - RT-qPCR on larval CNSs, adult heads or whole-bodied flies
 - CRISPR/Cas9-mediated intergenic anchor deletions
 - *nolo* CRISPR/Cas9-mediated knock-outs and RNAi
 - *Drosophila* viability tests
 - Analysis of neuromuscular junctions
 - Transgenic enhancer assays
 - scATAC-seq on third instar larval central nervous systems
 - scRNA-seq on third instar larval central nervous systems
 - scATAC-seq analysis
 - scRNA-seq analysis
 - Comparative analysis of meta-loops in *D. mel.* and *D. vir.* adult central nervous systems
 - Reuse of published datasets
- QUANTIFICATION AND STATISTICAL ANALYSIS

SUPPLEMENTAL INFORMATION

Supplemental information can be found online at <https://doi.org/10.1016/j.cell.2023.07.008>.

ACKNOWLEDGMENTS

We thank David Garfield for helpful discussions and Victor Rossier for his gene family visualization interface. H.M. was enrolled in the University of Paris Cité European Master Program in Genetics. R.C.S. received funding from the Marie Skłodowska-Curie grant agreement no. 945363. This work was supported by the Polish National Agency for Academic Exchange (Polish Returns 2019 to A.J.), National Institutes of Health grant R35 GM118147 and U01 DK127429 (to M.S.L.), the Swiss National Science Foundation grant no. 184715 (to M.C.G.), the Pierre Mercier Science Foundation (to M.C.G.), and the University of Lausanne (to M.C.G.).

AUTHOR CONTRIBUTIONS

Conceptualization, A.J., M.S.L., and M.C.G.; methodology, G.M., J.D., S.R., A.J., and M.C.G.; investigation, G.M., X.L., M.M., R.C.S., H.M., D.R., J.K., and M.C.G.; formal analysis, J.D., X.L., M.L., P.R., C.I., N.G., and A.J.; writing, N.G., A.J., M.S.L., and M.C.G.; supervision, N.G., B.D.M., A.J., M.S.L., and M.C.G.; funding acquisition, A.J., M.S.L., and M.C.G.

DECLARATION OF INTERESTS

S.R. developed MUSE technology marketed by arcoris bio AG, has shares, and sits on the board.

Received: October 16, 2022

Revised: March 31, 2023

Accepted: July 6, 2023

Published: August 2, 2023

REFERENCES

- Rao, S.S.P., Huang, S.-C., Hilaire, B.G.S., Engreitz, J.M., Perez, E.M., Kieffer-Kwon, K.-R., Sanborn, A.L., Johnstone, S.E., Bascom, G.D., Bochkov, I.D., et al. (2017). Cohesin loss eliminates all loop domains. *Cell* 171, 305–320.e24. <https://doi.org/10.1016/j.cell.2017.09.026>.
- Nora, E.P., Goloborodko, A., Valton, A.-L., Gibcus, J.H., Uebersohn, A., Abdennur, N., Dekker, J., Mirny, L.A., and Bruneau, B.G. (2017). Targeted degradation of CTCF decouples local insulation of chromosome domains from genomic compartmentalization. *Cell* 169, 930–944.e22. <https://doi.org/10.1016/j.cell.2017.05.004>.
- Rowley, M.J., Nichols, M.H., Lyu, X., Ando-Kuri, M., Rivera, I.S.M., Hermetz, K., Wang, P., Ruan, Y., and Corces, V.G. (2017). Evolutionarily conserved principles predict 3D chromatin organization. *Mol. Cell* 67, 837–852.e7. <https://doi.org/10.1016/j.molcel.2017.07.022>.
- Paulsen, J., Ali, T.M.L., Nekrasov, M., Delbarre, E., Baudement, M.-O., Kurscheid, S., Tremethick, D., and Collas, P. (2019). Long-range interactions between topologically associating domains shape the four-dimensional genome during differentiation. *Nat. Genet.* 51, 835–843. <https://doi.org/10.1038/s41588-019-0392-0>.
- Szabo, Q., Jost, D., Chang, J.-M., Cattoni, D.I., Papadopoulos, G.L., Bonev, B., Sexton, T., Gurgo, J., Jacquier, C., Nöhlmann, M., et al. (2018). TADs are 3D structural units of higher-order chromosome organization in *Drosophila*. *Sci. Adv.* 4, eaar8082. <https://doi.org/10.1126/sciadv.aar8082>.
- Beagrie, R.A., Scialdone, A., Schueler, M., Kraemer, D.C.A., Chotalia, M., Xie, S.Q., Barbieri, M., de Santiago, I., Lavitas, L.-M., Branco, M.R., et al. (2017). Complex multi-enhancer contacts captured by genome architecture mapping. *Nature* 543, 519–524. <https://doi.org/10.1038/nature21411>.
- Lieberman-Aiden, E., van Berkum, N.L., Williams, L., Imakaev, M., Ragozcy, T., Telling, A., Amit, I., Lajoie, B.R., Sabo, P.J., Dorschner, M.O., et al. (2009). Comprehensive mapping of long-range interactions reveals folding principles of the human genome. *Science* 326, 289–293. <https://doi.org/10.1126/science.1181369>.
- Rao, S.S.P., Huntley, M.H., Durand, N.C., Stamenova, E.K., Bochkov, I.D., Robinson, J.T., Sanborn, A.L., Machol, I., Omer, A.D., Lander, E.S., et al. (2014). A 3D map of the human genome at kilobase resolution reveals principles of chromatin looping. *Cell* 159, 1665–1680. <https://doi.org/10.1016/j.cell.2014.11.021>.
- Zenk, F., Zhan, Y., Kos, P., Löser, E., Atinbayeva, N., Schächtle, M., Tiana, G., Giorgetti, L., and Iovino, N. (2021). HP1 drives de novo 3D genome reorganization in early *Drosophila* embryos. *Nature* 593, 289–293. <https://doi.org/10.1038/s41586-021-03460-z>.
- Bonev, B., Cohen, N.M., Szabo, Q., Fritsch, L., Papadopoulos, G.L., Lubling, Y., Xu, X., Lv, X., Hugnot, J.-P., Tanay, A., et al. (2017). Multiscale 3D genome rewiring during mouse neural development. *Cell* 171, 557–572.e24. <https://doi.org/10.1016/j.cell.2017.09.043>.
- Monahan, K., Horta, A., and Lomvardas, S. (2019). LHX2- and LDB1-mediated trans interactions regulate olfactory receptor choice. *Nature* 565, 448–453. <https://doi.org/10.1038/s41586-018-0845-0>.
- Hug, C.B., Grimaldi, A.G., Kruse, K., and Vaquerizas, J.M. (2017). Chromatin architecture emerges during zygotic genome activation independent of transcription. *Cell* 169, 216–228.e19. <https://doi.org/10.1016/j.cell.2017.03.024>.
- Zhang, S., Übelmesser, N., Barbieri, M., and Papanonis, A. (2023). Enhancer-promoter contact formation requires RNAPII and antagonizes loop extrusion. *Nat. Genet.* 55, 832–840. <https://doi.org/10.1038/s41588-023-01364-4>.
- Chen, H., Levo, M., Barinov, L., Fujioka, M., Jaynes, J.B., and Gregor, T. (2018). Dynamic interplay between enhancer-promoter topology and gene activity. *Nat. Genet.* 50, 1296–1303. <https://doi.org/10.1038/s41588-018-0175-z>.
- Kane, L., Williamson, I., Flyamer, I.M., Kumar, Y., Hill, R.E., Lettice, L.A., and Bickmore, W.A. (2022). Cohesin is required for long-range enhancer action at the *Shh* locus. *Nat. Struct. Mol. Biol.* 29, 891–897. <https://doi.org/10.1038/s41594-022-00821-8>.
- Fulco, C.P., Nasser, J., Jones, T.R., Munson, G., Bergman, D.T., Subramanian, V., Grossman, S.R., Anyoha, R., Doughty, B.R., Patwardhan, T.A., et al. (2019). Activity-by-contact model of enhancer-promoter regulation from thousands of CRISPR perturbations. *Nat. Genet.* 51, 1664–1669. <https://doi.org/10.1038/s41588-019-0538-0>.
- Ghavi-Helm, Y., Klein, F.A., Pakozdi, T., Ciglar, L., Noordermeer, D., Huber, W., and Furlong, E.E.M. (2014). Enhancer loops appear stable during development and are associated with paused polymerase. *Nature* 512, 96–100. <https://doi.org/10.1038/nature13417>.
- Symmons, O., Uslu, V.V., Tsujimura, T., Ruf, S., Nassari, S., Schwarzer, W., Ettwiller, L., and Spitz, F. (2014). Functional and topological characteristics of mammalian regulatory domains. *Genome Res.* 24, 390–400. <https://doi.org/10.1101/gr.163519.113>.
- Symmons, O., Pan, L., Remeseiro, S., Aktas, T., Klein, F., Huber, W., and Spitz, F. (2016). The *shh* topological domain facilitates the action of remote enhancers by reducing the effects of genomic distances. *Dev. Cell* 39, 529–543. <https://doi.org/10.1016/j.devcel.2016.10.015>.
- Kaushal, A., Dorier, J., Wang, B., Mohana, G., Taschner, M., Cousin, P., Waridel, P., Iseli, C., Semenova, A., Restrepo, S., et al. (2022). Essential role of Cp190 in physical and regulatory boundary formation. *Sci. Adv.* 8, eabl8834. <https://doi.org/10.1126/sciadv.abl8834>.
- Zuin, J., Roth, G., Zhan, Y., Cramard, J., Redolfi, J., Piskadlo, E., Mach, P., Kryzhanovska, M., Tihanyi, G., Kohler, H., et al. (2022). Nonlinear control of transcription through enhancer-promoter interactions. *Nature* 604, 571–577. <https://doi.org/10.1038/s41586-022-04570-y>.
- Lupiáñez, D.G., Kraft, K., Heinrich, V., Krawitz, P., Brancati, F., Klopocki, E., Horn, D., Kayserili, H., Opitz, J.M., Laxova, R., et al. (2015). Disruptions of topological chromatin domains cause pathogenic rewiring of gene-enhancer interactions. *Cell* 161, 1012–1025. <https://doi.org/10.1016/j.cell.2015.04.004>.
- Pachano, T., Sánchez-Gaya, V., Ealo, T., Mariner-Faulí, M., Bleckwehl, T., Asenjo, H.G., Respuela, P., Cruz-Molina, S., Muñoz-San Martín, M.M.-S., Haro, E., et al. (2021). Orphan CpG islands amplify poised enhancer regulatory activity and determine target gene responsiveness. *Nat. Genet.* 53, 1036–1049. <https://doi.org/10.1038/s41588-021-00888-x>.
- Hafner, A., Park, M., Berger, S.E., Murphy, S.E., Nora, E.P., and Boettiger, A.N. (2023). Loop stacking organizes genome folding from TADs to chromosomes. *Mol. Cell* 83, 1377–1392.e6. <https://doi.org/10.1016/j.molcel.2023.04.008>.
- Batut, P.J., Bing, X.Y., Sisco, Z., Raimundo, J., Levo, M., and Levine, M.S. (2022). Genome organization controls transcriptional dynamics during development. *Science* 375, 566–570. <https://doi.org/10.1126/science.abi7178>.

26. Levo, M., Raimundo, J., Bing, X.Y., Sisco, Z., Batut, P.J., Ryabichko, S., Gregor, T., and Levine, M.S. (2022). Transcriptional coupling of distant regulatory genes in living embryos. *Nature* 605, 754–760. <https://doi.org/10.1038/s41586-022-04680-7>.
27. Kubo, N., Ishii, H., Xiong, X., Bianco, S., Meitinger, F., Hu, R., Hocker, J.D., Conte, M., Gorkin, D., Yu, M., et al. (2021). Promoter-proximal CTCF binding promotes distal enhancer-dependent gene activation. *Nat. Struct. Mol. Biol.* 28, 152–161. <https://doi.org/10.1038/s41594-020-00539-5>.
28. Rinzema, N.J., Sofiadis, K., Tjalsma, S.J.D., Versteegen, M.J.A.M., Oz, Y., Valdes-Quezada, C., Felder, A.-K., Filipovska, T., van der Elst, S., de Andrade Dos Ramos, Z., et al. (2022). Building regulatory landscapes reveals that an enhancer can recruit cohesin to create contact domains, engage CTCF sites and activate distant genes. *Nat. Struct. Mol. Biol.* 29, 563–574. <https://doi.org/10.1038/s41594-022-00787-7>.
29. Dixon, J.R., Jung, I., Selvaraj, S., Shen, Y., Antosiewicz-Bourget, J.E., Lee, A.Y., Ye, Z., Kim, A., Rajagopal, N., Xie, W., et al. (2015). Chromatin architecture reorganization during stem cell differentiation. *Nature* 518, 331–336. <https://doi.org/10.1038/nature14222>.
30. Winick-Ng, W., Kukalev, A., Harabula, I., Zea-Redondo, L., Szabó, D., Meijer, M., Serebreni, L., Zhang, Y., Bianco, S., Chiariello, A.M., et al. (2021). Cell-type specialization is encoded by specific chromatin topologies. *Nature* 599, 684–691. <https://doi.org/10.1038/s41586-021-04081-2>.
31. Andrey, G., Montavon, T., Mascrez, B., Gonzalez, F., Noordermeer, D., Leleu, M., Trono, D., Spitz, F., and Duboule, D. (2013). A switch between topological domains underlies HoxD genes collinearity in mouse limbs. *Science* 340, 1234167. <https://doi.org/10.1126/science.1234167>.
32. Dotson, G.A., Chen, C., Lindsly, S., Cicalo, A., Dilworth, S., Ryan, C., Jeyarajan, S., Meixner, W., Stansbury, C., Pickard, J., et al. (2022). Deciphering multi-way interactions in the human genome. *Nat. Commun.* 13, 5498. <https://doi.org/10.1038/s41467-022-32980-z>.
33. Allahyar, A., Vermeulen, C., Bouwman, B.A.M., Krijger, P.H.L., Versteegen, M.J.A.M., Geeven, G., van Kranenburg, M., Pieterse, M., Straver, R., Haarhuis, J.H.I., et al. (2018). Enhancer hubs and loop collisions identified from single-allele topologies. *Nat. Genet.* 50, 1151–1160. <https://doi.org/10.1038/s41588-018-0161-5>.
34. Mateo, L.J., Murphy, S.E., Hafner, A., Cinquini, I.S., Walker, C.A., and Boettiger, A.N. (2019). Visualizing DNA folding and RNA in embryos at single-cell resolution. *Nature* 567, 1–54. <https://doi.org/10.1038/s41586-019-1035-4>.
35. Gizzi, A.M.C., Cattoni, D.I., Fiche, J.-B., Espinola, S.M., Gurgo, J., Messina, O., Houbroun, C., Ogiyama, Y., Papadopoulos, G.L., Cavalli, G., et al. (2019). Microscopy-based chromosome conformation capture enables simultaneous visualization of genome organization and transcription in intact organisms. *Mol. Cell* 74, 212–222.e5. <https://doi.org/10.1016/j.molcel.2019.01.011>.
36. Ing-Simmons, E., Vaid, R., Bing, X.Y., Levine, M., Mannervik, M., and Vazquez, J.M. (2021). Independence of chromatin conformation and gene regulation during *Drosophila* dorsoventral patterning. *Nat. Genet.* 53, 487–499. <https://doi.org/10.1038/s41588-021-00799-x>.
37. Espinola, S.M., Götz, M., Bellec, M., Messina, O., Fiche, J.-B., Houbroun, C., Dejean, M., Reim, I., Gizzi, A.M.C., Lagha, M., et al. (2021). Cis-regulatory chromatin loops arise before TADs and gene activation, and are independent of cell fate during early *Drosophila* development. *Nat. Genet.* 53, 477–486. <https://doi.org/10.1038/s41588-021-00816-z>.
38. Stadler, M.R., Haines, J.E., and Eisen, M.B. (2017). Convergence of topological domain boundaries, insulators, and polytene interbands revealed by high-resolution mapping of chromatin contacts in the early *Drosophila* melanogaster embryo. *eLife* 6, e29550. <https://doi.org/10.7554/eLife.29550>.
39. Hsieh, T.-H.S., Cattoglio, C., Slobodyanyuk, E., Hansen, A.S., Rando, O.J., Tjian, R., and Darzacq, X. (2020). Resolving the 3D landscape of transcription-linked mammalian chromatin folding. *Mol. Cell* 78, 539–553.e8. <https://doi.org/10.1016/j.molcel.2020.03.002>.
40. Reddington, J.P., Garfield, D.A., Sigalova, O.M., Calviello, A.K., Marco-Ferreres, R., Girardot, C., Viales, R.R., Degner, J.F., Ohler, U., and Furlong, E.E.M. (2020). Lineage-resolved enhancer and promoter usage during a time course of embryogenesis. *Dev. Cell* 55, 648–664.e9. <https://doi.org/10.1016/j.devcel.2020.10.009>.
41. Kaushal, A., Mohana, G., Dorier, J., Özdemir, I., Omer, A., Cousin, P., Semenova, A., Taschner, M., Dergai, O., Marzetta, F., et al. (2021). CTCF loss has limited effects on global genome architecture in *Drosophila* despite critical regulatory functions. *Nat. Commun.* 12, 1011. <https://doi.org/10.1038/s41467-021-21366-2>.
42. Krause, S.A., Overend, G., Dow, J.A.T., and Leader, D.P. (2022). FlyAtlas 2 in 2022: enhancements to the *Drosophila melanogaster* expression atlas. *Nucleic Acids Res.* 50, D1010–D1015. <https://doi.org/10.1093/nar/gkab971>.
43. Eagen, K.P., Aiden, E.L., and Kornberg, R.D. (2017). Polycomb-mediated chromatin loops revealed by a subkilobase-resolution chromatin interaction map. *Proc. Natl. Acad. Sci. USA* 114, 8764–8769. <https://doi.org/10.1073/pnas.1701291114>.
44. Özel, M.N., Simon, F., Jafari, S., Holguera, I., Chen, Y.-C., Benhra, N., El-Danaf, R.N., Kapuralin, K., Malin, J.A., Konstantinides, N., et al. (2021). Neuronal diversity and convergence in a visual system developmental atlas. *Nature* 589, 88–95. <https://doi.org/10.1038/s41586-020-2879-3>.
45. Stark, A., Lin, M.F., Kheradpour, P., Pedersen, J.S., Parts, L., Carlson, J.W., Crosby, M.A., Rasmussen, M.D., Roy, S., Deoras, A.N., et al. (2007). Discovery of functional elements in 12 *Drosophila* genomes using evolutionary signatures. *Nature* 450, 219–232. <https://doi.org/10.1038/nature06340>.
46. Janssens, J., Aibar, S., Taskiran, I.I., Ismail, J.N., Gomez, A.E., Aughey, G., Spanier, K.I., De Rop, F.V.D., González-Blas, C.B., Dionne, M., et al. (2022). Decoding gene regulation in the fly brain. *Nature* 607, 630–636. <https://doi.org/10.1038/s41586-021-04262-z>.
47. Liu, J., Viales, R.R., Khoueiry, P., Reddington, J.P., Girardot, C., Furlong, E.E.M., and Robinson-Rechavi, M. (2021). The hourglass model of evolutionary conservation during embryogenesis extends to developmental enhancers with signatures of positive selection. *Genome Res.* 31, 1573–1581. <https://doi.org/10.1101/gr.275212.121>.
48. Özkan, E., Carrillo, R.A., Eastman, C.L., Weiszmann, R., Waghray, D., Johnson, K.G., Zinn, K., Celniker, S.E., and Garcia, K.C. (2013). An extracellular interactome of immunoglobulin and LRR proteins reveals receptor-ligand networks. *Cell* 154, 228–239. <https://doi.org/10.1016/j.cell.2013.06.006>.
49. *Drosophila* 12 Genomes Consortium, Clark, A.G., Eisen, M.B., Smith, D.R., Bergman, C.M., Oliver, B., Markow, T.A., Kaufman, T.C., Kellis, M., Gelbart, W., et al. (2007). Evolution of genes and genomes on the *Drosophila* phylogeny. *Nature* 450, 203–218. <https://doi.org/10.1038/nature06341>.
50. Meyer, S., Schmidt, I., and Klämbt, C. (2014). Glia ECM interactions are required to shape the *Drosophila* nervous system. *Mech. Dev.* 133, 105–116. <https://doi.org/10.1016/j.mod.2014.05.003>.
51. Li, X., Tang, X., Bing, X., Catalano, C., Li, T., Dolsten, G., Wu, C., and Levine, M. (2023). GAGA-associated factor fosters loop formation in the *Drosophila* genome. *Mol. Cell* 83, 1519–1526.e4. <https://doi.org/10.1016/j.molcel.2023.03.011>.
52. Tang, X., Li, T., Liu, S., Wisniewski, J., Zheng, Q., Rong, Y., Lavis, L.D., and Wu, C. (2022). Kinetic principles underlying pioneer function of GAGA transcription factor in live cells. *Nat. Struct. Mol. Biol.* 29, 665–676. <https://doi.org/10.1038/s41594-022-00800-z>.
53. Tsai, S.-Y., Chang, Y.-L., Swamy, K.B.S., Chiang, R.-L., and Huang, D.-H. (2016). GAGA factor, a positive regulator of global gene expression, modulates transcriptional pausing and organization of upstream nucleosomes. *Epigenetics Chromatin* 9, 32. <https://doi.org/10.1186/s13072-016-0082-4>.

54. Sexton, T., Yaffe, E., Kenigsberg, E., Bantignies, F., Leblanc, B., Hoichman, M., Parrinello, H., Tanay, A., and Cavalli, G. (2012). Three-dimensional folding and functional organization principles of the *Drosophila* genome. *Cell* *148*, 458–472. <https://doi.org/10.1016/j.cell.2012.01.010>.
55. Ghavi-Helm, Y., Jankowski, A., Meiers, S., Viales, R.R., Korb, J.O., and Furlong, E.E.M. (2019). Highly rearranged chromosomes reveal uncoupling between genome topology and gene expression. *Nat. Genet.* *51*, 1272–1282. <https://doi.org/10.1038/s41588-019-0462-3>.
56. Song, M., Pebworth, M.-P., Yang, X., Abnoui, A., Fan, C., Wen, J., Rosen, J.D., Choudhary, M.N.K., Cui, X., Jones, I.R., et al. (2020). Cell-type-specific 3D epigenomes in the developing human cortex. *Nature* *587*, 644–649. <https://doi.org/10.1038/s41586-020-2825-4>.
57. Clowney, E.J., LeGros, M.A., Mosley, C.P., Clowney, F.G., Markenskoff-Papadimitriou, E.C., Myllys, M., Barnea, G., Larabell, C.A., and Lomvardas, S. (2012). Nuclear aggregation of olfactory receptor genes governs their monogenic expression. *Cell* *151*, 724–737. <https://doi.org/10.1016/j.cell.2012.09.043>.
58. Long, H.K., Osterwalder, M., Welsh, I.C., Hansen, K., Davies, J.O.J., Liu, Y.E., Koska, M., Adams, A.T., Aho, R., Arora, N., et al. (2020). Loss of extreme long-range enhancers in human neural crest drives a craniofacial disorder. *Cell Stem Cell* *27*, 765–783.e14. <https://doi.org/10.1016/j.stem.2020.09.001>.
59. Cusanovich, D.A., Reddington, J.P., Garfield, D.A., Daza, R.M., Aghamirzaie, D., Marco-Ferreres, R., Pliner, H.A., Christiansen, L., Qiu, X., Steemers, F.J., et al. (2018). The cis-regulatory dynamics of embryonic development at single-cell resolution. *Nature* *555*, 538–542. <https://doi.org/10.1038/nature25981>.
60. Fujioka, M., Mistry, H., Schedl, P., and Jaynes, J.B. (2016). Determinants of Chromosome Architecture: insulator Pairing in cis and in trans. *PLoS Genet.* *12*, e1005889. <https://doi.org/10.1371/journal.pgen.1005889>.
61. Tsai, A., Muthusamy, A.K., Alves, M.R., Lavis, L.D., Singer, R.H., Stern, D.L., and Crocker, J. (2017). Nuclear microenvironments modulate transcription from low-affinity enhancers. *eLife* *6*, e1006441. <https://doi.org/10.7554/eLife.28975>.
62. Cho, W.-K., Spille, J.-H., Hecht, M., Lee, C., Li, C., Grube, V., and Cisse, I.I. (2018). Mediator and RNA polymerase II clusters associate in transcription-dependent condensates. *Science* *361*, 412–415. <https://doi.org/10.1126/science.aar4199>.
63. Rosencrance, C.D., Ammouri, H.N., Yu, Q., Ge, T., Rendleman, E.J., Marshall, S.A., and Eagen, K.P. (2020). Chromatin hyperacetylation impacts chromosome folding by forming a nuclear subcompartment. *Mol. Cell* *78*, 112–126.e12. <https://doi.org/10.1016/j.molcel.2020.03.018>.
64. Gaskill, M.M., Gibson, T.J., Larson, E.D., and Harrison, M.M. (2021). GAF is essential for zygotic genome activation and chromatin accessibility in the early *Drosophila* embryo. *eLife* *10*, e66668. <https://doi.org/10.7554/eLife.66668>.
65. Banerjee, S., Vernon, S., Jiao, W., Choi, B.J., Ruchti, E., Asadzadeh, J., Burri, O., Stowers, R.S., and McCabe, B.D. (2021). Miniature neurotransmission is required to maintain *Drosophila* synaptic structures during ageing. *Nat. Commun.* *12*, 4399. <https://doi.org/10.1038/s41467-021-24490-1>.
66. Kerpedjiev, P., Abdennur, N., Lekschas, F., McCallum, C., Dinkla, K., Strobel, H., Luber, J.M., Ouellette, S.B., Azhir, A., Kumar, N., et al. (2018). Hi-Glass: web-based visual exploration and analysis of genome interaction maps. *Genome Biol.* *19*, 125. <https://doi.org/10.1186/s13059-018-1486-1>.
67. Abdennur, N., and Mirny, L.A. (2020). Cooler: scalable storage for Hi-C data and other genomically labeled arrays. *Bioinformatics* *36*, 311–316. <https://doi.org/10.1093/bioinformatics/btz540>.
68. Pau, G., Fuchs, F., Sklyar, O., Boutros, M., and Huber, W. (2010). EB-Image—an R package for image processing with applications to cellular phenotypes. *Bioinformatics* *26*, 979–981. <https://doi.org/10.1093/bioinformatics/btq046>.
69. Hinrichs, A.S., Karolchik, D., Baertsch, R., Barber, G.P., Bejerano, G., Clawson, H., Diekhans, M., Furey, T.S., Harte, R.A., Hsu, F., et al. (2006). The UCSC Genome Browser Database: update 2006. *Nucleic Acids Res.* *34*, D590–D598. <https://doi.org/10.1093/nar/gkj144>.
70. Quinlan, A.R., and Hall, I.M. (2010). BEDTools: a flexible suite of utilities for comparing genomic features. *Bioinformatics* *26*, 841–842. <https://doi.org/10.1093/bioinformatics/btq033>.
71. Open2C, Abdennur, N., Fudenberg, G., Flyamer, I.M., Galitsyna, A.A., Goloborodko, A., Imakaev, M., and Venev, S.V. (2023). Pairtools: from sequencing data to chromosome contacts. <https://doi.org/10.1101/2023.02.13.528389>.
72. Love, M.I., Huber, W., and Anders, S. (2014). Moderated estimation of fold change and dispersion for RNA-seq data with DESeq2. *Genome Biol.* *15*, 550. <https://doi.org/10.1186/s13059-014-0550-8>.
73. Kuhn, R.M., Haussler, D., and Kent, W.J. (2013). The UCSC genome browser and associated tools. *Brief. Bioinform.* *14*, 144–161. <https://doi.org/10.1093/bib/bbs038>.
74. Tan, G., Polychronopoulos, D., and Lenhard, B. (2019). CNER: A toolkit for exploring extreme noncoding conservation. *PLOS Comput. Biol.* *15*, e1006940. <https://doi.org/10.1371/journal.pcbi.1006940>.
75. Harris, R.S. (2007). Improved pairwise alignment of genomic DNA. Ph.D. Thesis (The Pennsylvania State University).
76. Schindelin, J., Arganda-Carreras, I., Frise, E., Kaynig, V., Longair, M., Pietzsch, T., Preibisch, S., Rueden, C., Saalfeld, S., Schmid, B., et al. (2012). Fiji: an open-source platform for biological-image analysis. *Nat. Methods* *9*, 676–682. <https://doi.org/10.1038/nmeth.2019>.
77. Stuart, T., Butler, A., Hoffman, P., Hafemeister, C., Papalexi, E., Mauck, W.M., Hao, Y., Stoeckius, M., Smibert, P., and Satija, R. (2019). Comprehensive integration of single-cell data. *Cell* *177*, 1888–1902.e21. <https://doi.org/10.1016/j.cell.2019.05.031>.
78. Stuart, T., Srivastava, A., Madad, S., Lareau, C.A., and Satija, R. (2021). Single-cell chromatin state analysis with Signac. *Nat. Methods* *18*, 1333–1341. <https://doi.org/10.1038/s41592-021-01282-5>.
79. Yu, G., Wang, L.-G., Han, Y., and He, Q.-Y. (2012). clusterProfiler: an R package for comparing biological themes among gene clusters. *Omics J. Integr. Biol.* *16*, 284–287. <https://doi.org/10.1089/omi.2011.0118>.
80. Renschler, G., Richard, G., Valsecchi, C.I.K., Toscano, S., Arrigoni, L., Ramirez, F., and Akhtar, A. (2019). Hi-C guided assemblies reveal conserved regulatory topologies on X and autosomes despite extensive genome shuffling. *Genes Dev.* *33*, 1591–1612. <https://doi.org/10.1101/gad.328971.119>.
81. Li, H. (2013). Aligning sequence reads, clone sequences and assembly contigs with BWA-MEM. <https://doi.org/10.48550/arxiv.1303.3997>.
82. Bintu, B., Mateo, L.J., Su, J.-H., Sinnott-Armstrong, N.A., Parker, M., Kinrot, S., Yamaya, K., Boettiger, A.N., and Zhuang, X. (2018). Super-resolution chromatin tracing reveals domains and cooperative interactions in single cells. *Science* *362*, eaau1783. <https://doi.org/10.1126/science.aau1783>.
83. Port, F., Chen, H.-M., Lee, T., and Bullock, S.L. (2014). Optimized CRISPR/Cas tools for efficient germline and somatic genome engineering in *Drosophila*. *Proc. Natl. Acad. Sci. USA* *111*, E2967–E2976. <https://doi.org/10.1073/pnas.1405500111>.
84. Bischof, J., Maeda, R.K., Hediger, M., Karch, F., and Basler, K. (2007). Bischof_Basler2007P.pdf. *Proc. Natl. Acad. Sci. USA* *104*, 3312–3317. <https://doi.org/10.1073/pnas.0611511104>.
85. Venken, K.J.T., He, Y., Hoskins, R.A., and Bellen, H.J. (2006). P[acman]: a BAC transgenic platform for targeted insertion of large DNA fragments in *D. melanogaster*. *Science* *314*, 1747–1751. <https://doi.org/10.1126/science.1134426>.

86. Kent, W.J. (2002). BLAT—the BLAST-like alignment tool. *Genome Res.* 12, 656–664. <https://doi.org/10.1101/gr.229202>.
87. Zdobnov, E.M., Kuznetsov, D., Tegenfeldt, F., Manni, M., Berkeley, M., and Kriventseva, E.V. (2020). OrthoDB in 2020: evolutionary and functional annotations of orthologs. *Nucleic Acids Res.* 49, gkaa1009. <https://doi.org/10.1093/nar/gkaa1009>.
88. Li, H., and Durbin, R. (2009). Fast and accurate short read alignment with Burrows–Wheeler transform. *Bioinformatics* 25, 1754–1760. <https://doi.org/10.1093/bioinformatics/btp324>.
89. Loubiere, V., Papadopoulos, G.L., Szabo, Q., Martinez, A.-M., and Cavalli, G. (2020). Widespread activation of developmental gene expression characterized by PRC1-dependent chromatin looping. *Sci. Adv.* 6, eaax4001. <https://doi.org/10.1126/sciadv.aax4001>.

STAR★METHODS

KEY RESOURCES TABLE

REAGENT or RESOURCE	SOURCE	IDENTIFIER
Antibodies		
sheep anti-Dig peroxidase	Roche	11207733910; RRID: AB_514500
mouse monoclonal anti-Elav	Developmental Studies Hybridoma Bank	9F8A9; RRID: AB_528217
rat monoclonal anti-Elav	Developmental Studies Hybridoma Bank	7E8A10; RRID: AB_528218
mouse monoclonal anti-Repo	Developmental Studies Hybridoma Bank	8D12; RRID: AB_528448
rat anti-Wor	Abcam	ab196362
mouse monoclonal anti-vGlut clone 10D6G	Banerjee et al. ⁶⁵	10D6G
Alexa 647 anti-rat IgG	Thermo Scientific	A21247; RRID: AB_141778
Alexa 647 goat anti-HRP	Jackson ImmunoResearch	123-605-021; RRID: AB_2338967
Alexa 555 anti-mouse IgG	Thermo Scientific	A-21422; RRID: AB_2535844
Bacterial and virus strains		
DH5alpha E. coli	New England Biolabs	C2987H
Chemicals, peptides, and recombinant proteins		
16% formaldehyde	Thermo Scientific	20593
DSG (disuccinimidyl glutarate)	Thermo Scientific	20593
EGS (ethylene glycol bis(succinimidyl succinate))	Thermo Scientific	21565
Micrococcal nuclease	New England Biolabs	M0247S
DNA polymerase I, large (Klenow) fragment	New England Biolabs	M0210
T4 polynucleotide kinase	New England Biolabs	M0201
T4 DNA ligase	New England Biolabs	M0202
Exonuclease III	New England Biolabs	M0206
Biotin-14-dATP	Jena Bioscience	NU-835-BIO14
Biotin-11-dCTP	Jena Bioscience	NU-809-BIOX
Collagenase I	Sigma	C2674
Papain	Sigma	P4762
RNase inhibitor	Sigma	3335399001
MseI	New England Biolabs	R0525S
Csp6I	Thermo Scientific	ER0211
Hoechst 33342	Sigma-Aldrich	23491-52-3
UltraPure™ SSC, 20X	Thermo Fisher Scientific	15557044
ProLong Gold Antifade Mountant	Thermo Fisher Scientific	P36934
TRIzol Reagents	Thermo Fisher Scientific	15596026
Phenol:Chloroform:Isoamylalcohol (PCI, 25:24:1)	Thermo Scientific	15593031
T7 RNA polymerase	Roche	10881767001
Dig-UTP labeling mix	Roche	11277073910
DNase I recombinant, RNase-free	Roche	04716728001
aminoallyl-dUTP-XX-ATTO-488	Jena Bioscience	NU-803-XX-488-S
aminoallyl-dUTP-ATTO-550	Jena Bioscience	NU-803-550-S
Critical commercial assays		
Zymoclean Gel DNA Recovery Kit	Zymo Research	D4007
TSA Plus Cyanine 3/Fluorescein System	Perkin Elmer	NEL753001KT

(Continued on next page)

Continued

REAGENT or RESOURCE	SOURCE	IDENTIFIER
HCR buffer set	Molecular Instruments	www.molecularinstruments.com
HCR B1 488 amplifier	Molecular Instruments	www.molecularinstruments.com
HCR B2 546 amplifier	Molecular Instruments	www.molecularinstruments.com
Moxi V	Witec	MXV102
10x Genomics Chromium single cell ATAC reagent kits solution v1.0	10x Genomics	CG000168
10x Genomics Chromium Next GEM sc 3' reagent kits v3.1 dual index	10x Genomics	CG000315
SPRI Select beads	Beckman Coulter	B23319
Ampure XP beads	Beckman Coulter	A63880
NEBNext Ultra II DNA Library Prep kit for Illumina	New England Biolabs	E7645S
Dynabeads MyOne Streptavidin T1 beads	Invitrogen	65601
KAPA HiFi HotStart Ready Mix	Roche	KK2501
Nick-translation kit	Abbott Molecular	07J100-001
SuperScript IV	Invitrogen	18091050
GoScript	Promega	A2801
SYBR green	Invitrogen	4367659
GoTaq	Promega	A600A

Deposited data

Raw and processed data (Hi-C, scATAC-seq, scRNA-seq)	This paper	GEO: GSE214707
Raw and processed data (Micro-C)	This paper	GEO: GSE228095

Experimental models: Organisms/strains

<i>D. melanogaster</i> : <i>nolo</i> intergenic anchor deletion: <i>nolo</i> ^{ΔA23}	This paper	N/A
<i>D. melanogaster</i> : <i>beat-IV</i> intergenic anchor deletion: <i>beat-IV</i> ^{ΔA65}	This paper	N/A
<i>D. melanogaster</i> : <i>nolo</i> knock-out: <i>nolo</i> ^{KO}	This paper	N/A
<i>D. melanogaster</i> : UAS-luciferase RNAi: <i>y</i> [1] <i>v</i> [1]; +; P{UAS-LUC.VALIUM10}attP2	Bloomington Drosophila Stock Center	RRID: BDSC_35788
<i>D. melanogaster</i> : UAS- <i>nolo</i> RNAi: <i>y</i> [1] <i>v</i> [1]; +; P{UAS- <i>nolo</i> RNAi TRiP.MHC03983(<i>v</i> +) }attP2	Bloomington Drosophila Stock Center	RRID: BDSC_55296
<i>D. melanogaster</i> : <i>tubulin-Gal4</i> driver: <i>y</i> [1] <i>w</i> [*]; +; P{ <i>tubP-GAL4</i> }LL7/TM3	Bloomington Drosophila Stock Center	RRID: BDSC_5138
<i>D. melanogaster</i> : <i>worniu-Gal4</i> driver: <i>w</i> [*]; P{ <i>wor.GAL4.A</i> }2; Dr[1]/TM3	Bloomington Drosophila Stock Center	RRID: BDSC_56553
<i>D. melanogaster</i> : enhancer assay negative control: <i>w</i> ; +; {DSCP- <i>Gal4</i> }VK33	Gambetta lab	N/A
<i>D. melanogaster</i> : enhancer assay <i>beat-IV</i> intergenic anchor A65: <i>w</i> ; +; { <i>beat-IV A65</i> }VK33	Gambetta lab	N/A
<i>D. melanogaster</i> : enhancer assay <i>nolo</i> intergenic anchor A23: <i>w</i> ; +; { <i>nolo A23</i> }VK33	Gambetta lab	N/A
<i>D. melanogaster</i> : enhancer assay DIP-ε A12 intergenic anchor: <i>w</i> ; +; {DIP-ε A12}VK33	Gambetta lab	N/A
<i>D. melanogaster</i> : enhancer assay DIP-ε A14 intergenic anchor: <i>w</i> ; +; {DIP-ε A14}VK33	Gambetta lab	N/A
<i>D. melanogaster</i> : enhancer assay 5-HT7 A60 intergenic anchor: <i>w</i> ; +; {5-HT7 A60}VK33	Gambetta lab	N/A
<i>Drosophila melanogaster</i> : GAF ^{ΔBTB} ; <i>Halo-Trj</i> ^{ΔPOZ 90-119} /TM6B	Tang et al. ⁵²	N/A
<i>Drosophila melanogaster</i> : CTCF ⁰	Kaushal et al. ⁴¹	N/A

(Continued on next page)

Continued

REAGENT or RESOURCE	SOURCE	IDENTIFIER
<i>Drosophila melanogaster</i> : Cp190 ⁰	Kaushal et al. ²⁰	N/A
<i>Drosophila virilis</i> : wildtype	National Drosophila Species Stock Center	N/A
Oligonucleotides		
Oligonucleotides used for cloning, RT-qPCR and FISH experiments	Table S6	N/A
Software and algorithms		
Custom code	This paper	https://github.com/gambettalab/meta-loops-2022
HiGlass v1.11.8	Kerpedjiev et al. ⁶⁶	https://higlass.io
BWA	N/A	https://bio-bwa.sourceforge.net/
distiller v0.3.3	N/A	https://github.com/open2c/distiller-nf
cooler v0.8.11	Abdennur and Mirny ⁶⁷	https://github.com/open2c/cooler
R v4.2.0	R Core Team	https://www.R-project.org/
ggplot2 v3.3.6	N/A	https://ggplot2.tidyverse.org/
data.table v1.14.2	N/A	https://CRAN.R-project.org/package=data.table
EBIImage v4.38.0	Pau et al. ⁶⁸	http://bioconductor.org/packages/EBIImage
patchwork v1.1.1	N/A	https://CRAN.R-project.org/package=patchwork
rhdf5 v2.40.0	N/A	https://github.com/grimbough/rhdf5
igraph v1.3.5	N/A	https://igraph.org
mlpack v4.0.0	N/A	https://CRAN.R-project.org/package=mlpack
LiftOver	Hinrichs et al. ⁶⁹	http://genome.ucsc.edu/cgi-bin/hgLiftOver
bedtools merge	Quinlan and Hal ⁷⁰	https://bedtools.readthedocs.io/en/latest/content/tools/merge.html
pairtools v1.0.2	Open2C, Abdennur et al. ⁷¹	https://pairtools.readthedocs.io/en/1.0.2/
DESeq2	Love et al. ⁷²	https://bioconductor.org/packages/release/bioc/html/DESeq2.html
UCSC Kent's utilities v377	Kuhn et al. ⁷³	http://hgdownload.cse.ucsc.edu/admin/exe/
CNEr Bioconductor package	Tan et al. ⁷⁴	https://bioconductor.org/packages/release/bioc/html/CNEr.html
LASTZ	Harris et al. ⁷⁵	https://www.bx.psu.edu/~rsharris/lastz/
Fiji software v2.1.0/1.53c	Schindelin et al. ⁷⁶	https://fiji.sc/
bcl2fastq Conversion software v2.20	Illumina	https://support.illumina.com/downloads/bcl2fastq-conversion-software-v2-20.html
Cell Ranger ATAC software v1.2.0	10x Genomics	https://support.10xgenomics.com/single-cell-atac/software/pipelines/latest/installation
Seurat v3.1.5	Stuart et al. ⁷⁷	https://satijalab.org/seurat/
Signac v0.2.5	Stuart et al. ⁷⁸	https://stuartlab.org/signac/
CellRanger v6.1.2	10x Genomics	https://support.10xgenomics.com/single-cell-gene-expression/software/pipelines/latest/installation
clusterProfiler v3.14.0	Yu et al. ⁷⁹	https://guangchuangyu.github.io/software/clusterProfiler/
3D-Distance-Tool	N/A	https://imagej.nih.gov/ij/macros/tools/3D_Distance_Tool.txt
Other		
<i>D. virilis</i> reference genome	Renschler et al. ⁸⁰	GEO: GSE120751
<i>D. melanogaster</i> third instar larva CNS Hi-C, RNA-seq, CTCF ChIP-seq, Cp190 ChIP-seq	Kaushal et al. ⁴¹	GEO: GSE146752

(Continued on next page)

Continued

REAGENT or RESOURCE	SOURCE	IDENTIFIER
<i>D. melanogaster</i> adult brain snATAC-seq	Janssens et al. ⁴⁶	GEO: GSE163697
<i>D. melanogaster</i> adult brain bulk ATAC-seq	Janssens et al. ⁴⁶	GEO: GSE181494
<i>D. virilis</i> whole embryo DNase-seq	Liu et al. ⁴⁷	ArrayExpress: E-MTAB-3797 and E-MTAB-9480

RESOURCE AVAILABILITY**Lead contact**

Further information and requests for resources and reagents should be directed to and will be fulfilled by the lead contact, Maria Cristina Gambetta (mariacristina.gambetta@unil.ch).

Materials availability

All plasmids and fly strains generated in this study are available from the [lead contact](#) without restriction.

Data and code availability

- All sequencing data were deposited at NCBI Gene Expression Omnibus (GEO) and are publicly available as of the date of publication. Accession numbers are listed in the [key resources table](#).
- All original code is publicly available in GitHub. Links to GitHub and all software used as described in the [STAR Methods](#) are listed in the [key resources table](#).
- Any additional information required to reanalyze the data reported in this paper is available from the [lead contact](#) upon request.

EXPERIMENTAL MODEL AND STUDY PARTICIPANT DETAILS**Drosophila**

Drosophila melanogaster and *virilis* were cultured under standard laboratory conditions at 25°C. Samples were prepared as described in the [Methods Details](#). Embryos and larvae were not sexed, but adults were analyzed in 50:50 pools of females:males. All fly strains are listed in the [key resources table](#).

METHOD DETAILS**Micro-C**

Wing imaginal discs and larval brains were dissected from *y w* or *GAF^{ΔBTB}* homozygous third instar larvae, and adult brains were dissected from *y w* 5-day old adult animals in PBST (0.1% Triton-X in PBS). Tissues were fixed in 1 mL of 1% formaldehyde in PBST for 15 min at room temperature. The fixation was quenched by adding 370 μL of 2 M Tris-HCl pH 7.5 and washed with PBST 3 times. 60 discs or 30 brains were collected for each biological replicate. The tissue was then further fixed with 1 mL of 3 mM DSG and 3 mM EGS at room temperature for 45 min. The fixation was stopped by adding 370 μL of 2 M Tris-HCl pH 7.5 and washed with PBST 3 times for 5 min. The tissue was resuspended in 500 μL buffer MB1 (50 mM NaCl, 10 mM Tris, 5 mM MgCl₂, 1 mM CaCl₂, 0.2% NP-40, 1x protease inhibitor cocktail) and permeabilized on ice for 20 min. The tissue was rinsed twice in 1 mL MB1 and digested in 500 μL MB1 with 1.5 μL (30 U) MNase at 37 °C for 10 min. The digestion was terminated by 4 mM EGTA and incubating at 65 °C for 10 min. After two washes in MB2 (50 mM NaCl, 10 mM Tris-HCl pH 7.5, 10 mM MgCl₂), the tissues were treated with 25 U T4 PNK at 37 °C for 15 min and 25 U Klenow Fragment at 37 °C for 15 min, for chewing 3' ends for biotin labeling in 50 μL buffer containing 50 mM NaCl, 10 mM Tris-HCl pH 7.5, 10 mM MgCl₂. Biotin labeling was performed in 75 μL 50 mM NaCl, 10 mM Tris, 10 mM MgCl₂, 100 μg/mL BSA, 2 mM ATP and 5 mM DTT and 67 μM of each nucleotide (dATP and dCTP were biotinylated) at 25°C for 45 min and terminated with 30 mM EDTA incubating at 65 °C for 20 min. After rinsing in 200 μL MB3 (50 mM Tris-HCl pH 7.5, 10 mM MgCl₂) 3 times, proximity ligation was performed in 250 μL ligation mix (50 mM Tris, 10 mM MgCl₂, 1 mM ATP, 10 mM DTT, 100 μg/mL BSA) with 5000 U T4 ligase. Unligated biotin-nucleotides were removed with 500 U Exonuclease III in 100 μL of NEB1 (10 mM Bis-Tris-Propane-HCl pH 7, 10 mM MgCl₂, 1 mM DTT). The sample was then reverse crosslinked in 1 mg/mL Proteinase K and 1% SDS at 65 °C overnight. DNA was extracted with Phenol:Chloroform:Isoamylalcohol, ethanol-precipitated, resuspended in 50 μL of 10 mM Tris-HCl pH 8.5, treated with 2 μL RNase A at 37 °C for 30 min and purified on a ZymoClean spin column. Biotin-labeled DNA was bound to Dynabeads MyOne Streptavidin C1 beads, incubated with BW buffer (5 mM Tris-HCl pH 7.5, 0.5 mM EDTA, 1 M NaCl) at room temperature for 20 min in a total volume of 100 μL, and washed twice with BW at 55 °C for 5 min. The sample was rinsed once in EB buffer (10 mM Tris-HCl pH 7.5) and resuspended in 25 μL EB buffer. 3.5 μL of End Prep Reaction Buffer and 1.5 μL End Prep Enzyme Mix were added and the reaction was incubated at 20 °C for 30 min

for end repair, then heat-inactivated at 65°C for 30 min. The following components were added for adapter ligation: Adapter for Illumina 0.5 µL, Ligation Master Mix 15 µL, Ligation Enhancer 0.5 µL. After incubating at 20°C for 30 min, 15 µL of USER enzyme was added and the reaction was incubated 37°C for 15 min. The reaction was washed in BW buffer once at 55 °C for 5 min and resuspended in 24 µL EB buffer. 25 µl of 2X KAPA HiFi Hot Start Mix, 0.5 µl of 10 µM universal reverse primer and 0.5 µL of 10 µM PE2.0 primer were added to the beads and PCR-amplified for 12 cycles. The library was finally purified with 0.9x Ampure XP beads. Micro-C libraries were sequenced on a NovaSeq S1 100nt Flowcell v1.5 by the Princeton University Genomics Core Facility.

Micro-C analysis

The paired reads were mapped to the dm6 reference by bwa with mem -SP5M -t8. Aligned reads were parsed, sorted and deduplicated by pairtools⁷¹ (<https://doi.org/10.5281/zenodo.2649383>) with default settings. The deduplicated pairs were then selected with '(pair_type == "UU") or (pair_type == "UR") or (pair_type == "RU")' by pairtools. After being split and indexed by pairtools with default parameters, the output pairs were processed and normalized into multi-resolution matrices with default settings by Cooler.⁶⁷

FACS of embryonic neurons, glia, neuroblasts for Hi-C

Embryos were collected on yeasted apple juice agar plates from 8 cages each with 25 grams of flies for 2 hours, then aged at 25°C until the embryos were 6-8, 10-12 or 14-16 hours old. Embryos were then washed off the collection plates, dechorionated by stirring in 50% bleach for 2.5 minutes, extensively rinsed with water, dried by blotting embryos in 125 µm Nitex membrane squares on paper towels, transferred into 50 ml Falcons containing 10 ml of crosslinking solution (50 mM Hepes pH 8, 1 mM EDTA, 0.5 mM EGTA, 100 mM NaCl) and 30 ml of heptane, and fixed by vigorous shaking for 15 minutes at room temperature. Falcons were centrifuged at 500 g for 1 minute, and crosslinking solution and heptane were decanted. Formaldehyde crosslinking was quenched by vigorously shaking embryos for 1 minute in 50 ml of 125 mM glycine in PBS with 0.1% Triton X-100. Falcons were centrifuged again, and the buffer was decanted. Embryos were rinsed in embryo wash (PBS, 120 mM NaCl, 0.1% Triton X-100), dried by blotting in 125 µm Nitex membrane squares on paper towels, transferred to cryovials, weighed, snap-frozen in liquid nitrogen and stored at -80°C. An aliquot of each staged collection was devitized by shaking in eppendorfs containing 0.5 ml of heptane and 0.5 ml of methanol, washed in methanol, rehydrated in 0.5 ml of methanol and 0.5 ml of PBT, rinsed with PBT, stained with 4',6-diamidino-2-phenylindole (DAPI), and mounted on coverslips for observation on a fluorescent microscope with a 20x objective. The stages of at least 100 embryos were counted to estimate the proportions of each stage present in the collection.

For FACS, 0.5 g aliquots of 2 independent biological replicates of 6-8 or 10-12 or 14-16 hour old embryos prepared as above were processed. Frozen embryos were dounce-homogenized in 10 ml of cold homogenization buffer (15 mM Tris-HCl pH 7.4, 15 mM NaCl 60 mM KCl, 340 mM sucrose, 0.2 mM EDTA pH 8, 0.2 mM EGTA pH 8, 1x complete protease inhibitor cocktail) with 20 loose pestle strokes and 10 tight pestle strokes. The lysate was filtered through 2 layers of miracloth rotated by 90° to each other's grain. Nuclei were pelleted by centrifuging at 3'000 g for 10 minutes at 4°C, then blocked in 1 ml of MUSE incubation buffer with 0.1% NP-40 in 2 ml eppendorfs by rotating for 1 hour at 4°C. Primary antibodies against Worniu (Abcam ab196362), Repo (Developmental Studies Hybridoma Bank mouse monoclonal 8D12), or Elav (Developmental Studies Hybridoma Bank mouse monoclonal 9F8A9) conjugated to MUSE oligos were added at a 1 in 1'000 dilution and incubated with nuclei overnight at 4°C. The next day, immunostained nuclei were washed twice in MUSE wash buffer, incubated with MUSE primary amplifiers for 1 hour, washed twice in MUSE wash buffer, incubated with MUSE secondary amplifiers for 1 hour, washed twice in MUSE wash buffer, incubated with MUSE read-out probes for 30 minutes, washed twice in 2xSCCT (2x SCC pH 7, 0.1% Triton X-100) and incubated in 2xSSCT with DAPI overnight at 4°C. The next day, nuclei were passed up and down 10 times through a 20G needle and 10 times through a 22G needle, filtered through a 35 µm nylon mesh, and FAC-sorted into PBT (PBS, 0.1% Triton X-100, 1x complete protease inhibitor cocktail) on a Beckman Coulter Astrios EQ instrument. Aliquots of 1 million nuclei were transferred to eppendorfs and pelleted by centrifuging 5'000 g 5 minutes at 4°C in a swinging bucket rotor. PBT was removed leaving approximately 20 µl in the tube, and nuclei were snap-frozen and stored at -80°C.

Hi-C

About 10 dissected adult CNSs or 30 dissected third instar larval CNSs per biological replicate (2-3 biological replicates per genotype, except for the neuroblasts from 6-8 hour old embryo sample for which only a single biological replicate was used) were crushed in RPMI supplemented with 10% fetal bovine serum using a micro-pestle. Nuclei were fixed in 1% (v/v) formaldehyde for 10 minutes at room temperature. Crosslinking was stopped by adding 200 mM glycine, then nuclei were washed in PBS and snap-frozen for -80°C storage.

For Hi-C, CNS nuclei prepared above from dissected CNSs or 1 million FAC-sorted embryonic nuclei per replicate were restricted with MseI and Csp6I, restricted ends were marked with biotin, and then ligated. DNA was purified by proteinase K digestion and reverse crosslinking at 65°C for 6 hours, then sonicated in AFA microtubes in a Covaris S220 sonicator, and purified on SPRIselect beads (Beckman Coulter B23319). DNA was end-repaired, A-tailed and ligated to barcoded adapters using the NEBNext Ultra II DNA Library Prep kit for Illumina (NEB E764S), then enriched for pairwise DNA junctions by biotin pull-down using Dynabeads MyOne Streptavidin T1 (Invitrogen 65601) beads following the manufacturer's instructions. Libraries were amplified using KAPA HiFi HotStart Ready Mix (Roche KK2501) and purified on SPRIselect beads. 4 nM equimolar pools of multiplexed Hi-C libraries were subjected to 150 bp paired-end sequencing on HiSeq4000 instruments.

Hi-C analysis

FASTQ files were mapped to the reference genome using distiller v0.3.3 (<https://github.com/open2c/distiller-nf>). The following reference genomes were used: FlyBase version FB2020_05, dmel_r6.36 (dm6) for *Drosophila melanogaster*; and GSE120751_Dvir_HiC.fa.gz downloaded from <ftp://ftp.ncbi.nlm.nih.gov/geo/series/GSE120nnn/GSE120751/suppl/>⁸⁰ for *Drosophila virilis*. For each sample, unique pairs of reads with high mapping quality scores on both sides (MAPQ \geq 30) from all biological replicates were aggregated into contact matrices using cooler⁶⁷ v0.8.11 (<https://github.com/open2c/cooler>) and stored into multiresolution cooler files (1kb, 2kb, 4kb, 8kb, 16kb, 32kb, 64kb, 128kb, 256kb, 512kb). All contact matrices were normalized using the iterative correction procedure implemented in cooler. Hi-C maps were visualized in HiGlass⁶⁶ and R.

Meta-loop calling

Meta-loops were called on WT *D. melanogaster* third instar larval CNS Hi-C maps (data from Kaushal et al.⁴¹) or on WT *D. virilis* adult CNS Hi-C maps. Numbers of Hi-C read pairs between pairs of restriction fragments for the 3 biological replicates of WT larval CNSs were downloaded from Gene Expression Omnibus accession GSE146752 (<https://www.ncbi.nlm.nih.gov/geo/query/acc.cgi?acc=GSE146752>). Using cooler v0.8.11 (<https://github.com/open2c/cooler>), read pairs from all replicates were pooled, binned at 2 kb (for *D. melanogaster*) or 4 kb (for *D. virilis*) and normalized using iterative correction. The per chromosome expected number of Hi-C contacts as a function of genomic distance was obtained by evaluating the mean number of normalized Hi-C contacts (considering only pairs of bins within the selected chromosome arm) as a function of genomic distance and smoothing the resulting curve with a spline [R function `smooth.spline()` applied to $\log(\text{mean count})$ vs $\log(\text{distance})$]. The observed-over-expected matrix was then generated by dividing the normalized Hi-C contact matrix by the expected number of Hi-C contacts at the corresponding genomic distance. Loop calling on the observed-over-expected Hi-C matrix occurred in two main steps.

In step 1, regions with high Hi-C contacts were identified. Pairs of bins satisfying all of the following conditions were selected: (1) Observed-over-expected matrix entry for this pair of bins >30 (i.e. contacts are 30-fold higher than expected for pairs of bins at this distance). (2) Normalized Hi-C count matrix entry for this pair of bins is larger than the per chromosome expected number of Hi-C contacts at distance 100 kb (i.e. the absolute normalized count is at least as high as the normalized count between bins separated by 100 kb). (3) Both bins are not in a low coverage region. Low coverage regions were determined by evaluating the total number of raw Hi-C counts per 128 kb bin for all 128 kb bins in the genome and computing their median and mad (median absolute deviation). Low coverage 128 kb bins are defined as those with counts lower than $\text{median}-2*\text{mad}$. Low coverage 2 kb (for *D. mel.*) or 4 kb (for *D. Vir.*) bins are those within a low coverage 128 kb bin. Retained pairs of 2 kb (for *D. mel.*) or 4 kb (for *D. Vir.*) bins were then clustered using single linkage hierarchical clustering with Euclidean distance in the plane (bin1 position, bin2 position) and using a cutting distance of 5 bins. Only clusters satisfying all of the following criteria were retained (other clusters were considered as noise): (1) The cluster contains at least 10 selected pairs of bins. (2) The cluster bounding box [in the (bin1 position, bin2 position) plane] measures at least 5 bins in both directions.

In step 2, loops were identified in each region of high Hi-C contacts. For each cluster retained in step 1, we used image analysis methods to detect peaks (i.e. meta-loops) in the observed-over-expected matrix. An observed-over-expected image was created from the observed-over-expected matrix by extracting all pairs of bins within the bounding box of clusters extended by 20 bins on each side. Invalid bins (i.e. bins flagged as low coverage and ignored during normalization by cooler) were excluded from the image. A second image with normalized Hi-C counts was also created in the same way. To reduce noise, both images were blurred using a Gaussian filter with a standard deviation of 1 pixel (2 kb bin for *D. mel.* or 4 kb for *D. vir.*). Local maxima in the blurred observed-over-expected image were found as the global maxima within each of the regions obtained by watershed segmentation (using EBImage⁶⁸ function `watershed()` with flooding threshold 5). To mitigate the loss of precision due to blurring, the position of each local maximum was further adjusted to the pixel with the highest non-blurred observed-over-expected value within a 3x3 pixel neighborhood. Local maxima satisfying all of the following conditions were retained whereas others were considered as noise: (1) The value of the blurred observed-over-expected image at the position of the local maximum is >30 (i.e. 30-fold contact increase compared to expected). (2) The value of the blurred observed-over-expected image at the position of the local maximum is larger than half of the global maximum in this image. (3) The value of the blurred normalized Hi-C count image at the position of the local maximum was larger than the per chromosome expected number of Hi-C contacts at distance 100 kb. (4) The position of the local maximum is inside the bounding box of the cluster (i.e. not within the 20 bins added around the bounding box).

The resulting meta-loop anchors (i.e. local maxima retained after step 2) in *D. melanogaster* were associated with the presence of an accessible chromatin peak defined by DNase-seq in FACS-purified neurons (immunostained with anti-Elav antibody) from 10-12 hour old embryos from Reddington et al.⁴⁰ Therefore, the coordinates (chr, start, end, summit) of the nearest 10-12h neuron DNase hypersensitivity site (DHS) were attributed to each loop anchor (the distance was measured between the center of the loop anchor 2 kb bin and the DHS summit). If more than one DHS summit overlapped the 2 kb bin of the loop anchor, then all overlapping DHSs were conservatively kept, and the start, end and summit positions were taken as the minimum, maximum and mean of all overlapping DHS start, end and summit positions respectively.

Meta-loops automatically called in *D. melanogaster* (58 total) with the algorithm described above were then further manually curated. 51/58 (88%) automatically called meta-loops were validated by manual curation and 7/58 were considered false-positives. False positive meta-loops appeared to be artifacts arising by mapping or chromosomal rearrangements rather than pairwise associations of distal TADs and lacked a chromatin accessibility peak underlying the Hi-C interaction peak. 7 manually curated

meta-loops were not automatically called, considered false-negatives, and added to our final list of 58 curated meta-loops. False negatives were missed when interaction peaks were “drowned” in regions of high interaction frequency, for example within a meta-domain with particularly high interactions or when located close to another meta-loop. Indeed, 7/7 (100%) meta-loops that we classified as false-negatives are present in the same meta-domain as an automatically called meta-loop. Each curated loop anchor was manually matched to an overlapping 10-12h neuron DHS (or several DHSs in case of doubt) as for the automatically called loops. Finally, 10 intra-TAD loops involving meta-loop anchors were manually annotated and added to the final list of 58 meta-loops + 10 intra-TAD loops = 68 loops involving meta-loop anchors shown in Figure S1 and listed in Table S2. Note that we never observed a meta-loop anchor to loop to another locus than a meta-loop anchor.

Using a similar procedure as described above for manual curation of meta-loops automatically called in *D. virilis*, 51/54 (94%) automatically called loops were validated and 3/54 were considered false-positives (because they were likely artifacts or because one was arguably an intra-TAD loop). 4 meta-loops were considered false-negatives, leading to a final list of 58 curated meta-loops in *D. virilis*. The coordinates of called meta-loop anchors were then aligned to overlapping DNase-seq peaks from old (25-28 hours after egg-lay) *D. virilis* embryos.⁴⁷ Specifically, the minimum and maximum of start and end coordinates of overlapping DNase-seq peaks were taken as the anchor coordinates. Finally, 6 intra-TAD loops involving meta-loop anchors were then added to obtain a total of 64 considered loops involving meta-loop anchors listed in Table S3.

Loop anchor classification

Promoter-proximal loop anchors were defined as those within ± 200 bp of a protein coding gene TSS (FlyBase version 6.36 for *D. melanogaster*, GSE120751 transcript annotations in GTF format for *D. virilis*). When an anchor was within ± 200 bp of >1 protein coding gene TSS, all these genes were attributed to the anchor. The remaining loop anchors were defined as intergenic, and the closest TSS was attributed to each intergenic anchor.

Differential analysis of Micro-C or Hi-C interactions

For the differential analyses presented in Figures 6B and 7B, meta-loop coordinates were standardized to 5 kb in a bedpe format. Cooler files were dumped into the interaction matrix at 100 bp resolution using the dump function from cooler. The dumped matrix was then intersected with the meta-loop coordinates using the pairToPair function from bedtools with “both” mode. Total counts of each meta-loop were summed. The count lists for individual samples were summarized as a count table in R. The count table was used for differential analysis using the DESeq2⁷² package in R. Statistically significantly changed loops were filtered using an adjusted P value ≤ 0.01 . The volcano plot was generated with ggplot2.

Analysis of three-way interactions between meta-loop anchors

To determine if multiple interactions involving a single meta-loop anchor occur concurrently, we re-analyzed sequencing reads from our published Hi-C experiments in WT larval CNSs⁴¹ to infer information on higher-order chromatin interactions. We relied on the fact that Hi-C experiments were performed using in-nucleus ligation and each sequenced DNA molecule possibly obtained via several ligations, representing concurrent interactions in a single nucleus. We used a local sequence aligner, bwa mem⁸¹ version 0.7.17 with options -E50 -L0 -5 for mapping. This aligner was particularly suitable for chimeric reads that had more than one alignment that each uniquely mapped to a distinct region in the genome. To extract the alignments, we used pairtools parse from the pairtools suite⁷¹ version 1.0.2. We detected cases in which the same DNA fragment was sequenced in both reads forming the paired-end read, and further merged such alignments. The specific option used, --walks-policy all --add-columns pos5, pos3 --no-flip, ensured that all alignments are reported with their full genomic coordinates in the order in which they were sequenced.

We merged all ~ 597 M processed paired-end reads from the three replicates of WT larval CNS Hi-C data. ~ 62 M (10.7%) of them had three or more alignments, allowing for quantification of three-way interactions. Only ~ 7.5 M (1.3%) of paired-end reads had more than three alignments in total, hence we did not pursue the analysis of 4-way or higher-order interactions. We further followed an approach proposed by Bintu et al.⁸² to quantify the cooperativity of three-way interactions. We focused on 21 triplets of meta-loop anchors, called looping triplets, such that all three pairs of anchors within the triplet form a loop. Since all the loops are constrained to a single chromosome arm, all the looping triplets are too.

Let us consider one such looping triplet, and denote its three anchors by A, B, and C, according to their chromosomal order. We denote by n_A the number of paired-end reads involving anchor A, i.e. paired-end reads having an alignment that maps to the genome no more than 2 kb (i.e. the resolution of the Hi-C maps) away from anchor A. Similarly, we denote by n_{AB} the number of paired-end reads involving both anchors A and B, and we generalize this notation for any anchors and their higher number. To test whether locus A facilitates or inhibits the interaction between loci B and C, we first calculated $f(C|B) = n_{BC} / n_B$ as the fraction of reads involving B that also involve C. Similarly, we can calculate $f(C|AB) = n_{ABC} / n_{AB}$ as the fraction of reads involving A and B that also involve C. The fold change between these two fractions, namely the triplet cooperativity factor $f(C|AB)/f(C|B)$, quantifies the impact of A on the interaction between B and C. The above-described measure has two important properties. First, because we consider A, B, and C in their chromosomal order, the anchor A is not between B and C, and the effect of A is beyond polymeric nature of chromatin fiber. Second, it algebraically follows that $f(C|AB) / f(C|B) = (n_{ABC} \cdot n_B) / (n_{AB} \cdot n_{BC}) = f(A|BC) / f(A|B)$, and the cooperativity factor is independent of the direction of traversing the chromosome.

Positive values of the triplet cooperativity factor indicate that the two extreme anchors (A and C) facilitate interactions between the two other anchors. We systematically compared the values of the triplet cooperativity factor for all 21 looping triplets of meta-loop anchors, and for a set of control triplets of genomic regions defined as follows. For each looping triplet of anchors A, B, and C (in this chromosomal order), we defined anchor C' located to the left of A and positioned such that the distance between B and C is equal to the distance between C' and A. The control triplet of anchors C', A, and B is characterized by the same inter-anchor distances as the looping triplet A, B, and C, but typically involved very few alignments on C' side. Hence, we defined the anchor C'' by extending the anchor C' by 100 kb on both sides, noting that in no case did the anchors C'' and A overlap. From each looping triplet of anchors A, B, and C, we derived two control triplets of regions, namely C'', A, and B, as well as B, C, and A'' obtained correspondingly.

Loop strength measurement

Strengths of loops involving meta-loop anchors (plotted in [Figures 3B](#), [S1B](#), and [S6D](#)) were measured as the normalized Micro-C or Hi-C count divided by the average normalized Micro-C or Hi-C count at the same genomic distance and on the same chromosome as the pair of bins containing the loop anchors. The normalized Micro-C or Hi-C count was estimated as the average normalized Micro-C or Hi-C count over 3x3 pairs of bins centered on the loop (i.e. the bin containing the loop anchors and the nearest neighbor bins). The 3x3 neighborhood was used to mitigate the problem of missing data (i.e. bins flagged as low coverage and ignored during normalization by cooler), in particular for samples in which the loop is weak or absent. All measurements were done using 1.6 kb Micro-C resolution matrices and 2 kb resolution Hi-C matrices.

GO term enrichment analysis

For Gene Ontology (GO) term enrichment analysis, we extracted FlyBase IDs of 35 genes attributed to meta-loop promoter anchors. We also considered the set of 62 genes attributed as the closest to intergenic anchors. Each of the input gene sets was compared to the universe of all *Drosophila melanogaster* coding genes, using `enrichGO` function from the `clusterProfiler` R package⁷⁹ v3.14.0 and gene annotations from the `org.Dm.eg.db` Bioconductor package version 3.10.0. In our over-representation analysis, we considered terms from all three GO sub-ontologies (Biological Process, Molecular Function, and Cellular Component), and identified significantly enriched terms at FDR of 0.05, adjusting for multiple hypothesis testing using Benjamini-Hochberg method. The enrichment was plotted as a dotplot graph from the `clusterProfiler` package. Terms were ordered by gene enrichment ratio, i.e. the fraction of genes in the input set associated with the given GO term. UP to 20 terms with the highest gene enrichment ratio are shown.

RNA-FISH

DNA templates for *5-HT7*, *beat-IV*, *DIP-ε*, *Mp*, *nolo* or a reporter gene used in the transgenic enhancer assay were PCR-amplified from genomic DNA or a template plasmid, respectively, using primer sequences in [Table S6](#). These inserts were cloned upstream of a T7 RNA polymerase promoter oriented such that it transcribes an antisense transcript to the mRNA. Labeled RNA probes were then generated from template DNA by in vitro transcription with Dig-UTP labeling mix (Roche 11277073910) and T7 RNA polymerase (Roche 10881767001). After DNase I digestion for 20 minutes at 37°C, probes were fragmented by incubating 20 minutes at 65°C in 60 mM Na₂CO₃, 40 mM NaHCO₃ pH 10.2, precipitated in 300 mM sodium acetate pH 5.2, 1.25 M LiCl, 50 mg/ml tRNA and 80% EtOH, resuspended in 50% formamide, 75 mM sodium citrate pH 5, 750 mM NaCl, 100 μg/ml salmon sperm DNA, 50 μg/ml heparin and 0.1% Tween20, and stored at -20°C. Embryos were fixed in 4% paraformaldehyde for 30 minutes at room temperature, washed, and then stored in 100% MeOH at -20°C. Samples were rehydrated in PBS with 0.1% Tween20, post-fixed in 4% paraformaldehyde for 20 minutes at room temperature, progressively equilibrated to hybridization buffer (50% formamide, 75 mM sodium citrate pH 5, 750 mM NaCl) and heated to 65°C. RNA probes were diluted 1:50 in hybridization buffer, denatured at 80°C for 10 min then placed on ice, and added to the samples overnight shaking at 65°C. Samples were washed 6 times 10 minutes in hybridization buffer at 65°C, then progressively equilibrated to PBS with 0.1% Triton X-100. Samples were incubated overnight at 4°C in anti-Dig peroxidase (Roche 11207733910) diluted 1:2000 in PBS, 0.1% Triton X-100, 1x Western blocking reagent (Sigma 1921673). Samples were washed 6 times 10 minutes in PBS with 0.1% Tween20, labeled with Cyanine 3 tyramide in the TSA Plus kit (Perkin Elmer NEL753001KT) for 3 minutes at room temperature, washed 6 times 10 minutes in PBS with 0.1% Tween20, and finally mounted with DAPI to stain DNA. Images were acquired on a Zeiss LSM 880 microscope with a 20x objective and visualized with Fiji software v2.1.0/1.53c.⁷⁶

DNA-FISH

5 kb PCRs from genomic DNA using primers indicated in [Table S6](#) were cloned into a plasmid. 2 μg of miniprep plasmid DNA was nick-translated (Abbott Molecular 07J100-001) following the manufacturer's protocol in the presence of 10 μM aminoallyl-dUTP-XX-ATTO-488 (Jena Bioscience NU-803-XX-488-S) or aminoallyl-dUTP-ATTO-550 (Jena Bioscience NU-803-550-S) at 15°C for 5 hours, and stored at -20°C. Prior to DNA-FISH, both probes per two-color DNA-FISH experiment were co-precipitated in the presence of salmon sperm DNA, and resuspended in 100% formamide. 0-24 hour old WT embryos were dechorionated and fixed in 4% formaldehyde for 20 minutes at room temperature, washed, and then stored in 100% MeOH at -20°C. Samples were rehydrated in 2xSSCT (30 mM sodium citrate dihydrate pH 7.4, 300 mM NaCl, 0.1% Tween20), treated with RNase A for 30 minutes at room temperature, washed in 2xSSCT, progressively equilibrated to 50% formamide in 2xSSCT, and incubated for 2 hours at 37°C. DNA-FISH probes were mixed with the embryos in 25 μl total of 2xSSC, 10% (w/v) dextran sulfate, 50% formamide, heated to 80°C for

10 minutes, then incubated at 37°C overnight in the dark. Embryos were washed in 50% formamide in 2xSSCT, then 20% formamide in 2xSSCT, then 2xSSCT at 37°C. Embryos were then immunostained overnight at 4°C with anti-Elav rat monoclonal antibody (clone 7E8A10 from Developmental Studies Hybridoma Bank) diluted 1:50 in PBS, 0.1% Tween20, 1x Western blocking reagent (Sigma 1921673). Samples were washed, then incubated in the dark for 2 hours at room temperature with Alexa 647 anti-rat IgG (Thermo Fisher A21247) diluted 1:200 in PBS, 0.1% Tween 20, 1x Western blocking reagent (Sigma 1921673). Samples were washed in PBS with 0.1% Tween20, and finally mounted with DAPI to stain DNA. Images were acquired on a Zeiss LSM 880 microscope with a 63x oil objective and visualized with Fiji software v2.1.0/1.53c.⁷⁶ 3D distances between two color DNA-FISH spots were counted with the 3D distance tool Fiji plugin downloaded from https://imagej.nih.gov/ij/macros/tools/3D_Distance_Tool.txt.

RNA-DNA-FISH

For RNA-DNA-FISH experiments, RNA-FISH was performed first, RNAs were then digested by RNase A (the RNA-FISH signal perdures because it arises from fluorescent labeling of tyrosine residues of proximal proteins), and DNA-FISH was subsequently performed as described above.

HCR-RNA-FISH

The third instar larval tissue was dissected in PBST (0.1% Triton-X in PBS) and fixed in 4% formaldehyde diluted in PBST for 20 min at room temperature. The tissue was briefly rinsed in PBST 2 times, treated with 100% methanol, 75% methanol in PBST, 50% methanol in PBST and 25% methanol in PBST for 5 min at room temperature each time, then washed in PBST 3 times for 5 min at room temperature. The tissue was further processed following the protocol described in <https://files.molecularinstruments.com/MI-Protocol-RNAFISH-GenericSolution-Rev8.pdf> with the following modifications. The hybridization buffer, wash buffer and amplification buffer used in the protocol were purchased from Molecular Instruments. The probe stocks were designed and ordered from Molecular Instruments. For hybridization, oligos were mixed at 16 nM final concentration in the hybridization buffer. For amplification, the incubation time was reduced to 1.5 hours compared to the original protocol.

RT-qPCR on larval CNSs, adult heads or whole-bodied flies

For RT-qPCR on larval CNSs shown in Figure 6E, 15 larval CNSs of WT (*y w*) or *GAF^{ΔBTB}* mutants were dissected in biological triplicates and incubated in 500 μl TRIzol (Invitrogen 15596026) at room temperature for 10 minutes. RNA was extracted following the manufacturer's instructions and dissolved in 10 μl of 10 mM Tris-HCl pH 8. 1 μg of RNA was reverse transcribed with SuperScript IV (Invitrogen 18091050) with an oligo dT primer following the manufacturer's instructions. qPCR was performed with SYBR green (Invitrogen 4367659) on a ViiA 7 Real-Time PCR System (ThermoFisher).

For RT-qPCR on adult flies or adult heads shown in Figures S6A and S6B, total RNA was extracted from 10 heads (5 female, 5 male) or 4 flies (2 females, 2 males) of WT (*w¹¹¹⁸*), *nolo^{ΔA23}* or *beat-IV^{ΔA65}* mutants in biological triplicates with TRIzol as described above. 500 ng of RNA were reverse transcribed with GoScript (Promega A2801) with random hexamers following the manufacturer's instructions. qPCR was performed with GoTaq (Promega A600A) on a QuanStudio 6 Flex Real-Time PCR System (ThermoFisher).

Fold changes of gene expression in mutants relative to WT controls were calculated using the delta-delta CT method, referring to the *GAPDH* signal (for *GAF^{ΔBTB}* mutants) or to *RpL15* (for *nolo^{ΔA23}* or *beat-IV^{ΔA65}* mutants) and normalizing by the mean expression level of WT for each primer pair. A two-sided unpaired heteroscedastic t test was performed to test the significance of differential expression in knockout versus WT backgrounds.

CRISPR/Cas9-mediated intergenic anchor deletions

beat-IV^{ΔA65} and *nolo^{ΔA23}* mutants were generated by CRISPR-Cas9-mediated genome editing using small guide RNAs (sgRNAs) flanking the regions chosen for deletion: 199 bp (dm6 coordinates chr3R:28,654,618-28,654,816) for *beat-IV^{ΔA65}*, or 814 bp (dm6 coordinates chr2L:20,120,764-20,121,578) for *nolo^{ΔA23}*. Up to six sgRNAs per targeted intergenic anchor were cloned (using primers listed in Table S6) downstream of U6:1, U6:2 and U6:3 promoters,⁸³ then assembled into a single transgene and integrated by site-specific recombination into the ZH86Fb landing site.⁸⁴ All *Drosophila* injections were performed by FlyORF, Zurich. Males expressing both sgRNAs and Cas9 in their germline (*nanos-Cas9*)⁸³ were crossed to balancer females, and crosses of single sons were set up with balancer females. After three days, the males were sacrificed and genotyped by PCR. Males and females harboring independently isolated CRISPR knockout alleles were crossed and resulting trans-heterozygous larvae were analyzed by Hi-C and scRNA-seq.

nolo CRISPR/Cas9-mediated knock-outs and RNAi

nolo^{KO} alleles were generated by crossing mothers expressing *nanos-Cas9*⁸³ to fathers transgenically expressing two *nolo* sgRNAs targeting exon 2 (Bloomington stock 83042). Transheterozygotes for two independently isolated *nolo^{KO}* alleles were used for phenotypic analysis, and *w¹¹¹⁸* animals were used as WT control. For *nolo* tissue-specific knockdowns, transgenic *UAS-luciferase RNAi* (Bloomington stock 35788) or *UAS-nolo RNAi* mothers (Bloomington stock 55296) were crossed to fathers with transgenic Gal4 drivers expressed in neuroblasts [*worniu-Gal4* (Bloomington stock 56553)] or ubiquitously [*tubulin-Gal4* (Bloomington stock 5138)].

Drosophila viability tests

Three or four sets of 30–40 third instar larvae of desired genotypes were transferred into separate vials and the number of fully hatched adults was recorded. Viability defects in *nolo* knock-out and knock-down animals were only observed at the pupa-to-adult transitions, whereas larva-to-pupa transitions were similar to wildtype.

Analysis of neuromuscular junctions

Third instar larvae were dissected in chilled PBS and fixed for 8 minutes in Bouin's fixative. WT controls were the *w¹¹¹⁸* line. The dissected preparations were permeabilized in PBS with 0.3% Triton X-100 (PBT) for 45 minutes at room temperature, blocked in PBT with 3% goat serum for 1 hour, incubated overnight with mouse anti-VGlut⁶⁵ at 4°C, and finally incubated with secondary antibody and cellular dyes (Alexa 647 goat anti-HRP, Jackson 123-605-021 1:400; Alexa 555 anti-mouse IgG, Thermo Scientific A-21422 1:200) for 2 h at room temperature. Samples were mounted in Vectashield and imaged with LASX acquisition software (Leica) on a Leica SP8 confocal microscope using a 63x/1.40 NA oil HCPLAPOC52 objective with a 0.14 mm working distance. Maximum intensity projections of confocal stack images and image cropping were performed in Fiji ImageJ and images saved as.tif files. Thresholding of the resulting images was used to select regions of interest (ROIs) for area quantification, using the Default method of auto thresholding available in Fiji ImageJ. The selected ROIs were used to measure area values, which were recorded in a.csv file. One neuromuscular junction in each of ≥ 8 larvae were imaged per genotype.

Transgenic enhancer assays

Intergenic anchors were PCR-amplified from genomic DNA with primers from Table S6 and cloned upstream of a minimal *Drosophila* synthetic core promoter driving transcription of a reporter gene. Transgenes were inserted into the VK33 landing site on chromosome 3 by attP-attB recombination.⁸⁵ Embryos homozygous for the reporter transgene were analyzed in Figure S6G.

scATAC-seq on third instar larval central nervous systems

20 wandering third instar larvae were dissected in ice-cold Schneider's medium supplemented with 10% fetal bovine serum, washed in Rinaldini solution (0.36 mM NaH₂PO₄·H₂O, 11.9 mM Okay, 137 mM NaCl, 2.7 mM KCl, 5.6 mM glucose·H₂O), dissociated in 0.5 μg/μl collagenase I (Sigma C2674) for 1 hour at room temperature, washed in Schneider's medium, and dissociated into single cells by pipetting up and down several times with wide-bore tips. The cell suspension was passed through a 40 μm cell strainer, washed in PBS with 0.04% (w/v) BSA, and counted. Nuclei were extracted in 0.1x lysis buffer (1 mM Tris-HCl pH 7.4, 1 mM NaCl, 0.3 mM MgCl₂, 0.01% Tween20, 0.01% NP-40, 0.001% digitonin, 0.1% BSA) for 5 minutes on ice, washed in cold wash buffer (10 mM Tris-HCl pH 7.4, 10 mM NaCl, 3 mM MgCl₂, 0.1% Tween20, 1% BSA), resuspended in 1x nuclei buffer (provided by the manufacturer), counted, and diluted to 2500 nuclei/μl. 20000 nuclei were then loaded and processed according to the instructions of 10x Genomics Chromium single cell ATAC reagent kits solution v1.0 (CG000168 revB January 2019). scATAC-seq libraries were sequenced on an Illumina HiSeq 4000 using HiSeq 3000/4000 SBS kit reagents according to 10X Genomics recommendations (50 cycles read1, 8 cycles i7 index read, 16 cycles i5 index read, 50 cycles read2). Sequencing data were demultiplexed with bcl2fastq Conversion software (v 2.20, Illumina).

scRNA-seq on third instar larval central nervous systems

15 wandering third instar larvae were dissected in ice-cold Schneider's medium supplemented with 10% fetal bovine serum, washed in Rinaldini solution (0.36 mM NaH₂PO₄·H₂O, 11.9 mM NaHCO₃, 137 mM NaCl, 2.7 mM KCl, 5.6 mM glucose·H₂O), dissociated in 2 μg/μl collagenase I (Sigma C2674) and 2 μg/μl papain (Sigma P4762) for 50 minutes at room temperature, and dissociated into single cells by pipetting up and down several times. The cell suspension was washed in PBS with 1% BSA and RNase inhibitor (Sigma 3335399001), passed through a 35 μm cell strainer, resuspended in PBS with 1% BSA and RNase inhibitor, filtered again through a 0.35 μm cell strainer, counted and assessed for viability on a Moxi V instrument (Witec MXV102), and diluted to 1000 cells/μl. 20 μl (20000 cells) were processed according to the instructions of 10x Genomics Chromium Next GEM sc 3' reagent kits v3.1 dual index (CG000315 RevC August 2021). scRNA-seq libraries were sequenced on an Illumina NovaSeq 6000 using SBS cartridge 100C v 1.5 kit reagents according to 10X Genomics recommendations (28 cycles read1, 10 cycles i7 and i5 index reads, 90 cycles read2). Sequencing data were demultiplexed with bcl2fastq Conversion software (v 2.20, Illumina).

scATAC-seq analysis

Raw sequencing data (305 million read pairs, 14,957 cells) were processed using the Cell Ranger ATAC software v1.2.0, using a custom *D. melanogaster* reference based on FlyBase version FB2020_05, dmel_r6.36 (dm6) genome assembly. The read filtering and alignment, identification of transposase cut sites, detection of accessible chromatin peaks, cell calling and count matrix generation for peaks were performed by cellranger-atac count, using the default settings. The custom peak calling algorithm implemented in Single Cell ATAC fits a probabilistic model to a smoothed cut site distribution and sets a global signal threshold at the specificity level of 95%. The resulting 28,877 accessible chromatin peaks, filtered peak-barcode matrix in HDF5 format, filtered fragments and per-barcode cell calling table were further analyzed in R (v3.6.3) using the R packages Seurat (v3.1.5)⁷⁷ and Signac (v0.2.5).⁷⁸

For each cell, we computed the following quality metrics: number of fragments overlapping peaks, percent reads in peaks, TSS enrichment score and short-to-mononucleosomal reads ratio. Cells with the number of fragments overlapping peaks outside the

5%–95% quartile (672–18,642) were excluded from further analysis. The resulting count matrix of 28,877 peaks and 13,461 cells was used for latent semantic indexing (LSI). First, term frequency-inverse document frequency (TF-IDF) matrix was computed using the Signac function RunTFIDF and default implementation method. The resulting TF-IDF matrix was then decomposed using partial singular value decomposition implemented in the RunSVD function in Signac.

To obtain two-dimensional projection, we performed Uniform Manifold Approximation and Projection (UMAP) dimensional reduction, applying Seurat function RunUMAP and using LSI components 2 to 30. The first LSI component was found to be highly correlated with the total number of counts per cell, and hence excluded from the analysis as capturing technical variation (sequencing depth). Cells were clustered into 19 cell clusters by Seurat function FindClusters, using LSI components 2 to 30 and running the smart local moving (SLM) algorithm at the default resolution of 0.8. The 19 clusters were manually associated to one of three broad cell types (neuronal, neuroblast and glia) based on the accessibility of a 2 kb region upstream of the transcription start site of selected marker genes, respectively: *embryonic lethal abnormal vision (elav)*, *Notch (N)* and *reversed polarity (repo)*.

scRNA-seq analysis

Raw sequencing reads (143 million raw reads for WT, 192 million raw reads for *beat-IV^{ΔA65}*, 157 million raw reads for *nolo^{ΔA23}*) were processed with Cell Ranger v6.1.2 software using the *Drosophila melanogaster* reference genome BDGP6.28.101. Resulting UMI count matrices (h5 files filtered_feature_bc_matrix.h5) were imported into and analyzed in R (v. 4.0.0) using the R package Seurat (v3.1.5).⁷⁷ Cells with less than 1000 or more than 30000 UMI counts, expressing less than 200 or more than 7000 genes, and detecting more than 3% of mitochondrial genes, were removed from the analysis. This resulted in the following total numbers of cells and genes remaining for the analysis: 4460 cells and 8905 genes in WT, 4431 cells and 8905 genes for *beat-IV^{ΔA65}*, and 5871 cells and 8698 genes for *nolo^{ΔA23}*.

All samples were first processed independently following the standard Seurat processing workflow with default settings unless specified: Log-normalization of the raw counts (NormalizeData with scale factor set to 10000), identification of the most variable genes (FindVariableFeatures, with nFeature set to top 2000 and selecting the vst method), and scaling the data (ScaleData, setting the center parameter to FALSE). After processing, objects were then integrated using the Seurat Canonical Correlation Analysis (FindIntegrationAnchors using CCA dimensions 1–20 and IntegrateData), and further processed applying the same steps as described above.

22 clusters were identified at a resolution of 0.5 (FindNeighbors and FindClusters, running the Louvain algorithm). Clusters were manually associated to one of five broad cell-types shown in Figure 5A based on the expressions of selected markers shown in Figure S6C. For visualization, a 2-dimensional UMAP was generated from the first 10 principal components (RunPCA and runUMAP).

The differential expression analysis in either mutant relative to WT was performed from the integrated Seurat object for each of the 22 cell clusters (FindMarker using a Wilcoxon Rank Sum test).

Comparative analysis of meta-loops in *D. mel.* and *D. vir.* adult central nervous systems

We used CNER Bioconductor package⁷⁴ complemented with UCSC Kent's utilities (<http://hgdownload.cse.ucsc.edu/admin/exe/>)⁷³ to identify conserved elements. First, we converted *D. melanogaster* and *D. virilis* soft-masked genome sequences from FASTA format to twoBit format, and used the LASTZ sequence alignment program (<https://www.bx.psu.edu/~rsharris/lastz/>)⁷⁵ with the default (HOXD70) scoring matrix to obtain their pairwise alignment. We converted the LASTZ output from .lav to .psl format using lavToPsl, and joined matching alignments located next to each other into chains using axtChain with the default (medium) linear gap costs. The chains were further sorted using chainMergeSort, filtered using chainPreNet to remove isolated chains, and combined to alignment nets using chainNetSyntenic. Final.net.axt files were obtained from the previous net and chain files using netToAxt.

We further combined the two.net.axt files obtained by taking one of the *Drosophila* genomes as query and the other one as reference, using the CNE function from the CNER package. Conserved elements were identified by scanning the two sets of alignments using ceScan for regions with at least 80% identity over 50 alignment columns (nucleotide positions). We merged the conserved elements using cneMerge, as we perform their detection with each genome as reference, leaving intact the elements that overlap only in one of the genomes. As some of the conserved elements might be unannotated repeats which were not filtered out by soft-masking, we realigned each element sequence against the respective genome using BLAT⁸⁶ and used blatCNE to discard the elements with more than four BLAT matches.

The filtered conserved elements were chained by placing edges between concordant elements within 10 kb distance in both genomes, as described below. We iteratively looped over pairs of elements, in increasing order of distances between them. For this purpose, the larger of the distances calculated in both genomes was taken. We chained the elements only if each of them was either unchained or at one of the ends of its respective chain, and only if the resulting chaining order would be in line with the strandedness of these elements. We kept only the chains containing at least two conserved elements.

For mapping the loop anchors across species, we extended the anchors by 1 kb in both directions to account for possible uncertainty in calling them. We then overlapped them with both the chained conserved elements and the edges between these elements. The coordinates in the other genome of these conserved elements and edges were reduced by joining them within each chain to define the homologous loci for the loop anchors. For a pair of anchors defining a loop, all possible combinations of homologous loci for both anchors were considered as candidate loops. We called a loop “conserved” if at least one such combination matched (overlapped) a loop defined in the other species.

To assess the contribution of coding sequences to loop anchor homology (Figure S3C), we calculated gene exon coverage as follows. For each chain of conserved elements, we overlapped the conserved elements (i.e. the aligned sequences) with all annotated gene exons, and divided the total length of overlap by the total length of the conserved elements. This ratio was calculated separately in both species.

For the permutations of *D. melanogaster* loop anchors performed in Figure S3H, we randomly paired $2 \times 68 = 136$ loop anchors rather than 79 unique anchors, to make the random pairing more realistic as some loop anchors are used multiple times. The random pairing was done within each chromosome arm separately.

To compare the identity of genes at meta-loop anchors, we used ortholog annotations from OrthoDB v10.1 (<https://www.orthodb.org/>),⁸⁷ taking only protein-coding genes and their orthologs within the clade Metazoa. For each *D. melanogaster* meta-loop anchor, only the gene with the closest TSS to the anchor was considered for the ortholog analysis. Further, when analyzing the *D. virilis* orthologs of these genes, we searched for all possible orthologs and considered the closest one (in terms of distance to TSS) to any of the homologous loci of the anchor. We note that this procedure, when applied to *D. melanogaster* anchor A22 with the same anchor-to-TSS distance for its two closest protein-coding genes (*Lar* and *CG46244*), led to the choice of the same ortholog in *D. virilis* (*GJ13567*). The choice of the ortholog also determined the homologous locus of the anchor.

Reuse of published datasets

FlyAtlas RNA-seq v2 data were downloaded from http://ftp.flybase.org/releases/FB2022_04/precomputed_files/genes/gene_rpk_matrix_fb_2022_04.tsv.gz, and expression in adults (males for all tissues except ovary from females) were plotted in Figure 1H.

For visualizing DNase hypersensitive sites (DHSs) mapped by DNase-seq in WT *D. melanogaster* embryos,⁴⁰ this published dataset was lifted over from dm3 to dm6 coordinates using the LiftOver tool (<http://genome.ucsc.edu/cgi-bin/hgLiftOver>).⁶⁹

To quantify the overlap between meta-loop anchors described in this study with those of loops reported in Kc167 cells by Eagen et al.⁴³ or in nuclear cycle 14 embryos by Batut et al.²⁵ and Levo et al.,²⁶ we extended the [start; stop] coordinates of each set of anchors by ± 200 bp and quantified the number of overlaps between independent studies by ≥ 1 bp in Figure S2F. Prior to this, loop anchors published by Eagen et al. were first lifted over from dm3 to dm6 coordinates using the LiftOver tool, and separate anchors published by Eagen et al. that overlapped by ≥ 1 bp were merged to avoid overestimating loop anchor overlaps, using the “merge” command from bedtools.⁷⁰ Loop sizes plotted in Figure 1D show distances between the summits of DNase-seq peaks under meta-loop anchors (from this study) or distances between the centers of published loop anchor coordinates.^{25,26,43}

For visualizing snATAC-seq data in WT adult brains, this published dataset⁴⁶ was downloaded from GEO GSE163697 (<https://www.ncbi.nlm.nih.gov/geo/query/acc.cgi?acc=GSE163697>, supplementary file GSE163697_cisTopicObject_Adult.Rds.gz). For visualizing bulk ATAC-seq data in WT adult brains, the fastq file of sample GSM5503528 from GEO GSE181494 (<https://www.ncbi.nlm.nih.gov/geo/query/acc.cgi?acc=GSE181494>)⁴⁶ was downloaded from the SRA repository (<https://sra-pub-run-odp.s3.amazonaws.com/sra/SRR15347354/SRR15347354>) and mapped the dm6 genome assembly with the BWA-MEM aligner.

For visualizing DNase-seq data in *D. virilis* embryos, this published dataset⁴⁷ was downloaded from ArrayExpress (<https://www.ebi.ac.uk/arrayexpress/>) accessions E-MTAB-3797 and E-MTAB-9480, and remapped using the BWA tool⁶⁸ as previously described.⁴⁷ Sizes of *D. vir.* loops involving meta-loop anchors shown in Figure 2 represent distances between the midpoints of the DNase-seq peaks in 25–28 hour old *D. vir.* embryos that were assigned to meta-loop anchors. The same *D. vir.* genome assembly was used throughout this study (GSE120751 downloaded from <https://ftp.ncbi.nlm.nih.gov/geo/series/GSE120nnn/GSE120751/suppl/GSE120751%5FDvir%5FHiC%2Efa%2Egz>).⁸⁰

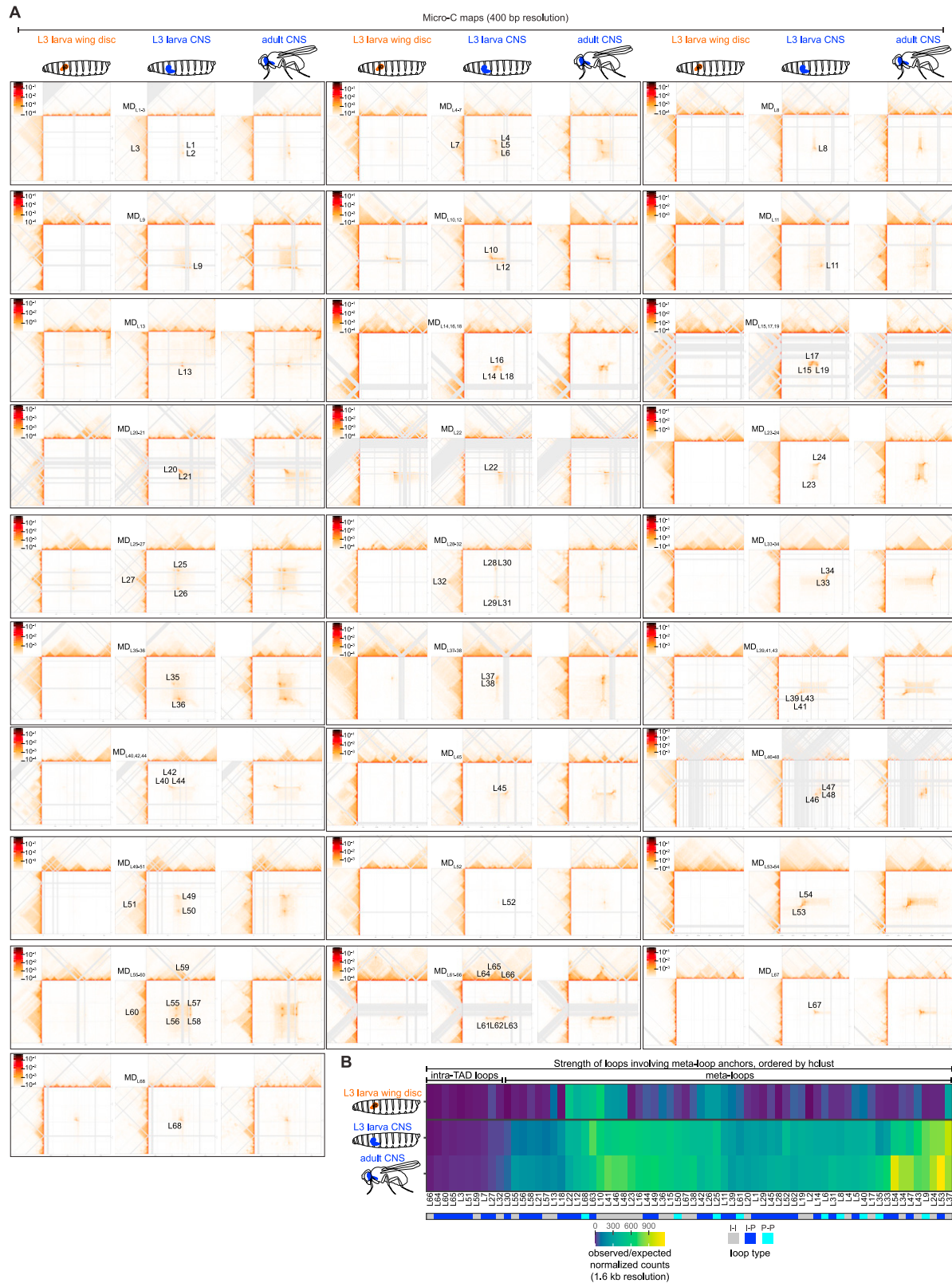
For visualizing Hi-C and CTCF and Cp190 ChIP-seq data in larval CNSs,⁴¹ these published datasets were downloaded from GEO (<https://www.ncbi.nlm.nih.gov/geo/query/acc.cgi?acc=GSE146752>).

QUANTIFICATION AND STATISTICAL ANALYSIS

All statistical analyses and software used were indicated in the respective [method details](#) section and figure legends. P values are indicated in the respective figures. All described replicate experiments are biological replicates. Samples were grouped according to genotype (wildtype or various mutants). The investigators were not blinded during data collection as the biological groups (genotypes) were well defined and handled in parallel. Computational analysis was performed by data scientists different from the researchers who collected the data. No data were excluded from the analyses.

For RNA-FISH experiments, approximately 20 embryos were examined per genotype over two independent experiments and only representative expression patterns observed in all animals are shown. These numbers were chosen because they revealed that phenotypes were reproducibly detected in all animals and because sample collection beyond this scale was rate-limiting. For Micro-C and Hi-C experiments, 10 adult or 30 third instar larval brains were dissected per replicate because these numbers allowed sufficient material to be amplified for next-generation sequencing library preparation with a limited number of PCR cycles to avoid over-amplification. This number was sufficient because all biological replicates were well correlated.

Supplemental figures

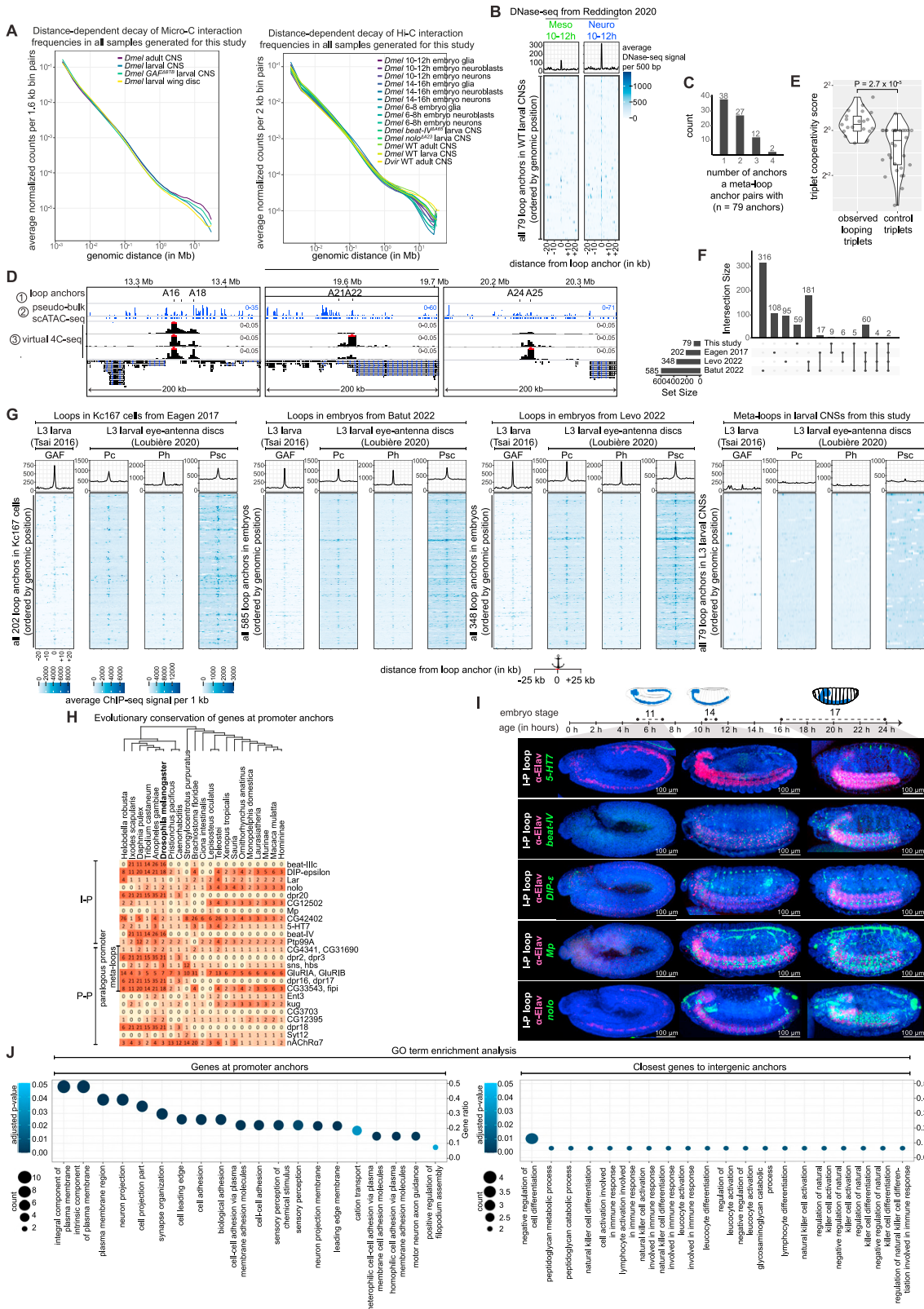


(legend on next page)

Figure S1. Comparison of meta-domains in larval wing discs and in larval and adult CNSs, related to Figure 1

(A) Micro-C maps (400 bp resolution) generated in the indicated tissues (columns) are shown separately for each meta-domain. Loops involving meta-loop anchors are marked in larval CNSs (in which they were defined). The color scales show normalized Micro-C counts.

(B) For each loop involving meta-loop anchors observed in WT larval CNSs (columns), loop strength (color, measured as the observed-over-expected normalized Micro-C count) is shown in each sample (rows). Intra-TAD loops and meta-loops (that loop between TADs) are indicated. Loop types are color-coded below.



(legend on next page)

Figure S2. Meta-loops involve genes expressed in the CNS, related to Figure 1

(A) Average normalized Micro-C (left) and Hi-C (right) counts per pairs of 1.6 kb (for Micro-C) or 2 kb (for Hi-C) bins (in y) as a function of genomic distance (using exponentially increasing bins in x) per genotype (merged biological replicates are shown for separately colored genotypes).

(B) Distribution of DNase-seq signal (blue, average per 500 bp) in FACS-purified mesodermal cells (Meso) or neurons (Neuro) from 10- to 12-h-old embryos from Reddington et al.⁴⁰ (columns) in 500-bp bins \pm 25 kb around all 79 meta-loop anchors defined in larval CNSs (rows, ordered by genomic position). Meta-loop anchors were originally defined by Hi-C and subsequently intersected with underlying DNase-seq peaks in FACS-purified neurons from 10- to 12-h-old embryos; hence the distance from the loop anchor is the distance from the summit of the DNase-seq peak associated with that anchor measured in the 5'-to-3' direction. For each column, the upper plot summarizes the average signal over all loop anchors. This shows that neurons of 10- to 12-h-old embryos have DNase-seq peaks enriched at loop anchors, and only some of these peaks are also present in mesoderm.

(C) The number of anchors (in x) that each meta-loop anchor pairs with is shown (in y).

(D) Pseudo-bulk scATAC-seq data with called peaks (this study) and virtual 4C-seq tracks derived from Hi-C data (at 2 kb resolution, from Kaushal et al.⁴¹) in WT larval CNSs. The 4C-seq tracks correspond to reads involving meta-loop anchor A16 (row 1), both A16 and A22 (row 2) and both A16 and A25 (row 3). Viewpoints are marked by red triangles. Regions with numbers of reads exceeding the y axis scale are marked by a red line. 955/39,716 (2.4%) of all Hi-C reads involving A22 also involve A25, whereas 25/480 (5.2%) of reads involving A16 and A22 also involve A25. This corresponds to the triplet cooperativity factor of 2.2, and shows that A16, A22, and A25 meta-loop anchors can engage in concurrent three-way interactions.

(E) Comparison of the distributions of triplet cooperativity factor values (points, defined in the [STAR Methods](#)) for 21 looping triplets consisting of three meta-loop anchors forming three observed loops, and for 42 control triplets. The control triplets consist of two anchors from a looping triplet and a third non-looping anchor at a comparable genomic distance as the third looping anchor, but in the opposite genomic direction. The indicated p value is from a Wilcoxon test.

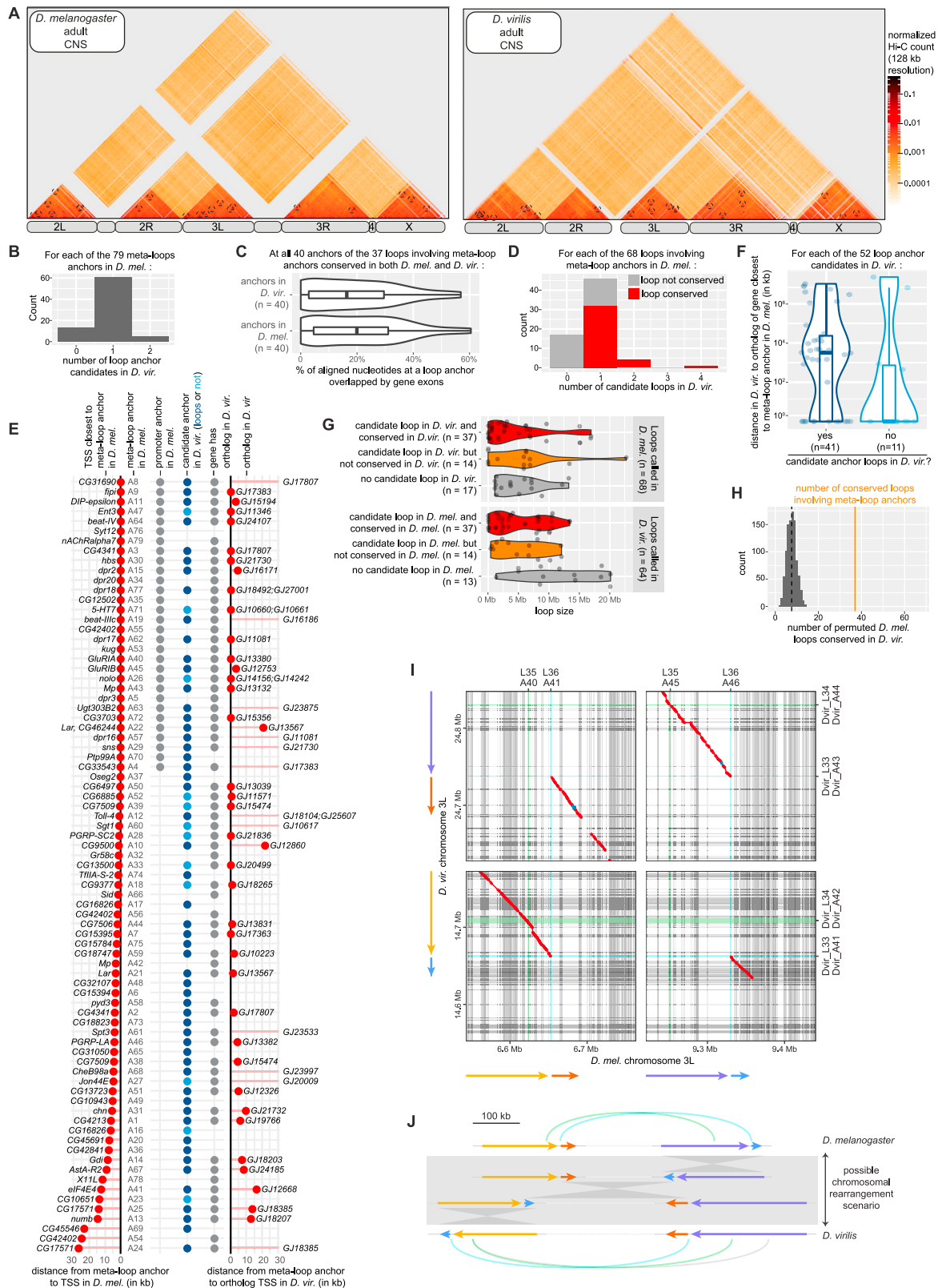
(F) Upset plot showing the overlap between anchors of meta-loops reported in larval CNSs in this study and loops defined by Hi-C in Kc167 cells⁴³ or by Micro-C in early embryos^{25,26} (rows). This shows that most meta-loop anchors found in the CNS are unique, i.e., are not used in embryos or Kc167 cells.

(G) Distribution of GAF (data from Tsai et al.⁵³) and subunits of Polycomb repressive 1 comprising Polycomb (Pc), Polyhomeotic (Ph), and Posterior sex combs (Psc) (data from Loubière et al.⁸⁹) ChIP-seq signal (blue, average per 1 kb) in 1-kb bins \pm 25 kb around loop anchors (rows, ordered by genomic location) defined in the indicated studies (columns). For each column, the upper plot shows the average signal over all loop anchors as a function of distance from the loop anchors, per 1 kb. GAF ChIP-seq was performed on larval tissues comprising CNSs,⁵³ while Polycomb ChIP-seq was performed on larval eye-antenna discs composed in large part of neurons.⁸⁹

(H) Average number of PANTHER orthologs for each gene, or pair of paralogous genes, present at promoter anchors (rows) found in the indicated species or species group (columns). Vertical lines indicate whether genes at promoter anchors only loop to an intergenic anchor (in I-P meta-loops) or also loop to another promoter anchor (in P-P meta-loops). If a gene at a promoter anchor engages in both I-P and P-P meta-loops, it was annotated as a P-P meta-loop in this figure. Another vertical line further indicates whether a P-P meta-loop involved two paralogous gene promoter anchors ("paralogous promoter meta-loops") or not.

(I) Lateral views of embryos of the indicated stages (columns) stained by immuno-RNA-FISH with a probe antisense to the indicated genes at meta-loop promoter anchors (rows, in green), α -Elav (pink, to label neurons), and DAPI (anterior, left; posterior, right; merged images on the right). This shows that all tested genes at meta-loop promoter anchors start to be expressed in the nervous system at stage 14 as neurons differentiate.

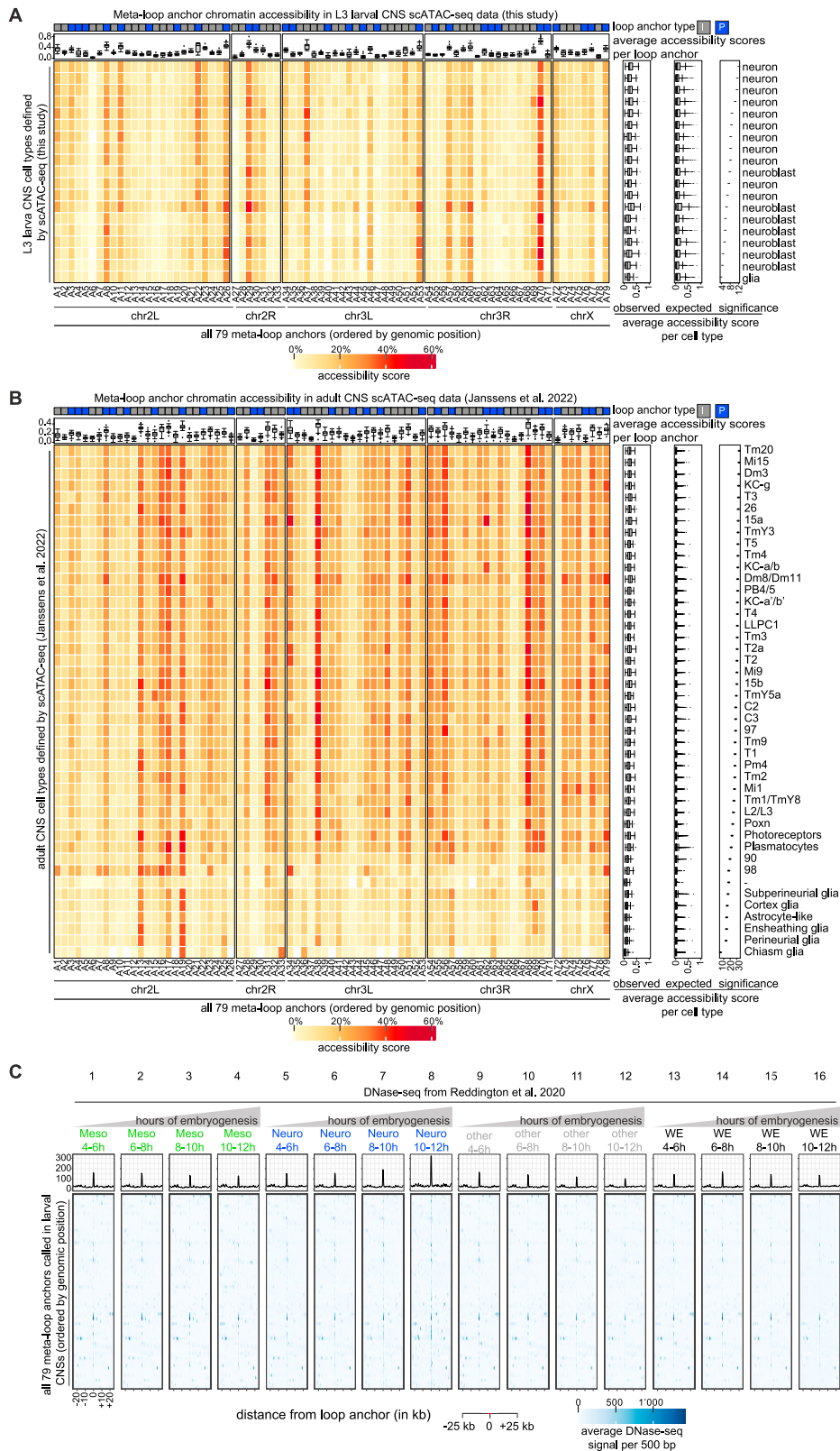
(J) GO term enrichment analysis of genes at promoter anchors (left) and of genes whose TSSs are closest to intergenic anchors. GO terms (in x) are ranked by gene enrichment ratios (in y). Dot sizes indicate the number of genes associated with a given GO term and are colored according to false discovery rate-adjusted p value.



(legend on next page)

Figure S3. Meta-loop conservation over evolution, related to Figure 2

- (A) Whole-genome views of Hi-C maps of *D. mel.* (left) and *D. vir.* (right) adult CNSs. Dotted circles mark meta-domains.
- (B) For each *D. mel.* meta-loop anchor, the number of homologous loci in *D. vir.* ("candidate *D. mel.* meta-loop anchors in *D. vir.*") is counted.
- (C) Violin plots showing exon coverage at all 40 anchors of the conserved 37 loops involving meta-loop anchors. For each anchor, we considered all the aligned nucleotides of the respective alignment chain and calculated the fraction of these nucleotides overlapped by gene exons. The overlaid boxplot shows the median (thick vertical line) and the 25th and 75th percentiles (hinges).
- (D) For each of the 68 loops involving meta-loop anchors in *D. mel.*, the number of pairs of loci found in *D. vir.* that are homologous to the respective pair of *D. mel.* meta-loop anchors ("candidate loops in *D. vir.*") is shown in x. Candidate loops in *D. vir.* for a given *D. mel.* meta-loop are colored in gray when none of these were observed to loop by Hi-C in *D. vir.* (labeled "not conserved"), or in red when at least one of these candidates were observed to loop in *D. vir.* (labeled "conserved"). Note that a few *D. mel.* meta-loops had up to 2 or 4 candidate matches in *D. vir.* due to anchor duplication in *D. vir.* Nevertheless, each *D. mel.* meta-loop had at most one loop conserved in *D. vir.* (i.e., the remaining 1 or 3 candidate meta-loops in *D. vir.* did not loop).
- (E) All 79 meta-loop anchors in *D. mel.* (rows) are sorted by their distance to the closest indicated gene TSS (left). For each anchor, dots indicate whether (dot present) or not (dot absent) the anchor is a promoter anchor, has a candidate match in *D. vir.*, and has an ortholog in *D. vir.* of the gene that it is closest to (middle). Colors indicate whether the candidate anchor in *D. vir.* loops (dark blue) or not (light blue) according to *D. vir.* CNS Hi-C maps. For anchors with both a candidate match and an ortholog in *D. vir.* present on the same chromosome, the closest distance between the match and the putative TSS of the ortholog is shown (right).
- (F) Out of 79 *D. mel.* meta-loop anchors, 52 have both a candidate anchor in *D. vir.* and a *D. vir.* ortholog of the gene closest to the meta-loop anchor in *D. mel.* For each of these 52 loop anchor candidates in *D. vir.*, the distance to the ortholog is plotted (in y, in kb). Anchor candidates are categorized as those that loop in *D. vir.* (left) and those that do not (right). This plot shows that loop anchor candidates that loop in *D. vir.* are not any closer to the ortholog genes than loop anchor candidates that do not loop ($p = 0.09$, Wilcoxon test).
- (G) (Top) For each of all 68 loops involving meta-loop anchors in *D. mel.*, those with candidate loops in *D. vir.* that are conserved (i.e., loop, red) or not (i.e., do not loop, orange) in *D. vir.*, and those that did not have a candidate match in *D. vir.* (gray) are shown as dots arranged according to their sizes (in x). (Bottom) For each of all 64 loops involving meta-loop anchors called in *D. vir.*, those with candidate loops in *D. mel.* that are conserved (red) or not (orange) in *D. mel.*, and those that did not have a candidate match in *D. mel.* (gray) are shown as dots arranged according to their sizes (in x).
- (H) Matching of randomly permuted loops in *D. mel.* to observed loops in *D. vir.* The distribution (gray) is derived from 1,000 random pairings of *D. mel.* loop anchors. The average number of matches of randomly permuted loops (dashed vertical line) is 4.86 times lower than the observed number of loops conserved in *D. vir.* (vertical orange line).
- (I) Illustration of the complex loop referenced in Figure 2C that had rearrangement junctions at both anchors. Alignment chains of conserved sequence fragments in concordant (blue) and discordant (red) orientation. The four colored arrows on the sides mark the roughly conserved regions. Green and cyan stripes indicate anchors of loops conserved in *D. mel.* and *D. vir.*; gray stripes indicate exons.
- (J) The gray box indicates a possible chromosomal rearrangement scenario that may have occurred during evolution to result in the observed meta-loop anchors in *D. mel.* (top, white background) and *D. vir.* (bottom, white background).



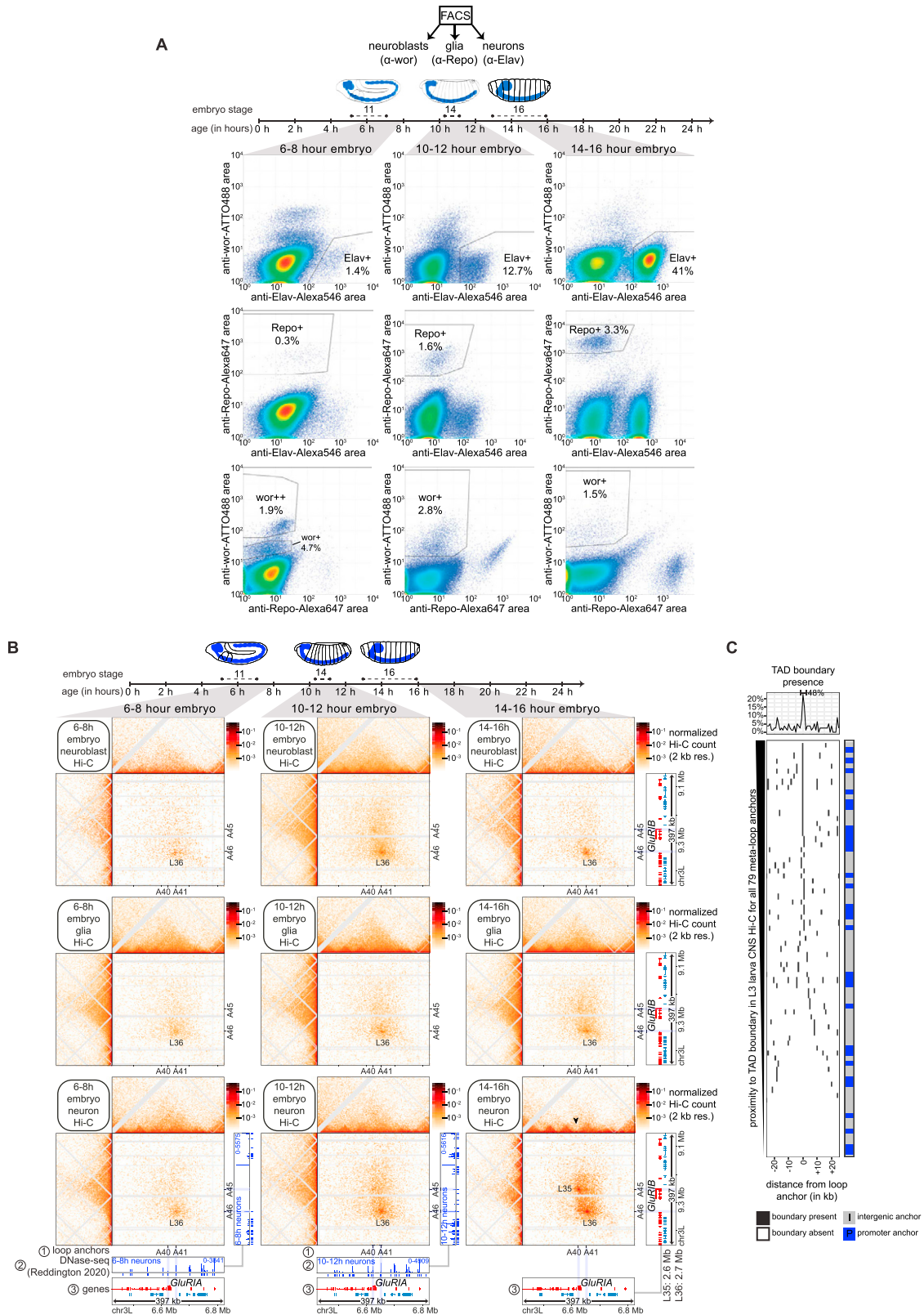
(legend on next page)

Figure S4. Chromatin accessibility at meta-loop anchors, related to Figure 3

(A) Meta-loop anchor chromatin accessibility in L3 larval CNSs determined by scATAC-seq in this study. An “accessibility score” was defined as the percentage (color) of single cells in which chromatin was accessible in a 20 bp region around each meta-loop anchor. Accessibility scores are shown for each meta-loop anchor (columns, ordered by genomic position) in each cell type (rows) defined as neuron, neuroblast or glia (as described in the [STAR Methods](#)). Meta-loop anchors were classified as intergenic (I) or promoter (P) (top row). For each cell type (rows), the side boxplots summarize the average accessibility scores plotted at every loop anchor (each data point is a loop anchor). The significance of the observed relative to the expected result is also shown. For each meta-loop anchor (columns), the top boxplots summarize the average accessibility score in every cell type (each data point is a cell type).

(B) Same as (A) but showing meta-loop anchor chromatin accessibility in adult fly CNSs determined by scATAC-seq by Janssens et al.⁴⁶ Cell types (rows) were defined by that study.

(C) Distribution of DNase-seq signal (blue, average per 500 bp) from FACS-purified mesodermal cells (Meso), neurons (Neuro), non-mesodermal and non-neuronal cells (other) from embryos or whole embryos (WE) of the indicated hours of development (columns, data from Reddington et al.⁴⁰) in 500-bp bins \pm 25 kb around all 79 meta-loop anchors defined in larval CNSs (in rows, ordered by genomic position). Meta-loop anchors were originally defined by Hi-C and subsequently intersected with underlying DNase-seq peaks in FACS-purified neurons from 10- to 12-h-old embryos (shown in column 8); hence the distance from the loop anchor is the distance from the summit of the DNase-seq peak associated with that anchor measured in the 5'-to-3' direction (as described in the [STAR Methods](#)). For each column, the upper plot summarizes the average signal over all loop anchors. This shows that neurons of 10- to 12-h-old embryos have DNase-seq peaks enriched at meta-loop anchors, and only some of these peaks are present in younger neurons or in other embryo samples.



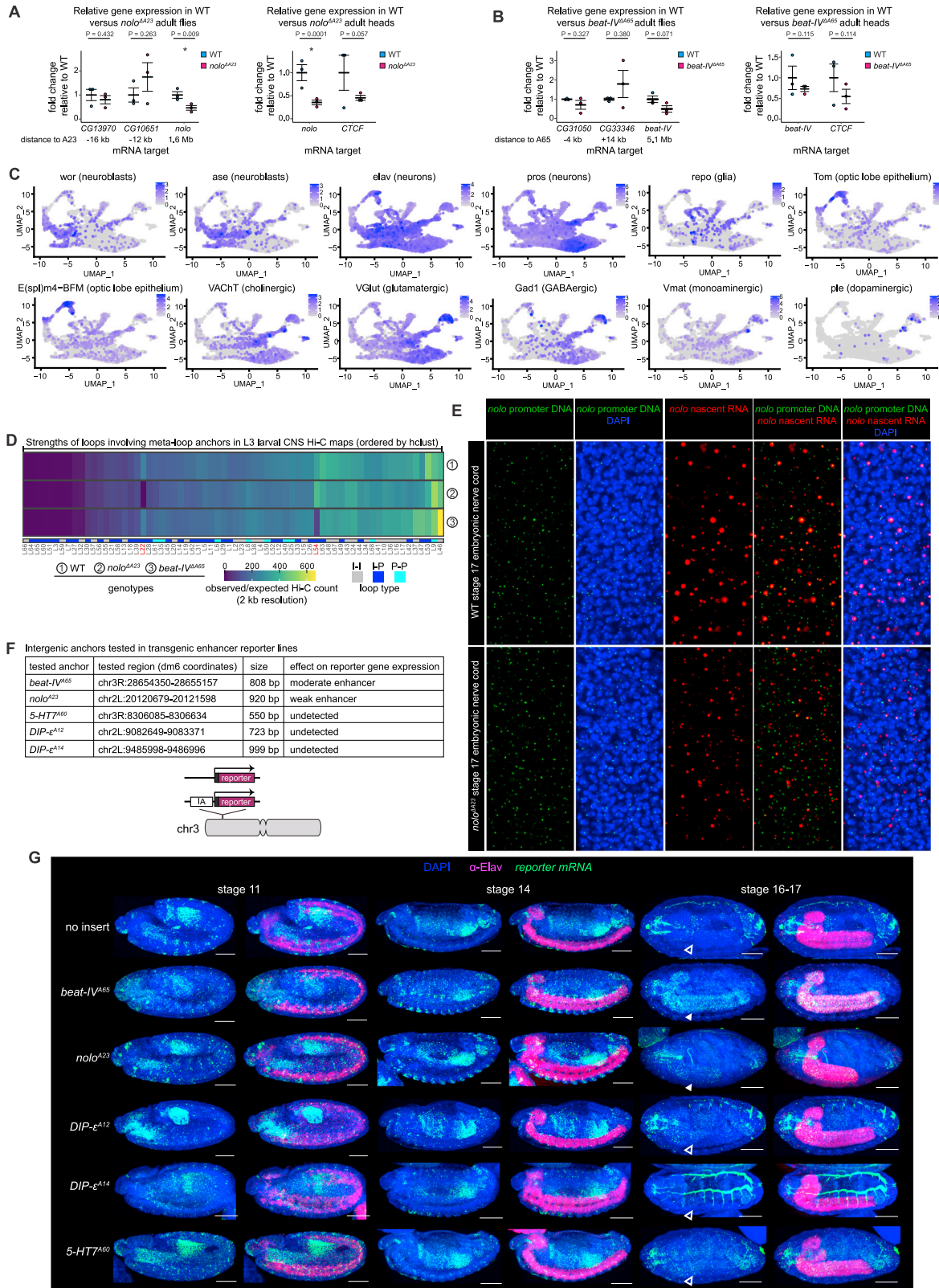
(legend on next page)

Figure S5. Developmental time-course of meta-loop formation in CNS cell types, related to Figure 3

(A) (Top) Embryos at 6–8, 10–12, or 14–16 h of development were fixed and dissociated into nuclei, then co-stained with directly labeled antibodies against lineage markers of neurons (α -Elav), glia (α -Repo), or neuroblasts (α -Wor). (Bottom) Each cell type was FACS-purified with the indicated gates. The proportion of neurons and glia progressively increased in older embryos, whereas the inverse was true for neuroblasts.

(B) Hi-C maps, DNase-seq tracks in neurons purified from 6–8 or 10–12 h embryos from Reddington et al.,⁴⁰ and gene tracks of the left (in x) and right (in y) anchors of the *GlurIA-GlurIB* meta-domain harboring meta-loops L35 and L36 in neuroblasts (row 1), glia (row 2) or neurons (row 3) FACS-purified from 6- to 8-h-old (column 1), 10- to 12-h-old (column 2), or 14- to 16-h-old (column 3) embryos. The meta-domain is shown in grid view in the center. This shows that L36 is detectable in all samples, whereas L35 connecting the promoters of *GlurIA* and *GlurIB* is only clearly distinguishable in neurons from 14- to 16-h old embryos. The chromatin of L36 anchors is consistently accessible earlier in neuronal differentiation than that of L35 anchors. The arrowhead marks an example of a TAD boundary that appears close to meta-loop L35 anchor A40 concomitantly with looping.

(C) Distribution of the presence of TAD boundaries called in WT larval CNS Hi-C maps by Kaushal⁴¹ in 1-kb bins \pm 25 kb around all 79 meta-loop anchors. The summarized percentage of loci with a TAD boundary present over all loop anchors is shown on top. Anchors are classified as intergenic or promoter on the right. This shows that 48% of meta-loop anchors are within \pm 2 kb (i.e., within \pm 1 binsize at which TAD boundaries were called) of a TAD boundary.



(legend on next page)

Figure S6. Effect of meta-loop anchors on gene expression, related to Figure 5

(A) Fold change (in y) of mRNA levels of indicated genes (in x) in WT versus $nolo^{\Delta A23}$ whole-bodied adults (left) or adult heads (right) quantified by RT-qPCR. Dots represent individual biological triplicate values, thick horizontal bars represent average values, and error bars indicate standard deviation. p values from two-sided unpaired heteroscedastic t tests are shown. Gene distance to the deleted A23 intergenic meta-loop anchor is indicated below. *CTCF* is not expected to be affected by $nolo^{\Delta A23}$ and serves as negative control. This shows that $nolo$ mRNA levels are reduced by 2- (in whole bodies) to 3-fold (in heads) in $nolo^{\Delta A23}$ mutants relative to WT.

(B) Same as (A) but quantifying the expression of *beat-IV* and genes around the deleted A65 intergenic meta-loop anchor in WT versus *beat-IV* $^{\Delta A65}$ mutants. This shows that *beat-IV* mRNA levels are not significantly changed in *beat-IV* $^{\Delta A65}$ mutants relative to WT.

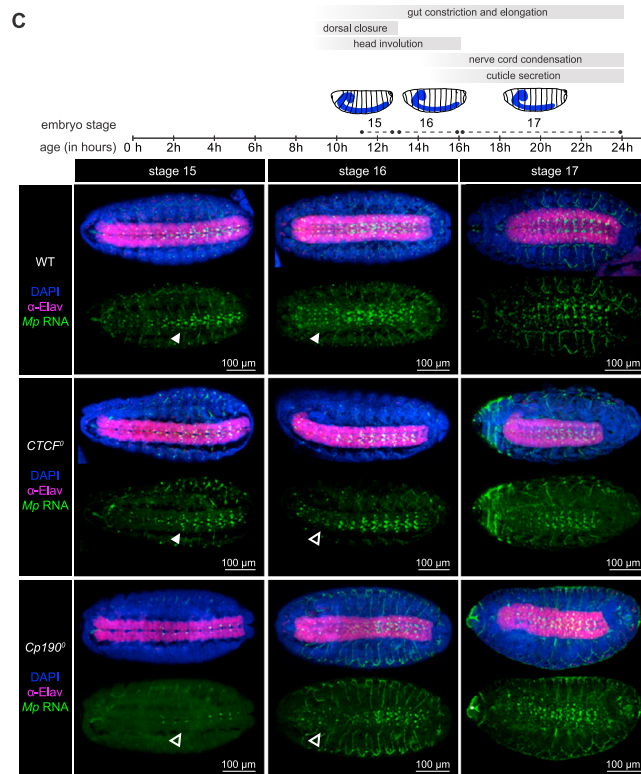
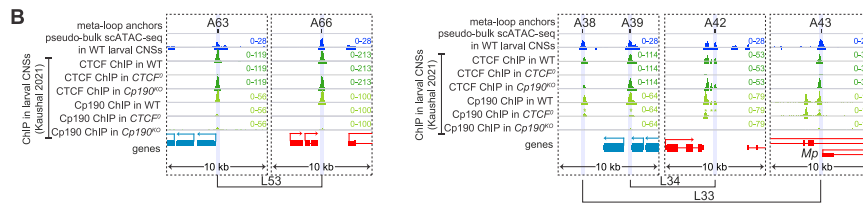
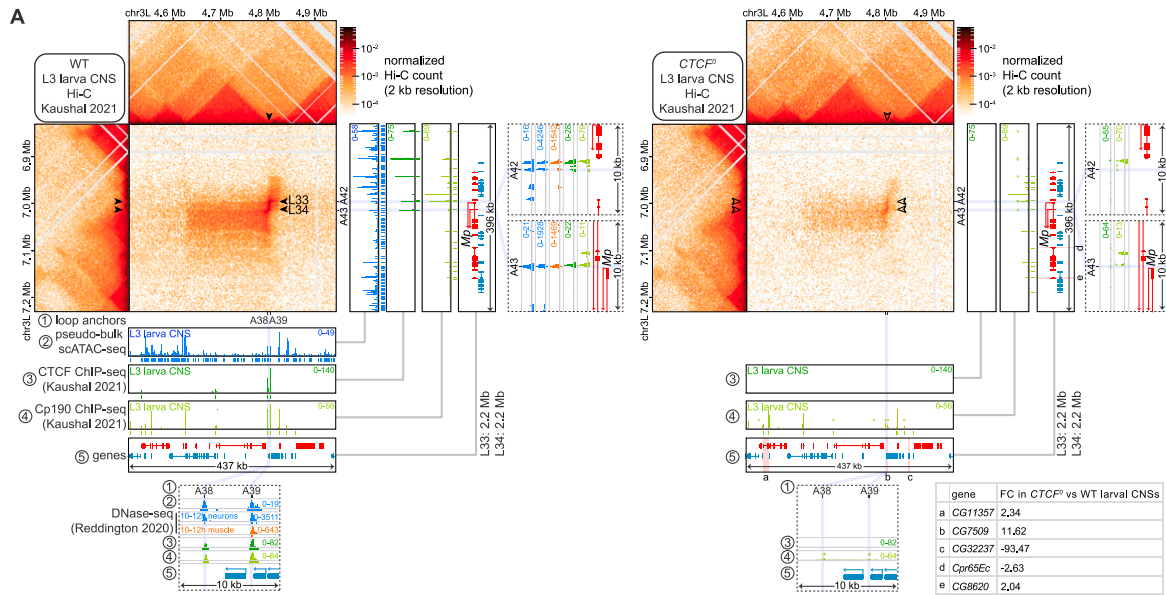
(C) Marker gene expression used to annotate broad cell types in the combined WT, *beat-IV* $^{\Delta A65}$, and $nolo^{\Delta A23}$ larval CNS scRNA-seq data presented in Figure 5A.

(D) For each meta-loop called in WT larval CNSs (columns, ordered by hierarchical clustering), loop strength (color, measured as the observed-over-expected normalized Hi-C count) is shown in larval CNSs of each indicated genotype (rows).

(E) Nascent RNA-DNA-FISH images of nerve cords of stage 17 WT (row 1) and $nolo^{\Delta A23}$ mutant (row 2) embryos with probes against *nolo* intronic RNA (red) and *nolo* promoter DNA (green). *nolo* nascent RNA-FISH signal was weaker in $nolo^{\Delta A23}$ mutants compared to WT. We therefore imaged RNA-FISH signal in the mutant with higher laser intensity than in WT to detect nuclei with even low RNA-FISH signal. Because of the resulting higher background signal, less *nolo* nascent RNA-FISH spots co-localized with *nolo* promoter DNA-FISH spots in $nolo^{\Delta A23}$ mutants than in WT. To distinguish real *nolo* nascent RNA-FISH signal from background in $nolo^{\Delta A23}$ mutants, *nolo* promoter DNA-FISH spots with or without overlapping *nolo* nascent RNA-FISH signal were counted in biological triplicates and plotted in Figure 5E.

(F) List of intergenic anchors (IAs, 550–999 bp) tested for their ability to drive reporter gene transcription when cloned upstream of the minimal *Drosophila* synthetic core promoter (DSCP) transcribing a reporter gene, as schematized below. A transgene without an intergenic anchor was included as negative control to reveal the activities of local enhancers around the transgene integration site. Each transgene was stably integrated into the VK33 genomic landing site on chromosome 3L of WT embryos. For each tested anchor, its name and genomic coordinates and the observed effect it had on reporter gene expression relative to the negative control is reported.

(G) Lateral views of embryos homozygous for the indicated transgenes (rows, described in F) at the indicated developmental stages (columns) stained by immuno-RNA-FISH with a probe antisense to reporter gene mRNA (green), α -Elav (pink), and DAPI (anterior, left; posterior, right; merged images on the right). The negative control (row 1) shows that local enhancers around the VK33 transgene integration site drive reporter gene expression in dynamic spatio-temporal patterns, but not in the embryonic nervous system (labeled by α -Elav) at any stage. Of five intergenic anchors tested, only those of the *nolo* or *beat-IV* I-P meta-loops weakly or moderately drove reporter gene expression in the nervous system of late-stage embryos, respectively. Empty/filled arrowheads mark absence/presence of reporter gene mRNA in stage 16–17 embryonic nerve cords in each genotype. The shown reporter gene expression patterns were observed in 100% of embryos (≥ 5 embryos imaged per genotype and stage).



(legend on next page)

Figure S7. CTCF loss destabilizes the *Mp* meta-domain, related to Figure 7

(A) Hi-C map of meta-loops L33 and L34 in WT (left) and *CTCF*⁰ mutant (right) larval CNSs. L34 connects the downstream promoter of *Mp* to an intergenic anchor located 2.2 Mb away. Filled/empty arrowheads point to WT/reduced meta-loop strength in *CTCF*⁰ mutants (in the meta-domain), or to WT/weakened TAD boundaries in *CTCF*⁰ mutants (in x and y). Pseudo-bulk scATAC-seq and ChIP-seq profiles of CTCF and Cp190 in larval CNSs are also shown. Colored bars under ChIP-seq tracks mark called ChIP peaks, and asterisks mark differentially Cp190-bound regions in *CTCF*⁰ mutants compared to WT. Genes determined to be differentially expressed by RNA-seq in *CTCF*⁰ mutant relative to WT larval CNSs ($\text{padj} < 0.05$ and $|\text{fold change}| > 1.5$) are highlighted in pink and labeled with a letter on the gene track on the right, and the fold changes are indicated in the table below. Hi-C, ChIP-seq, and RNA-seq data were published by Kaushal et al.⁴¹ Dotted rectangles show zoomed-in views of 10 kb regions around meta-loop anchors. Note that the scale for ChIP-seq tracks is kept constant between WT (left) and *CTCF*⁰ mutants (right).

(B) The indicated pseudo-bulk scATAC-seq or ChIP-seq profiles generated in larval CNSs of the indicated genotypes are shown for anchors A63 and A66 of meta-loop L53 (shown in Figure 7A), A38 and A43 of meta-loop L33 (shown in A), and A39 and A42 of meta-loop L34 (shown in A). Note that CTCF binding is largely unaffected at these meta-loop anchors in *Cp190*^{KO} mutant larval CNSs.

(C) Ventral views of embryos of indicated genotypes (rows) and stages (columns) stained by immuno-RNA-FISH with a probe antisense to *Mp* mRNA (green), α -Elav (pink) and DAPI (anterior, left; posterior, right; merged images on top). Embryos were staged according to developmental landmarks indicated above (as in Figure 7E). Specific RNA-FISH signal appears as dots; string-like and broad green non-specific signal is visible in trachea and epidermis. Filled/empty arrowheads point to WT/reduced *Mp* RNA-FISH signal in each genotype. The phenotypes shown here were observed in 100% of embryos (≥ 6 embryos imaged per genotype and stage).